Università degli Studi di Genova

Scuola di Scienze Matematiche, Fisiche e Naturali
Corso di Laurea Magistrale in Fisica

Thesis for the Master's Degree in Physics

Efficiency and stability of a collisional quantum battery in the presence of anharmonicity

Supervisors:
Prof. **Dario Ferraro**
Prof. **Fabio Cavaliere**
Co-supervisor:
Prof. **Paolo Solinas**

Candidate:
Nicolò Massa

Academic Year 2023–2024

Contents

Introduction

Quantum technologies have witnessed outbreaking progresses in the last decades, both from the theoretical and experimental point of view, which led to the development of a very active cross-disciplinary field of research. This field can be divided into four main domains [1]: quantum computation [2, 3], which aims at exploiting quantum effects to speed up algorithms such as number factorization and search in a database; quantum simulation, which emulates less-accessible quantum systems through more accessible and controllable ones [4]; quantum communication, aimed at increasing the security and efficiency of data transmission processes [5, 6]; and quantum sensing, where the sensitivity of coherent quantum systems with respect to external perturbations is used in order to increase the accuracy of physical measurements also for metrological applications [7]. Within this broad panorama, quantum batteries have gained more and more relevance during the last decade.

Generally speaking, a battery is a device created in order to store and release energy on demand. The ordinary batteries which allow the functioning of everyday life devices are the so called electro-chemical batteries, which typically store chemical energy and release it in the form of electric energy [8]. Quantum batteries can be seen as the quantum counter parts of such devices: they consist in quantum multi-level systems whose energy is increased by populating their excited states, through a charging process which involves the coupling with one or many other quantum systems, playing the role of chargers.
The concept of a quantum battery was firstly introduced in 2013 by R. Alicki and M. Fannes [9]. Inspired by the development of the field of quantum thermodynamics of mesoscopic and nanoscopic systems [10], they showed that entanglement and quantum collective effects can lead to advantages in terms of work extraction. Starting from this seminal idea, many other works dealt with the extension of thermodynamics rules to arbitrary quantum systems and with the possibility of exploiting quantum effects in order to improve their performances as energy storage devices [11, 12, 13].

Since then, various different models of quantum batteries have been proposed, based on quantum harmonic oscillators [14, 15], three-levels systems [16, 17] but, mainly, two-level systems [14, 18, 19]. The reason for the prevalence of two-level systems is that they are the fundamental unit of quantum computation, and they have been realized in various platforms such as trapped ions [20], semiconductor quantum dots [21] and superconducting circuits [22]. Chargers employed within the above works can be both external classical fields [17, 23, 24] or quantum systems, such as photons trapped in a cavity [14, 25, 26] or other two-level systems [14].
Although a great part of theoretical works considered superconducting qubits, the first

experimental realization of a quantum battery, reported in [27], employed fluorescent molecules. Here, molecules effectively behaved as two-level systems and were inserted into a cavity acting as a charger. This was the first experimental work addressing the power produced by quantum batteries and its results were in agreement with the theoretical predictions reported in [25].
This work has been followed by new experimental proposals based on superconducting qubits [28] and quantum dots [29], triggering further interest in the topic.

Recently, the attention has shifted to the so-called collisional quantum batteries, whose charging is realized through the sequential interaction with a collection of quantum systems individually interacting with the battery [30, 31, 32, 33]. Among these, a prominent role is played by multi-level batteries, usually quantum harmonic oscillators, that are charged through sequential interactions with a collection of two-level systems whose state is suitably engineered. The name given to these devices derives from the fact that they are based on the collisional models introduced for the study of dissipation in open quantum systems, where the environment is decomposed into a collection of elementary units that interact with the system under examination, leading for example to thermalization phenomena [10, 34]. The fundamental difference lies in the fact that, in the context of quantum batteries, these interaction processes actively contribute to the net transfer of energy from the chargers to the battery.

In this context the present master thesis aims at studying theoretically the effects of the anharmonicity on a multi-level collisional quantum battery, characterizing its efficiency and stability, exploring the possibility of extracting the stored energy and comparing coherent and incoherent charging protocols. From an experimental point of view the anharmonicity is one of the relevant features of a particular superconducting circuit, the so called transmon [22]. This makes this analysis very relevant in view of future implementations of these device.
In **Chapter 1** we introduce the most relevant physical platforms employed in the field of quantum technologies, which reveal to be the most suitable also for the realization of quantum batteries. After setting the notation providing a brief theoretical background on such systems, we introduce the concept of quantum batteries and the figures of merit relevant for our purposes. **Chapter 2** deals with the theoretical framework of open quantum systems, comparing the master equation approach with the collisional one and providing an example of the latter, which will be the starting point for **Chapter 3**. Here, in fact, we will retrace and extend the study done in [32, 33] about the possibility of employing a Micromaser as a quantum battery. This system consists in a cavity, employed as an energy storage device, which sequentially interacts with a stream of two-level systems, playing the role of chargers.
The striking feature of this model is that, on the one hand, incoherent chargers allow to store energy in the system only for precisely fine-tuned values of the the system-ancilla coupling whereas, on the other hand, coherent chargers make the stored energy stable with respect to coupling deviations from such values. In order to reproduce these results on coherent and incoherent charging protocols, we will provide both analytical and numerical arguments. Furthermore, we will show original results for regimes of previously unexplored coherences. **Chapter 4** is the core of the original part of this thesis, where we will analyze the possibility of realizing an anharmonic collisional quantum battery,

characterizing its stability and providing original numerical results about the storage and extraction of energy.
As stated above, the platform we will consider consists of a superconducting circuit in the transmon regime, playing the role of the battery, charged through the sequential interaction with a collection of identical two-level systems.
The numerical approach performed to solve such collisional dynamics highlights relevant differences between the coherent charging protocol and the incoherent one. In the first case, in fact, we will show that it is possible to store a significant amount of energy in the battery and to extract it almost entirely whereas, in the second case, these relevant features are almost completely lost. Thus, similarly to the harmonic collisional quantum batteries studied in literature, quantum coherences at the level of the ancillae lead to advantages in terms of collisional charging performances also in the case of the transmon. These advantages, however, reveal to be far more dramatic in the transmon case than in the Micromaser case. The former, in fact, needs quantum coherences at the level of the ancillae for both the storage and extraction of energy whereas the latter allows to store a significant, although instable, amount of energy also using an incoherent protocol.
Numerical simulations have been performed employing QuTiP (Quantum Toolbox in Python) [35] and its tools for matrix calculations and Master Equations solving. Technical details for the code implementation have been discussed in the Appendix.

Chapter 1

Introduction to quantum batteries

This Chapter sets the background needed to study quantum batteries. In Section 1.1 we introduce the topic of quantum batteries. Section 1.2 surveys the most important physical platforms for quantum computation and information, which are expected to be the most promising testbeds for the implementation of quantum batteries. After this, in Section 1.3 we will introduce the theoretical tools required to describe such systems setting a general notation for the rest of the thesis. At last, in Sec. 1.4 we will introduce quantum batteries, focusing on their most important figures of merit and, in Sec. 1.5, we will provide examples of simple quantum battery models.

1.1 Road towards quantum batteries

The problem of realizing efficient devices for the storage and release of energy is one of the most important challenges of our society. Most common devices for such purposes are electrochemical batteries [8], whose origin dates back to the Eighteenth and Nineteenth centuries, when their functioning principles were firstly studied and the first electrochemical cells were realized. These devices revealed to be very versatile, spreading in all technological fields. The recent increasing demand for energy storage devices able to handle great power densities has been only partially satisfied by realizing new classes of electrochemical supercapacitor electrodes [36].
For these reasons it is worth, on the one hand, improving already existing devices, for example considering innovative materials [37] and, on the other, investigating new classes of batteries based on principles which are different from electrochemical ones.
The trend towards miniaturization of devices emerged during the last decades, as well as the development of the field of quantum technologies have led to an increasing interest in the topic of energy transfer between quantum systems and the unavoidable trade-offs associated to such transfer, studied by the so called *quantum thermodynamics* [11, 38, 39]. It is well known, in fact, that the large applicability of thermodynamics and the validity of its laws are related to the fact that it does not take into account microscopic details. In principle, then, thermodynamical laws and bounds for systems at the micro and nano scales could be different from the ones we are used to at the macroscopic level, converging to them only in the macroscopic limit [11, 19, 38, 39, 40].
It is in this context that the interest on quantum batteries arose. These are devices which aim at outperforming their classical counterparts in terms of several figures of merit, by exploiting purely-quantum features such as entanglement and quantum coherences.

The first work dealing with quantum batteries [9], in fact, tried to characterize the amount of extractable work from a system used to store energy temporarily.
The importance of the study of quantum batteries, however, goes beyond the realization of devices, since they can also impact other branches of quantum technologies such as quantum information processing, in order, for example, to evaluate the energetic cost of qubit operations [41, 42].

1.2 Platforms for quantum batteries

The theoretical models and physical platforms considered in the field of quantum batteries have been previously extensively studied for both quantum computation and quantum information purposes. The aim of this Section is to provide an insight on such platforms and their experimental realization.
Since two-level systems (TLS) are at the basis of qubits, the fundamental unit of quantum computation [10, 43], and of the simplest models of quantum batteries [18], we describe here how they can be realized and what are the main environmental effects on such implementations. At last, we will briefly describe physical realizations of cavities and resonators, fundamental systems in the field of quantum computation, employed for example in the readout processes of qubits, as well as in the field of quantum batteries, where they can be used both as batteries and chargers.

1.2.1 Two-level systems platforms

A two-level system is the simplest possible quantum system, characterized by a two dimensional Hilbert space. Its quantum states are therefore given by all the possible quantum superpositions of two independent states in this space. Practical implementations of two-level systems can be divided into two main categories, whether they are based on natural or artificial systems.
On the one hand, since nature provides equal copies of them, natural systems such as neutral atoms and ions are suitable for the realization of qubits arrays. Furthermore, they can be isolated from the external environment more easily than artificial systems such as superconducting circuits or semiconducting quantum dots [20]. However, they also present disadvantages such as the fact that their parameters are not tunable, together with technical difficulties in coupling them.
On the other hand, artificial platforms have the advantage of custom-designed features, which allows tunability of parameters such as energy levels spacings. Furthermore, they are easier to put in connection, since they can be wired together in a chip [44]. Disadvantages for this kind of platforms are, for example, issues in building equal copies and in isolating them from noise sources.

At the operational level, other differences may arise, regarding for example the best working conditions in terms of temperature (nK-μK for neutral atoms, μK-mK for ions and superconducting qubits and K for quantum dots [20]).
In order to isolate two levels out of their multi-level structures, all these systems must present anharmonicity of the energy spectra. In other words, the transition frequency between the two states forming the desired qubit must be sufficiently different from the other transition frequencies. If this is not the case, performing operations on the qubit

could cause non-zero populations of other levels, and the system could not be treated as a qubit anymore [45, 46].
In the following we will briefly discuss some examples before introducing the superconducting qubits in the next subsection.

Trapped ions Since atoms and ions are characterized by an anharmonic energy levels structure they are natural candidates for the realization of qubits. Ions are of greater utility with respect to neutral atoms since, thanks to their charge, they are easier to confine through time dependent electromagnetic traps and also easier to couple in order to realize two qubits gates [20, 43].
Their long-lived internal energy levels are used to encode quantum information and can be excited through laser radiation [20].
For quantum computation purposes they must be trapped and cooled to very low temperatures in order to allow the confinement [43]. This can be realized combining constant and alternating electric fields, an example being the so called *Paul trap*, where the ion is subjected to a saddle potential with rotating confinement direction (see Fig. 1.1(a)), which effectively leads to a well of the form

$$V(x,y,x) = \frac{1}{2}m\big(\omega_x x^2 + \omega_y y^2 + \omega_z z^2\big), \tag{1.2.1}$$

shown in Fig. 1.1(b). Provided that the frequencies are tuned so that $\omega_x \approx \omega_y \gg \omega_z$

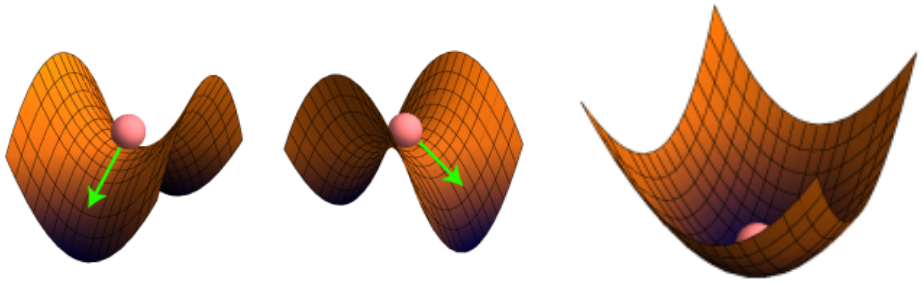

(a) (b)

Figure 1.1: Mechanical analogous of a Paul trap: (a) Rotation of a saddle potential confining a particle; (b) Effective potential experienced by the particle. Images taken from [47]

the ion motion develops approximately only along the z direction, and is characterized by vibrational modes which are typical of a harmonic oscillator [43]. Thus, the need to cool down ions derives from the fact that, in order to manipulate their internal degrees of freedom, they must be in their vibrational ground state. This condition is satisfied provided that the temperature regime is such that $k_B T \ll \hbar\omega_z$. This can be realized through cooling techniques such as laser Doppler cooling [43]. This consists in inserting the ion between two laser beams with opposite directionality and frequencies just below the resonance condition with the vibrational frequency of the ion. When the ion moves oppositely to the direction of one of these laser beams, it sees a greater frequency of the incoming photons, which now is closer to the resonance condition. This enhances the absorption of the photon which, in turn, transfers its momentum to the ion, slowing it down and cooling it. This happens independently from the direction of motion of the ion due to the presence of the two opposite beams.

Once the ion has been cooled, the qubit is obtained by isolating two levels out of the ion internal energy levels structure.
Lasing techniques are also a powerful instrument for the readout of this kind of systems [20].

Quantum dots Quantum dots can be realized as microscopic to nano-scale semiconductor structures where electrons are confined in all three dimensions [48], leading to atom-like discrete energy levels. This kind of devices can be realized through growth techniques or electrode gates over a two dimensional electron gas (2DEG). Their main advantages are the possibility of engineering them properly in order to have control on system parameters, together with their operational temperature reaching the Kelvin scale [20]. Furthermore, arrays of quantum dots can be realized both through growth techniques [48] and through multiple gating over a 2DEG [49] (see Fig. 1.2), which is a relevant fact for scalability purposes.
One of the most relevant works considering the employment of quantum dots as qubits has been proposed by D. Loss and D. P. DiVincenzo in [21]. Here, the implementation of a universal set of one- and two-qubits gates for quantum computation is discussed. The idea is to use single-electron dots as qubits, where the two levels are given by the two spin states of the electron. This choice is motivated by the fact that spin degrees of freedom of an electron in a single electron quantum dot are weakly coupled with the environment, leading to long decoherence times (see Sec. 1.2.3) [21]. Encoding the qubit in the TLS formed by the spin of the electron allow to perform single qubit operations by applying an external magnetic field [21] or by properly engineering the gate used to create the dot structure [50].

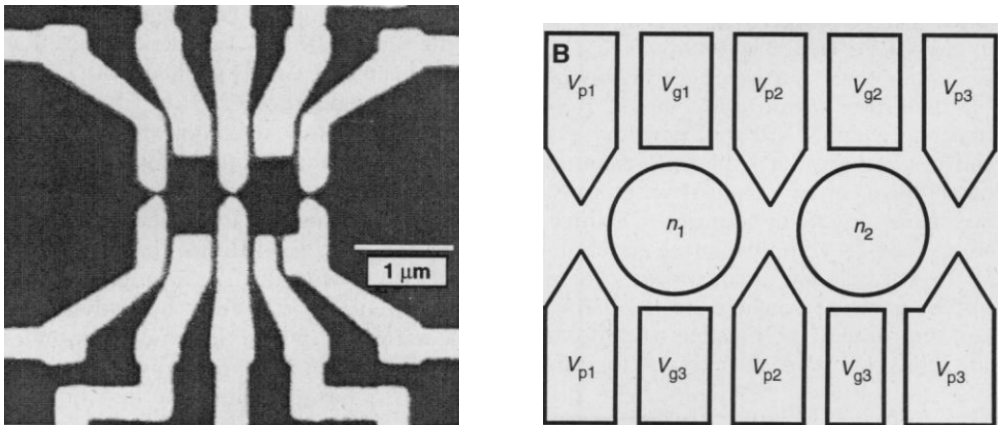

(a) (b)

Figure 1.2: (a) Scanning Electron Microscope image of a two dot structure created through the action of gate electrodes (grey components). (b) Schematic representation of the electrodes needed to control the system: V_{g1}, V_{g2}, V_{g3} are side gates used to control the excess charge on each dot; n_1, n_2 represent the number of excess electrons in the two dots; V_{p1}, V_{p2}, V_{p3} are point contact gates used to control both the dot-lead and dot-dot conductances. Images taken from [50].

Considering a multiple-dot structure, two-qubits gates can be realized by electrical gating of the tunneling barrier between two neighboring quantum dots. A well-established technique in order to realize such structures is the so called split-gate technique shown in Fig.

1.2 [50]. Here, electrons are confined in the two central regions (dots) through gates with different roles: side gates, such as V_{g1}, V_{g2}, V_{g3} in Fig. 1.2(b), control the excess charge on each dot whereas point contact gates, such as V_{p1}, V_{p2}, V_{p3}, allow to control the dot-lead and dot-dot conductances. The idea behind this is that, when the tunneling barrier is high enough, no tunneling occurs and the qubit states are held stably without evolution in time, whereas if it is properly decreased, tunneling may happen, and the spins of the single electron dots will be subjected to a Heisenberg coupling which allows the realization of two qubits operations [21].
The energy balance of a dot coupled with an external electromagnetic field in view of a possible quantum battery implementation has also been studied recently [29].

1.2.2 Superconducting qubits

Given their importance in this thesis, we dedicate to superconducting qubits a separate section. They are solid-state electrical circuits based on superconducting materials and employing Josephson junctions. This has the twofold advantage of avoiding dissipation and providing non linearity and, consequently, anharmonicity [45]. Since they can be easily integrated with other solid-state circuits [45] they are appealing for readout and scalability purposes [3]. For these reasons, such devices are usually employed in the field of quantum computation, quantum information processing and circuit Quantum Electrodynamics (circuit QED) [51, 52].
Different possible implementations of superconducting qubits have been proposed in literature. They can be divided in charge qubits, flux qubits, phase qubits [52] and the transmon qubits [22, 52] depending on the circuit implementation and working conditions. Here, we will only focus on charge and transmon qubits. A detailed description of the other classes of superconducting qubits can be found in [45, 52, 53]. Before entering into the detailed analysis of these circuits, as a warm up, in the following we will briefly describe a simple but instructive electrical circuit in the quantum regime, namely the LC circuit.

LC circuit It constitutes the simplest example of a circuit which, under proper conditions, displays a quantum behaviour. It can be described as an inductor L connected with a capacitor C, with all metal parts made of a superconducting material [45]. This allows to get rid of resistive contributions for temperature below the superconducting critical temperature of the material.
Such a device, represented in Fig. 1.3(a), can be seen as the lumped element version of a superconducting cavity or a transmission line resonator [51]. At sufficiently low temperatures, it exhibits quantum features such as a harmonic energy level structure with frequency given by

$$\omega_r = \frac{1}{\sqrt{LC}}. \tag{1.2.2}$$

This feature makes this system a remarkable example of mesoscopic quantum system: it presents a quantum behaviour with parameters linked to engineered quantities, as expressed in Eq. (1.2.2). A detailed theoretical description of its quantum Hamiltonian will be carried out in Sec. 1.3. Such circuits can be realized using planar components with size of about 100 μm (see Fig. 1.3(b)) and with typical $L \approx 10\ nH$ and $C \approx 1\ pF$ [45] leading to $\omega_r \approx 10\ GHz$.

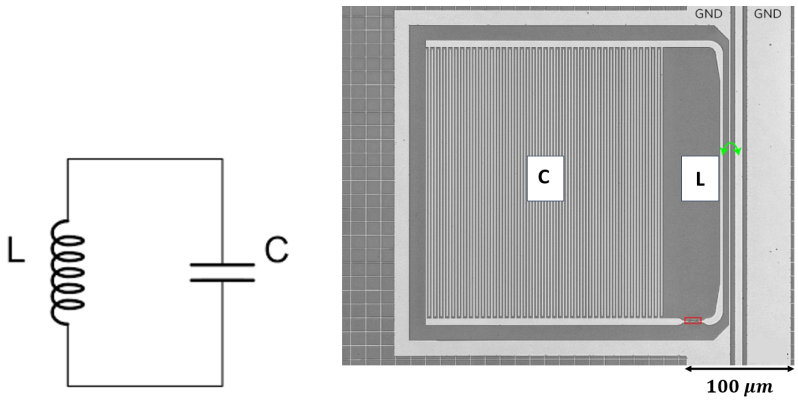

(a) (b)

Figure 1.3: (a): Lumped elements scheme for an LC circuit. Here, L denotes the inductance of the circuit whereas C its capacitance. Image taken from [45]. (b): Laser microscope image of the lumped-element LC oscillator inductively coupled to a coplanar transmission line (on the right). Image taken and adapted from [54]

In order to employ the LC circuit in more complicated geometries for quantum computation purposes, one needs to ensure that it maintains superconducting features in the regime where qubits need to be employed. Usual applications take place at temperatures around $T \approx 1 - 10\ mK$ and qubit state measurements are performed using pulses of frequencies on the order of $10 - 20\ GHz$. Employing a suitable superconducting material with critical temperature above T and no dissipative effects for frequencies considered above ensures the possibility of employing this circuit for quantum computation purposes. An example of a suitable material is aluminium: its critical temperature is $T_C \approx 1.1$ K and the frequency at which dissipation due to the breaking of Cooper pairs occurs is $\omega_{diss} = 100\ GHz$, values which are sufficiently far from the qubits scales anticipated above. Such values of the LC circuits parameters, for which we refer to [45], allow these systems to present characteristic impedance values which make them easy to couple with other superconducting circuits [45].
The possibility of realizing harmonic level structures through the use of superconducting circuits, however, is not useful in order to realize artificial atoms. It is, in fact, impossible to isolate only two levels out of a harmonic structure [45, 52]. For this reason, a source of non linearity is needed.

Josephson junction The need for the introduction of such a new element derives from the fact that, for an integrated circuit to be employed as qubit, no dissipation nor linearity is acceptable: the first is linked to the loss of quantum coherence whereas the latter to harmonicity of energy spectra as stated above. The problem of dissipation can be overcome by employing superconducting materials with suitable critical temperature, whereas non-linearity can be achieved by employing Josephson junctions. Introduced for the first time by B.D. Josephson [57, 58], these are non dissipative and non linear circuit elements which can be used at low temperature.
The structure of a Josephson junction is shown in Fig. 1.4(a): it is formed by two superconducting materials separated by a thin insulating layer, usually an oxide layer with typical width scale of 1 nm. The functioning of this device is based on Cooper pairs tunneling through the barrier [55].

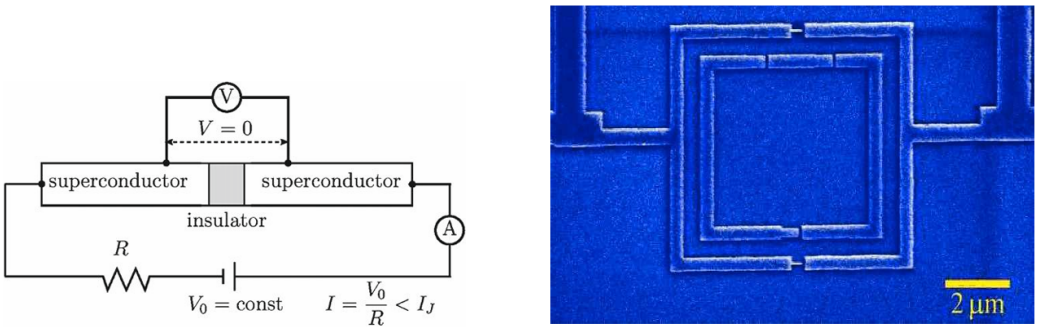

(a) (b)

Figure 1.4: (a): circuital scheme of a Josephson junction. Image taken from [55]. (b): superconducting qubit (inner loop) inserted into a 2-junction SQUID (external loop) which works as a readout device. Image taken from [56].

Here, we limit ourselves to introduce relevant equations and parameters for Josephson junctions. At the typical frequencies and temperatures of qubit operations it behaves as a non linear inductor $L^{(JJ)}$ with an associated capacitance $C^{(JJ)}$ due to the superconducting (SC) electrodes. It is interesting to study its constitutive equations, namely

$$I_J(t) = I_C \mathrm{Sin}[\varphi(t)] \tag{1.2.3}$$

$$\frac{\partial \varphi(t)}{\partial t} = \frac{2\pi}{\phi_0} V(t) \tag{1.2.4}$$

which are usually referred to as Josephson equations [55, 59]. Here we introduced the critical current of the junction I_C, which depends on the SC material and the size of the junction, the gauge invariant phase difference φ across the junction, the applied voltage $V(t)$, and the superconducting flux quantum $\phi_0 = \frac{h}{2e} \approx 2.07 \times 10^{-15}\ Wb$. It can be shown [60] that the inductance of such a junction and its inductive energy are given by

$$L^{(JJ)} = \left(\frac{\partial I_J}{\partial t}\right)^{-1} V(t) = \frac{1}{\mathrm{Cos}(\varphi(t))} \frac{\phi_0}{2\pi I_C} \tag{1.2.5}$$

and

$$E_{JL} = \int_0^t I(t')V(t')dt' = E^{(JJ)}(1 - \mathrm{Cos}(\varphi(t))) \tag{1.2.6}$$

respectively. Here

$$E^{(JJ)} = \frac{\phi_0}{2\pi} I_C \tag{1.2.7}$$

represents the energy scale of the inductive contribution. On the other hand the capacitive energy is given by

$$E_C = \frac{Q^2}{2C^{(JJ)}} \tag{1.2.8}$$

where Q is the charge of the junction, namely the charge of the Cooper pairs which undergo the tunneling process between the two superconducting materials forming the junction [55]. Typically $C^{(JJ)} \approx 1\ pF$ [60].
Two Josephson junctions can be connected in parallel through a superconducting loop in

order to realize the so called SQUIDs (Superconducting Quantum Interference Devices) [45, 60]. These are important not only for the realization of qubits, but also for their readout processes, due to their sensitivity to small magnetic fields. As shown in [53, 56] they can be combined in circuital schemes which, coupled with the superconducting qubit, are able to measure its state. Fig 1.4(b) displays an example of this situation: a 3-junction superconducting qubit is inserted into a SQUID [56] which performs the readout of the qubit by measuring the magnetic flux through it.
Assuming the junctions to be identical, the capacitive energy of a SQUID is of the same form of Eq. (1.2.8) with a total capacitance $C_J = 2C^{(JJ)}$. For what concerns its inductive Josephson energy, it can be evaluated by inserting in Eq. (1.2.6) the expression for the total superconducting current flowing in a SQUID loop composed by two superconducting electrodes A and B connected through two identical Josephson Junctions, 1 and 2 (see Fig. 1.5).

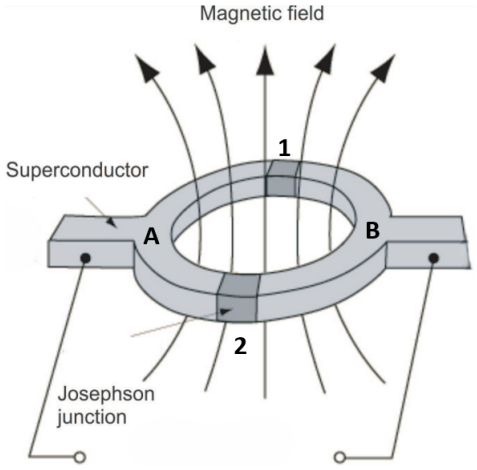

Figure 1.5: Schematic representation of a SQUID loop: two superconducting electrodes (light grey) are connected through two Josephson junctions (dark grey).

The total superconducting current is thus given by [55, 61]

$$\begin{aligned} I_J &= I_C(\mathrm{Sin}(\varphi_{2,A} - \varphi_{2,B}) + \mathrm{Sin}(\varphi_{1,A} - \varphi_{1,B})) = \\ &= I_C(\mathrm{Sin}(\Delta\varphi_2) + \mathrm{Sin}(\Delta\varphi_1)). \end{aligned} \tag{1.2.9}$$

In the presence of an external magnetic field, in fact, φ is not homogeneous in a superconducting electrode. It is possible to show that for a given superconducting electrode the following relation holds [55]

$$\vec{\nabla}\varphi(\vec{r}) = \frac{2\pi}{\phi_0}\vec{A}(\vec{r}) \tag{1.2.10}$$

with $\vec{A}(\vec{r})$ the vector potential and $\vec{r}$ the position considered in the electrode. This allows us to write

$$\varphi_{2,A} - \varphi_{1,A} = \frac{2\pi}{\phi_0}\int_1^2 \vec{A}(\vec{r})\cdot d\vec{r} \tag{1.2.11}$$

$$\varphi_{1,B} - \varphi_{2,B} = \frac{2\pi}{\phi_0}\int_2^1 \vec{A}(\vec{r})\cdot d\vec{r}. \tag{1.2.12}$$

Rewriting Eq. (1.2.9) as

$$I_J = 2I_C \mathrm{Sin}\left(\frac{\Delta\varphi_2 + \Delta\varphi_1}{2}\right)\mathrm{Cos}\left(\frac{\Delta\varphi_2 - \Delta\varphi_1}{2}\right) \tag{1.2.13}$$

and using Eqs. (1.2.11) and (1.2.12) one obtains

$$I_J = I_{max}\mathrm{Sin}\left(\frac{\Delta\varphi_2 + \Delta\varphi_1}{2}\right) \tag{1.2.14}$$

with

$$I_{max} = 2I_C \mathrm{Cos}\left(\frac{\pi\phi}{\phi_0}\right). \tag{1.2.15}$$

Here, ϕ stands for the external magnetic flux through the SQUID ring. Comparing Eq. (1.2.14) with Eq. (1.2.3) we see that the Josephson current of a SQUID has the same form of the Josephson current of a junction provided that we redefine

$$\varphi = \frac{\Delta\varphi_2 + \Delta\varphi_1}{2} \tag{1.2.16}$$

$$I_C = I_{max} \tag{1.2.17}$$

Inserting Eq. (1.2.14) for the superconducting current of the SQUID in Eq. (1.2.6) allows us to evaluate its Josephson energy as [55, 60]

$$E_{JL} = E_J(1 - \mathrm{Cos}(\varphi)) \tag{1.2.18}$$

with φ given by Eq. (1.2.16) and

$$E_J = 2E^{(JJ)}\mathrm{Cos}\left(\frac{\pi\phi}{\phi_0}\right), \tag{1.2.19}$$

which can be tuned changing the magnetic field through the SQUID.

Josephson qubits Usual implementations of such devices in the field of quantum bits requires the introduction of a gate potential V_g coupled with the system considered through a gate capacitance C_g. Therefore, relevant parameters for the characterization of these devices are

$$E_J = \frac{\phi_0 I_C}{2\pi} \tag{1.2.20}$$

$$E_C = \frac{e^2}{2C_{tot}} \tag{1.2.21}$$

with $C_{tot} = C_g + C_J$.

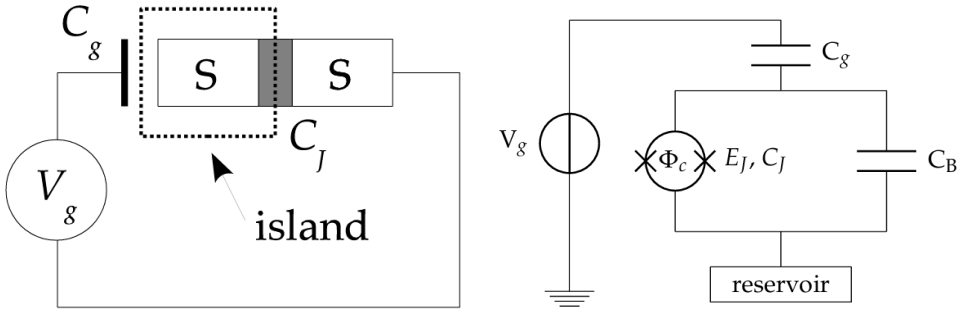

(a) (b)

Figure 1.6: (a): circuital scheme of a Cooper Pair Box (CPB). (b): circuital scheme of a transmon qubit: a SQUID shunted by a large capacitance C_B. Images taken from [60].

In Fig. 1.6 two examples of such platforms are shown. The circuit shown in Fig. 1.6(a) is the so called *charge qubit*. Here, a superconducting electrode (*island*) is connected to a superconducting reservoir through an intermediate device (the grey region) which can be both a Josephson junction or a SQUID. The tunneling of Cooper pairs towards the island may occur as response to the gate voltage. In its working regime, namely $E_J \ll E_C$, this system allows to isolate a two-level system thanks to its anharmonicity. The main problem of this device is its sensitivity to the gate voltage fluctuations. For this reason it is worth exploring the opposite regime $E_J \gg E_C$. It can be achieved by connecting a SQUID in parallel with a large capacitance C_B whose role is to reduce E_C in order to reduce charge fluctuations related to the gate voltage. This kind of circuit is usually referred to as *transmon qubit*, which is depicted in Fig. 1.6(b). Typical values which allow suitable anharmonicity and stability with respect to gate fluctuations are within the range $20 \lesssim \frac{E_J}{E_C} \ll 5 \times 10^4$ [60].
We conclude this introductory section on superconducting circuits by observing that, given their operational temperatures in the interval $T \approx \mu K \div 10mK$ [20], it is possible, as an initial approximation, to neglect contributions due to thermal excitations.

1.2.3 Decoherence

The coupling between a qubit and an external environment causes detrimental effects on the functionality of the device and must be taken into account in order to properly analyze physical implementations of two-level systems.
For the theoretical treatment of the problem of a quantum system coupled with an external environment we refer the reader to Chapter 2. For now, we only carry out a brief description of the main *Decoherence* effects affecting qubits.
The term *Decoherence* refers to the class of phenomena caused by the uncontrolled interaction between a quantum system and its environment. This may cause stochastic fluctuations in physical parameters which can lead to loss of quantum information and loss of stability of the qubit features. The main effects which can be observed in a qubit are known as *Relaxation* and *Dephasing* [43, 52].
Relaxation phenomena are due to the spontaneous loss of energy of the qubit, whereas the dephasing is due to the random change of the qubit phase due to the environment. The decoherence time T_1 is defined as the time scale over which the qubit returns to its ground

state due to relaxation, whereas the dephasing time T_2 is the time scale over which the qubit phase coherence is lost.
In order to minimize the effects of such processes, it would be desirable to act on the system with characteristic operation times t_{op} much shorter than T_1 and T_2.
Typical values of these times are:

- **trapped ions:** $T_1, T_2 \approx 1 \div 10\ s$ [20];
- **quantum dots:** $T_1, T_2 \approx 10\ ms$ [21];
- **charge qubits:** $T_1 \approx 10^{-2} \div 10^{-1}\ \mu s$, $T_2 \approx 10^{-2}\ \mu s$ [62];
- **transmon qubits:** $T_1, T_2 \approx 100\ \mu s$ [62].

These are much greater than the duration of pulses typically used to control these systems. In particular, superconducting qubits such as transmons display sufficiently long coherence times for quantum computation purposes even though they show much shorter decoherence times than systems such as trapped ions. This is because the range of their operation time is $1 \div 10\ ns$, much shorter than the corresponding values for T_1 and T_2 displayed above, a fact that guarantees the possibility of realizing a great number of operations on the qubit before loosing quantum coherence.

1.2.4 Cavities and resonators

The integration of superconducting qubits into more complex circuits for readout and scalability purposes usually requires elements such as cavities and resonant circuits. We have already introduced their simplest example, namely the LC circuit, composed by only two distinct circuital elements.
However, it is possible to realize more sophisticated versions of a resonant circuit based on distributed circuital elements. These are built differently with respect to lumped circuit elements (inductances, capacitances) but show similar effective inductive or capacitive behaviour. Distributed versions of resonant circuits are known as transmission lines or waveguide resonators [51]. Their most simple planar scheme is represented in Fig. 1.7.

A central superconducting electrode of width w is separated from two ground superconducting electrodes of the same material by a distance s. This structure supports the formation of transverse electromagnetic modes with a set of frequencies $\{\omega_m\}$. In order to use these devices to manipulate qubits we need to enter the quantum regime for such modes, operating at temperatures such that $\hbar\omega_0 \gg k_B T$, with ω_0 being the lowest frequency mode. As already discussed above, for typical frequencies of qubit manipulations, namely $\omega_0 \approx 1 \div 10\ GHz$, the temperature scale needed is $1 \div 10\ mK$, within reach for a cryogenic apparatus and far below the critical temperatures of materials usually employed, such as niobium and aluminium [51].
It can be shown that a capacitive coupling between the single mode of a resonator and a transmon [22, 63] or charge qubit [60] can be realized and that controlling the quantum electromagnetic field of the resonator allows to perform qubit operations.
Such devices are also promising platforms for the realization of quantum batteries or chargers, given their harmonic modes structure [14, 33].
We will explore these last two points more in detail in Sec. 1.3.3 and Sec. 1.5.2.

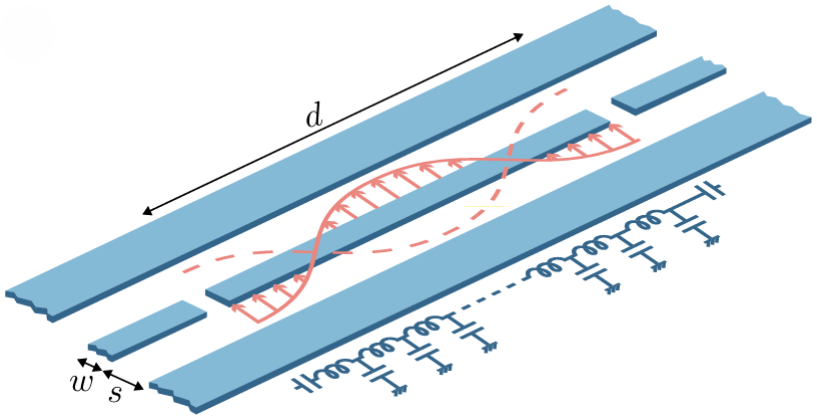

Figure 1.7: Schematic layout of a coplanar waveguide resonator. Here w is the width of the central superconducting electrode, s is the separation between this and the lateral electrodes and d is the longitudinal length of the waveguide resonator. Image taken from [51].

1.3 Setting the quantum mechanical framework

Now that we have introduced significant platforms for our purposes and before proceeding further towards the characterization of quantum batteries, it is worth recalling the mathematical tools needed in order to describe such systems.

1.3.1 Two-level systems

In this Section we theoretically analyze two-level systems which are the building blocks of most of the models describing quantum devices and, in particular, batteries. They are quantum systems with a two dimensional Hilbert's space $\mathscr{H}_{TLS}$ and their simplest description can be carried out considering the following basis for the Hermitian operators acting on such systems

$$\left\{\mathbb{I} \equiv \hat{\sigma}_0, \hat{\sigma}_x, \hat{\sigma}_y, \hat{\sigma}_z\right\} \tag{1.3.1}$$

where $\mathbb{I}$ is the identity operator and $\hat{\sigma}_x, \hat{\sigma}_y, \hat{\sigma}_z$ are the Pauli's operators. This implies that every Hermitian operator acting on $\mathscr{H}_{TLS}$ can be written as

$$\hat{O} = O_0\mathbb{I} + \vec{d_O} \cdot \vec{\sigma} \tag{1.3.2}$$

with $\vec{d_O}$ formed by three real components and $\vec{\sigma} = (\hat{\sigma}_x, \hat{\sigma}_y, \hat{\sigma}_z)$. The most common choice for the two dimensional basis describing the TLS corresponds to the basis of eigenvectors of $\hat{\sigma}_z$ which can be represented in a spinorial notation by

$$|+\rangle = \begin{pmatrix} 1 \\ 0 \end{pmatrix} \quad |-\rangle = \begin{pmatrix} 0 \\ 1 \end{pmatrix}. \tag{1.3.3}$$

This leads to the following representation of Pauli's operators

$$\hat{\sigma}_x = \begin{pmatrix} 0 & 1 \\ 1 & 0 \end{pmatrix} \quad \hat{\sigma}_y = \begin{pmatrix} 0 & -i \\ i & 0 \end{pmatrix} \quad \hat{\sigma}_z = \begin{pmatrix} 1 & 0 \\ 0 & -1 \end{pmatrix}. \tag{1.3.4}$$

It is straightforward to observe that these are traceless, Hermitian operators with eigenvalues ± 1. They also satisfy the following commutation and anticommutation relations

$$[\hat{\sigma}_i, \hat{\sigma}_j] \equiv \hat{\sigma}_i\hat{\sigma}_j - \hat{\sigma}_j\hat{\sigma}_i = 2i\epsilon_{ijk}\hat{\sigma}_k \tag{1.3.5}$$

$$\{\hat{\sigma}_i, \hat{\sigma}_j\} \equiv \hat{\sigma}_i\hat{\sigma}_j + \hat{\sigma}_j\hat{\sigma}_i = 2\delta_{ij}\mathbb{I}. \tag{1.3.6}$$

Denoting with Δ the energy difference between the two states of the system and assuming $\hbar = 1$ (which will be implicit hereafter) the Hamiltonian describing it can be expressed as

$$\hat{H}_{TLS} = \frac{\Delta}{2}\hat{\sigma}_z. \tag{1.3.7}$$

The state of a TLS can be given by every possible quantum superposition of $|+\rangle$ and $|-\rangle$ which, in its most general and normalized form can be written as

$$|\psi\rangle = \mathrm{Cos}\left(\frac{\theta}{2}\right)|+\rangle + \mathrm{Sin}\left(\frac{\theta}{2}\right)e^{i\phi}|-\rangle \tag{1.3.8}$$

with $\theta \in [0, \pi]$ and $\phi \in [0, 2\pi]$. This equation defines a mapping between the TLS pure states and the surface of a 3D sphere referred to as Bloch sphere (see Fig. 1.8). Thus, each state of a TLS corresponds to a point on the Bloch sphere. A complete description of a TLS taking into account also mixed states can be carried out by studying its density matrix [64]. Denoting it as $\hat{\rho}$, it is a hermitian, positive and unit trace operator which must also satisfy $\det\{\hat{\rho}\} \geq 0$ and $\mathrm{Tr}\{\hat{\rho}^2\} \leq 1$. If the state is pure, then $\det\{\hat{\rho}\} = 0$ and $\mathrm{Tr}\{\hat{\rho}^2\} = 1$.
We observe that the most general form of a TLS density matrix satisfying the above condition can be written in the form of Eq. (1.3.2) as [64]

$$\hat{\rho} = \frac{1}{2}\big(\mathbb{I} + \vec{d}_\rho \cdot \vec{\sigma}\big). \tag{1.3.9}$$

It is straightforward to show [64] that the purity conditions $\det\{\hat{\rho}\} = 0$ and $\mathrm{Tr}\{\hat{\rho}^2\} = 1$ hold if and only if $|\vec{d}_\rho| = 1$. Given a pure state of the form in Eq. (1.3.8) the corresponding density matrix is given by

$$\hat{\rho} = |\psi\rangle\langle\psi| = \begin{pmatrix} \mathrm{Cos}^2\big(\frac{\theta}{2}\big) & e^{-i\phi}\mathrm{Sin}\big(\frac{\theta}{2}\big)\mathrm{Cos}\big(\frac{\theta}{2}\big) \\ e^{i\phi}\mathrm{Sin}\big(\frac{\theta}{2}\big)\mathrm{Cos}\big(\frac{\theta}{2}\big) & \mathrm{Sin}^2\big(\frac{\theta}{2}\big) \end{pmatrix} \tag{1.3.10}$$

$$= \frac{1}{2}\begin{pmatrix} 1 + \mathrm{Cos}(\theta) & \big(\mathrm{Cos}(\phi) - i\mathrm{Sin}(\phi)\big)\mathrm{Sin}(\theta) \\ \big(\mathrm{Cos}(\phi) + i\mathrm{Sin}(\phi)\big)\mathrm{Sin}(\theta) & 1 - \mathrm{Cos}(\theta) \end{pmatrix}$$

$$= \frac{1}{2}\Big[\mathbb{I} + \mathrm{Sin}(\theta)\mathrm{Cos}(\phi)\hat{\sigma}_x + \mathrm{Sin}(\theta)\mathrm{Sin}(\phi)\hat{\sigma}_y + \mathrm{Cos}(\theta)\hat{\sigma}_z\Big].$$

This last expression confirms what anticipated: the vector $\vec{d}_\rho$ representing a pure state density matrix is such that $|\vec{d}_\rho| = 1$. On the contrary, mixed states satisfy $|\vec{d}_\rho| < 1$.

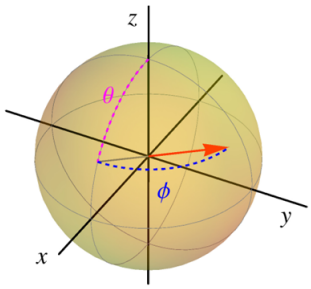

Figure 1.8: Picture of the Bloch sphere: a pure state (red arrow) is represented together with the two angles θ and ϕ which identify it. Mixed states are represented by points internal to the sphere. Image taken from [60].

Before proceeding further, it is worth studying the time evolution of a TLS described by a time-independent Hamiltonian of the form of Eq. (1.3.2), namely

$$\hat{H} = \vec{A} \cdot \vec{\sigma}. \tag{1.3.11}$$

Moreover, consistently to Eq. (1.3.7), we will fix

$$A_z = \frac{\Delta}{2}. \tag{1.3.12}$$

The first two components of $\vec{A}$ can be interpreted as an external field. The time evolution of this system is ruled by the following unitary operator in Schrödinger's picture [64]

$$|\psi(t)\rangle = \hat{U}(t,0)\,|\psi(0)\rangle \tag{1.3.13}$$

$$\hat{U}(t,0) = e^{-it\vec{A}\cdot\vec{\sigma}}. \tag{1.3.14}$$

We now define the unit vector $\vec{n}$ such that $\vec{A} = A\vec{n}$ with $A = \sqrt{A_x^2 + A_y^2 + A_z^2}$ so that the unitary operator defined in Eq. (1.3.14) becomes [65]

$$\hat{U}(t,0) = e^{-itA\vec{n}\cdot\vec{\sigma}} = \mathrm{Cos}(At)\mathrm{I} - i\mathrm{Sin}(At)\vec{n}\cdot\vec{\sigma}. \tag{1.3.15}$$

In the $\hat{\sigma}_z$ basis it reads

$$\hat{U}(t,0) = \begin{pmatrix} \mathrm{Cos}(At) - i\mathrm{Sin}(At)\frac{\Delta}{2A} & -i\mathrm{Sin}(At)\frac{A_x - iA_y}{A} \\ i\mathrm{Sin}(At)\frac{A_x + iA_y}{A} & \mathrm{Cos}(At) + i\mathrm{Sin}(At)\frac{\Delta}{2A} \end{pmatrix}. \tag{1.3.16}$$

Thus, starting from Eq. (1.3.8) the evolved state at a time t is

$$|\psi(t)\rangle = \begin{pmatrix} \mathrm{Cos}(At) - i\mathrm{Sin}(At)\frac{\Delta}{2A} & -i\mathrm{Sin}(At)\frac{A_x - iA_y}{A} \\ i\mathrm{Sin}(At)\frac{A_x + iA_y}{A} & \mathrm{Cos}(At) + i\mathrm{Sin}(At)\frac{\Delta}{2A} \end{pmatrix} \begin{pmatrix} \mathrm{Cos}\frac{\theta}{2} \\ e^{i\phi}\mathrm{Sin}\frac{\theta}{2} \end{pmatrix}. \tag{1.3.17}$$

Since the evolution operator is given by a unitary matrix, the norm of the state is preserved, as it can be verified.
One interesting feature of this model is that it shows a non zero transition probability

between $|-\rangle$ and $|+\rangle$. This can be seen by computing the probability $P_+(t)$ of finding the system in the state $|+\rangle$ at a time t, assuming as an initial state $|\psi(0)\rangle = |-\rangle$. In this case the evolved state is given by

$$|\psi(t)\rangle = \begin{pmatrix} -i\text{Sin}(At)\frac{A_x - iA_y}{A} \\ \\ \text{Cos}(At) + i\text{Sin}(At)\frac{\Delta}{2A} \end{pmatrix} \tag{1.3.18}$$

$$= -i\text{Sin}(At)\frac{A_x - iA_y}{A}|+\rangle + \left(\text{Cos}(At) + i\text{Sin}(At)\frac{\Delta}{2A}\right)|-\rangle$$

which immediately leads to the following transition probability

$$P_+(t) = |\langle +|\psi(t)\rangle|^2 = \frac{A_x^2 + A_y^2}{\frac{\Delta^2}{4} + A_x^2 + A_y^2}\text{Sin}^2(At). \tag{1.3.19}$$

These oscillations in the transition probabilities are usually referred to as *Rabi's Oscillations* [64].

1.3.2 Harmonic systems

We describe here the quantization of harmonic systems such as the LC oscillator and the transmission lines introduced in Sec. 1.2.2 and 1.2.4 respectively.

Quantum LC circuit We consider here the LC circuit shown in Fig. 1.3. Denoting with V and I respectively the voltage applied to the capacitor and the current flowing in the circuit we can write the classical energy of the circuit as

$$E_{cl} = E_C + E_L = \frac{CV^2}{2} + \frac{LI^2}{2} = \frac{Q^2}{2C} + \frac{\Phi^2}{2L} \tag{1.3.20}$$

where, in the last equality, we used the relations $Q = CV$ for the charge of the capacitance and $\Phi = LI$ for the magnetic flux through the circuit. Defining $\omega_r = \frac{1}{\sqrt{LC}}$ we obtain

$$E_{cl} = \frac{Q^2}{2C} + \frac{C\omega_r^2\Phi^2}{2} \tag{1.3.21}$$

which has the same form of the energy of a classical Harmonic oscillator with mass $m \equiv C$, conjugate variables $X \equiv \Phi$ and $P \equiv Q$ and frequency ω_r. Its quantization can be performed introducing of two Hermitian operators $\hat{Q}$ and $\hat{\Phi}$ as quantum conjugate variables satisfying

$$\left[\hat{\Phi}, \hat{Q}\right] = i\mathbb{I}. \tag{1.3.22}$$

Thus, the quantum Hamiltonian reads

$$\hat{H} = \frac{\hat{Q}^2}{2C} + \frac{C\omega_r^2\hat{\Phi}^2}{2}. \tag{1.3.23}$$

We now rewrite this by introducing the annihilation and creation operators, $\hat{a}$ and $\hat{a}^\dagger$, defined by the following relations

$$\hat{Q} = i\sqrt{\frac{\omega_r C}{2}}(\hat{a}^\dagger - \hat{a}) \tag{1.3.24}$$

$$\hat{\Phi} = \sqrt{\frac{1}{2\omega_r C}}(\hat{a} + \hat{a}^\dagger) \tag{1.3.25}$$

and which satisfy

$$\left[\hat{a}, \hat{a}^\dagger\right] = \mathbb{I}. \tag{1.3.26}$$

Performing this substitution we obtain a standard quantum harmonic oscillator Hamiltonian [65]

$$\hat{H} = \omega_r\left(\hat{a}^\dagger\hat{a} + \frac{\mathbb{I}}{2}\right). \tag{1.3.27}$$

This Hamiltonian describes the LC circuit in the quantum regime. We recall that this can be achieved at proper operational conditions already discussed in Sec. 1.2.2. The operator

$$\hat{N} = \hat{a}^\dagger\hat{a} \tag{1.3.28}$$

is the usual *Number operator* [65]. Denoting with $\{|n\rangle\}$, $n \in \mathbb{N}$ its eigenbasis such that $\hat{N}|n\rangle = n|n\rangle$, we recall that

$$\hat{a}|n\rangle = \sqrt{n}\,|n-1\rangle \tag{1.3.29}$$

$$\hat{a}^\dagger|n\rangle = \sqrt{n+1}\,|n+1\rangle \tag{1.3.30}$$

$$\hat{H}|n\rangle = \omega_r\left(n + \frac{1}{2}\right)|n\rangle \equiv E_n|n\rangle\,. \tag{1.3.31}$$

with $n \geq 0$.

Transmission lines Distributed resonant circuits can be quantized following a similar procedure [51]: after modeling them as series of lumped circuital elements, one proceeds to decompose them as the sum of contributions corresponding to different electromagnetic modes. Therefore, the quantization of this system results in a collection of quantum harmonic oscillators with frequencies $\{\omega_m\}$, with the index $m \in \mathbb{N}$ denoting the considered mode, and Hamiltonian

$$\hat{H} = \sum_m \omega_m\left(\hat{a}_m^\dagger\hat{a}_m + \frac{\mathbb{I}}{2}\right). \tag{1.3.32}$$

1.3.3 Superconducting Circuits

After having discussed the quantization of an LC circuit we theoretically analyze here the possibility of realizing a qubit by employing superconducting circuits, discussing how an effective two-level system Hamiltonian can be derived in various regimes.

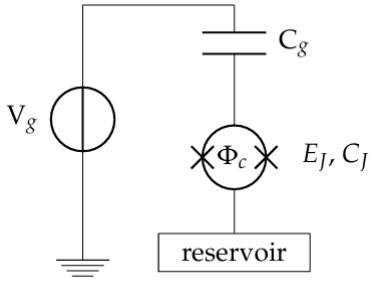

Figure 1.9: Scheme of a SQUID shunted by a gate capacitance C_g connected to a gate voltage V_g. Here, Φ_c represents an external magnetic flux through the SQUID, C_J its capacitance and E_J its inductive energy scale. Image taken from [60].

SQUID Hamiltonian Let us consider the circuital configuration in Fig. 1.9.
From now on, we will denote with E_J and C_J the SQUID inductive energy and Josephson capacitance which are linked to the single junction parameters $E^{(JJ)}$ and $C^{(JJ)}$ through

$$C_J = 2C_J^{(JJ)} \tag{1.3.33}$$

$$E_J = 2E^{(JJ)}\mathrm{Cos}\left(\frac{\pi\phi_c}{\phi_0}\right) \tag{1.3.34}$$

as discussed in Sec. 1.2.2. Recalling Eq. (1.2.18) for the inductance energy of a SQUID, its classical Hamiltonian is given by [51, 60]

$$H_{cl} = \frac{(Q-Q_g)^2}{2C_{tot}} - E_J\mathrm{Cos}(\varphi) \tag{1.3.35}$$

where Q is the charge of the Cooper pairs in the Junctions, φ is the Gauge invariant phase difference between the two superconducting electrodes of the SQUID and $Q_g = C_gV_g$ is the charge of the gate capacitance which is used to control the global charge of the junction. Since the capacitive energy is due to the excess of Cooper's pairs in the junctions, we can write $Q = 2eN$ introducing the number of pairs $N \in (-\infty, +\infty)$. Defining $E_C = \frac{e^2}{2C_{tot}}$ Eq. (1.3.35) can be rewritten as

$$H_{cl} = 4E_C(N-N_g)^2 - E_J\mathrm{Cos}(\varphi). \tag{1.3.36}$$

Treating N and φ as conjugate variables this Hamiltonian can be quantized by introducing their corresponding Hermitian operators $\hat{N}$ and $\hat{\varphi}$ with the following requirement [22, 60]

$$\left[\hat{\varphi}, \hat{N}\right] = i\mathbb{I}. \tag{1.3.37}$$

Thus, the quantum Hamiltonian of the considered circuit reads

$$\hat{H} = 4E_C(\hat{N}-N_g)^2 - E_J\mathrm{Cos}(\hat{\varphi}). \tag{1.3.38}$$

It can be exactly diagonalized in the $\hat{\varphi}$ eigenbasis in terms of Mathieu's special functions and its eigenvalues are given in terms of Mathieu's characteristic values as functions of the N_g and $\frac{E_J}{E_C}$ parameters [22, 45]. The first energy levels are represented as functions of

N_g for different values of the parameters in Fig 1.10.
From these figures the anharmonicity of the system clearly emerges. The most striking feature of the energy levels is their dependence from N_g at $E_J \approx E_C$, which makes the system unstable with respect of fluctuations due to the gate potential. This, however, becomes irrelevant if one increases the ratio $\frac{E_J}{E_C}$, leading to the progressive flattening of the energy levels as shown in Figs. 1.10(b-d). In the following we analyze the two opposite regimes $E_C \gg E_J$ and $E_C \ll E_J$.

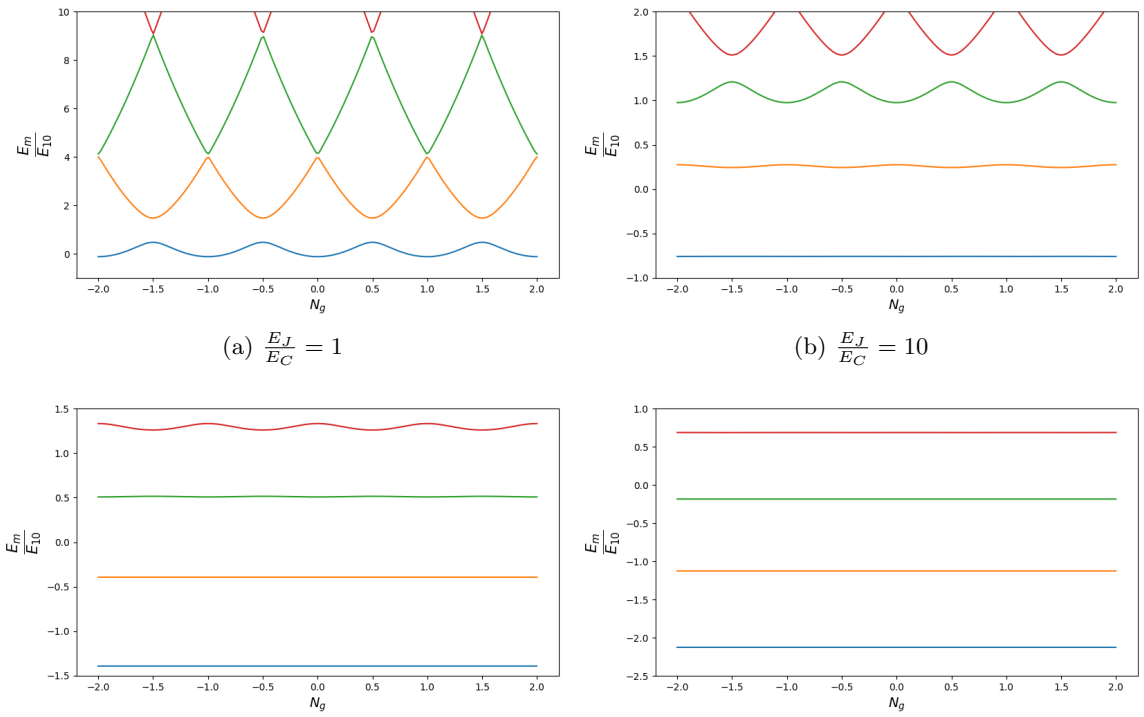

(a) $\frac{E_J}{E_C} = 1$ (b) $\frac{E_J}{E_C} = 10$

(c) $\frac{E_J}{E_C} = 25$ (d) $\frac{E_J}{E_C} = 50$

Figure 1.10: Plots of E_m for $m = 0, 1, 2, 3$ in units of $E_{01} = \min_{N_g}(E_1 - E_0)$ for different ratios of the inductive and capacitive energy scales E_J/E_C.

Charge qubit The circuital implementation which allows to work in the $E_C \gg E_J$ regime (charge regime) was shown in Fig. 1.6a: a superconducting island small enough to have a small capacitance (suitable for the realization of the charge regime) is separated from another superconducting electrode by a tunneling component such as a Josephson junction or a SQUID, the latter being the case we consider here. In the presence of a gate voltage V_g, Cooper pairs may tunnel into the island. For this reason this system is usually referred to as Cooper pair box (CPB). Writing Eq. (1.3.38) as

$$\hat{H} = E_C\left[4(\hat{N} - N_g)^2 - \frac{E_J}{E_C}\mathrm{Cos}(\hat{\varphi})\right]. \tag{1.3.39}$$

and given the predominant role of the capacitive component, this regime can be analyzed using perturbation theory, with perturbation parameter $\frac{E_J}{E_C}$, unperturbed Hamiltonian given by

$$\hat{H}^{(0)}_{CPB} = 4E_C\left(\hat{N} - N_g\right)^2 = \sum_{N=-\infty}^{+\infty} 4E_C(N - N_g)^2 \left|N\right\rangle\!\left\langle N\right|. \tag{1.3.40}$$

and perturbation Hamiltonian

$$\hat{H}_{tun} = -E_J \mathrm{Cos}(\hat{\varphi}) = -\frac{E_J}{2} \sum_{N=-\infty}^{+\infty} |N\rangle\langle N+1| + |N+1\rangle\langle N| \,. \tag{1.3.41}$$

In the second equality of the last equations we expressed both Hamiltonians in terms of the eigenbasis of $\hat{N}$, namely the set $\{|N\rangle\}$ such that $\hat{N}\,|N\rangle = N\,|N\rangle$ with $N \in \mathbb{Z}$, which constitutes the unperturbed Hamiltonian eigenbasis. The unperturbed energy levels $\{E_N\}$, are given by

$$E_N = 4E_C(N - N_g)^2 \tag{1.3.42}$$

which is degenerate when

$$N_g = \frac{1}{2} + N. \tag{1.3.43}$$

For this reason, around these points, we can resort to the degenerate perturbation theory [65]. Since the following relation holds [52, 60]

$$\mathrm{Cos}(\hat{\varphi}) = \frac{1}{2} \sum_{N=-\infty}^{+\infty} |N\rangle\langle N+1| + |N+1\rangle\langle N| \tag{1.3.44}$$

the level $|N\rangle$ is coupled with the two neighboring levels $|N \pm 1\rangle$. In order to consider the effects of this perturbation we are going to focus on the subspace $\{|N\rangle\,, |N+1\rangle\}$ near the degeneracy point, namely setting

$$N_g = \frac{1}{2} + N + \Delta_g \tag{1.3.45}$$

with Δ_g sufficiently small. The reason for this choice of N_g will be clearer at the end of the derivation.
We will treat these degenerate states as if they were decoupled from every other state [52, 60]. This approximation can be made more rigorous by going into the interaction picture where it is possible to demonstrate that the neglected terms contribute only at higher perturbative orders [60].
The restriction of the complete Hamiltonian to the above two dimensional space takes the form

$$\begin{aligned} \hat{H}^{(N)} = 4E_C\Delta_g \Big(|N\rangle\langle N| - |N+1\rangle\langle N+1| \Big) + 4E_C \left(\frac{1}{4} + \Delta_g^2 \right) \\ - \frac{E_J}{2} \Big(|N\rangle\langle N+1| + |N+1\rangle\langle N| \Big). \end{aligned} \tag{1.3.46}$$

The operators in the first and third term of this expression can be represented into the subspace considered as

$$\begin{pmatrix} 1 & 0 \\ 0 & -1 \end{pmatrix} \equiv \sigma_z^{(N)} \tag{1.3.47}$$

$$\begin{pmatrix} 0 & 1 \\ 1 & 0 \end{pmatrix} \equiv \sigma_x^{(N)} \tag{1.3.48}$$

so that, dropping the second term proportional to the identity, we have

$$\hat{H}^{(N)} = \begin{pmatrix} 4E_C\Delta_g & -\frac{E_J}{2} \\ -\frac{E_J}{2} & -4E_C\Delta_g \end{pmatrix}. \tag{1.3.49}$$

Its eigenvalues and eigenvectors are given by

$$|\pm\rangle^{(N)} = \frac{|N+1\rangle \mp |N\rangle}{\sqrt{2}} \tag{1.3.50}$$

$$E_\pm^{(N)} = \pm\frac{E_J}{2}\sqrt{1 + \frac{16E_C^2\Delta_g^2}{E_J^2}}. \tag{1.3.51}$$

This shows that this system can be approximated as a two-level system with $|+\rangle^{(N)}$ and $|-\rangle^{(N)}$ as excited state and ground state respectively, provided that Eq. (1.3.45) holds [60]. Before clarifying what "sufficiently small" means for Δ_g we can observe that:

- if $\Delta_g = 0$, that is, at the degeneracy condition of Eq. (1.3.43) a gap $\Delta E = E_J$ is opened between the two originally degenerate states due to the perturbation (see Fig. 1.11);
- if $\frac{16E_C^2\Delta_g^2}{E_J^2} \ll 1$, a gap is opened which is independent from the gate offset charge up to $o(\Delta_g^2)$, namely $\Delta E = E_J + o(\Delta_g^2)$;
- if $\frac{16E_C^2\Delta_g^2}{E_J^2} \gg 1$ the gap is given by $\Delta E = 2E_C\Delta_g$, which is the same result obtained in the unperturbed case with N_g always given by Eq. (1.3.45).

For what observed in the first two points, the gap of the resulting qubit is almost insensitive to gate fluctuations of N_g provided that one operates near $\Delta_g = 0$. For this reason, N_g values expressed in Eq. (1.3.42) are usually referred to as *sweet spots*.
All considered, Δ_g can be seen as the width of the perturbative effects region, since the perturbation has no effect on the energy gap if $\frac{16E_C^2\Delta_g^2}{E_J^2} >> 1$. It is in this sense, therefore, that it is sufficient to study the perturbative regime near $N_g = N + \frac{1}{2}$ as expressed by Eq. (1.3.45).

Transmon qubit Since it is not always possible to work near sweet spots, it would be of great interest to build a gate-charge insensitive qubit. This can be realized as shown in Fig. 1.6(b), where a SQUID is shunted by an additional large capacitance C_B and connected with a gate capacitance of the same magnitude. The role of such capacitances is to strongly reduce the charging energy according to

$$E_C = \frac{e^2}{2C^{(JJ)} + C_g + C_B} \tag{1.3.52}$$

in order to access the so called transmon regime $E_C \ll E_J$. The transmon Hamiltonian has therefore the same form of that in Eq. (1.3.38), but with E_C defined by Eq. (1.3.52). As shown in Fig. 1.10(d), the gate dependence of the first energy levels is lost already at $\frac{E_J}{E_C} = 50$. By further increasing this value the number of levels independent from N_g

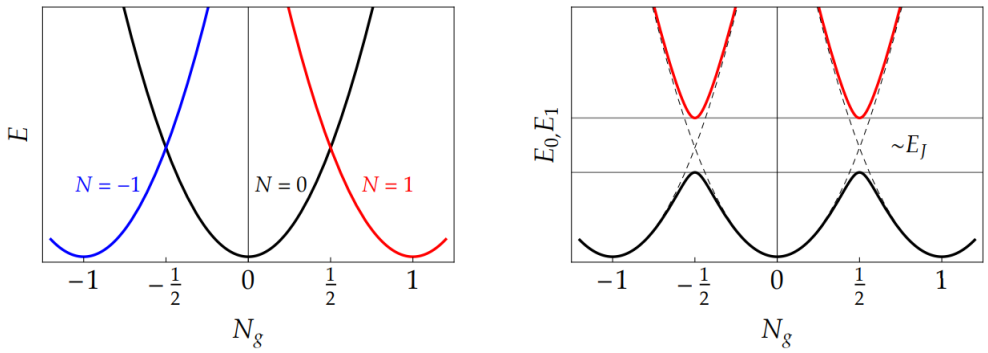

Figure 1.11: Left plot: energy levels of $|N\rangle$ for $E_J = 0$ as functions of N_g. They show a degeneracy at $N_g = (1 + 2N)/2$. Right plot: same quantities for $E_J \neq 0$: two distinct energy levels can be identified: E_0 (black) and E_1 (red). Their energy difference at $N_g = (1 + 2N)/2$ is $\approx E_J$. Image taken from [60].

increases. This is a very important property since it leads to transition frequencies which are unaffected from the gate fluctuations, so that there is no need to force the system to a particular gate regime. This flattening behaviour is evident also by explicit study of the transmon eigenvalues $E_m(N_g)$: they have the same form of the CPB eigenvalues, the only difference being the expression of E_C. As shown in Fig. 1.10, when $\frac{E_J}{E_C} \gtrsim 1$, they present an oscillating structure with period $\delta N_g = 1$ with the amplitude of the oscillations which decreases when $\frac{E_J}{E_C}$ is increased. For this reason, if $\frac{E_J}{E_C} \gg 1$ it is possible to approximate each level E_m as the sum of its intermediate value $E_m(N_g = 1/4)$ plus an oscillating term leading to the following expression [22, 60]

$$E_m(N_g) \approx E_m\left(N_g = \frac{1}{4}\right) - \frac{\epsilon_m}{2}\mathrm{Cos}(2\pi N_g). \tag{1.3.53}$$

Here, the charge dispersion ϵ_m is defined as [22]

$$\epsilon_m(N_g) \equiv E_m\left(N_g = \frac{1}{2}\right) - E_m(N_g = 0) \approx (-1)^m E_C \frac{2^{4m+5}}{m!}\sqrt{\frac{2}{\pi}}\left(\frac{E_J}{2E_C}\right)^{\frac{m}{2}+\frac{3}{4}} e^{-\sqrt{8E_J/E_C}}. \tag{1.3.54}$$

This clarifies that the flattening of the levels in the transmon regime is due to the last exponential factor.
In order to better understand the physics behind the transmon regime we can proceed by Taylor expanding the $\mathrm{Cos}(\hat{\varphi})$ term in the transmon Hamiltonian for small values of $\hat{\varphi}$, namely

$$\begin{aligned} \hat{H}_{tr} &= 4E_C(\hat{N} - N_g)^2 - E_J\mathrm{Cos}(\hat{\varphi}) = \\ &\approx 4E_C(\hat{N} - N_g)^2 + \frac{1}{2}E_J\hat{\varphi}^2 - \frac{E_J}{24}\hat{\varphi}^4. \end{aligned} \tag{1.3.55}$$

This expansion is motivated by the fact that we are considering a system formally analogous to a particle in a cosine well potential which is predominant with respect to the kinetic energy. Thus, it seems reasonable to approximate the well up to the fourth order, since we expect the system to be bound near the bottom of the well [22].
Furthermore, we can eliminate terms depending on N_g since their contributions to the

energy levels are negligible [22, 60] so that we obtain

$$\hat{H}_{tr} \approx 4E_C\hat{N}^2 + \frac{1}{2}E_J\hat{\varphi}^2 - \frac{E_J}{24}\hat{\varphi}^4. \tag{1.3.56}$$

This has the form of a Duffing non linear oscillator Hamiltonian [60] which is composed by a harmonic oscillator part

$$\hat{H}^{(0)} = 4E_C\hat{N}^2 + \frac{1}{2}E_J\hat{\varphi}^2 \tag{1.3.57}$$

and a perturbation

$$\hat{H}^{(1)} = -\frac{E_J}{24}\hat{\varphi}^4. \tag{1.3.58}$$

We can therefore write $\hat{N}$ and $\hat{\varphi}$ in terms of the annihilation and creation operators $\hat{b}$ and $\hat{b}^\dagger$ of a harmonic oscillator

$$\hat{N} = \frac{i}{2}\left(\frac{E_J}{2E_C}\right)^{\frac{1}{4}}\left(\hat{b}^\dagger - \hat{b}\right) = \frac{i}{4}\sqrt{\frac{\omega_p}{E_C}}\left(\hat{b}^\dagger - \hat{b}\right) \tag{1.3.59}$$

$$\hat{\varphi} = \left(\frac{2E_C}{E_J}\right)^{\frac{1}{4}}\left(\hat{b}^\dagger + \hat{b}\right) = 2\sqrt{\frac{E_C}{\omega_p}}\left(\hat{b}^\dagger + \hat{b}\right), \tag{1.3.60}$$

where we introduced the Josephson plasma frequency

$$\omega_p = \sqrt{8E_JE_C}. \tag{1.3.61}$$

Eqs. (1.3.59) and (1.3.60) ensure that, given the usual commutation relation $\left[\hat{b}, \hat{b}^\dagger\right] = \mathbb{I}$, $\hat{N}$ and $\hat{\varphi}$ satisfy

$$\left[\hat{\varphi}, \hat{N}\right] = i\mathbb{I}. \tag{1.3.62}$$

According to this we are left with

$$\hat{H}_{tr} = \omega_p\left(\hat{b}^\dagger\hat{b} + \frac{1}{2}\right) - \frac{E_C}{12}\left(\hat{b}^\dagger + \hat{b}\right)^4 \tag{1.3.63}$$

Since $E_C \ll E_J$ we can apply a perturbative approach, starting from the unperturbed energy levels of $\hat{H}^{(0)}$

$$E_m^{(0)} = \omega_p\left(m + \frac{1}{2}\right) \tag{1.3.64}$$

and computing the first order corrections of these non degenerate levels as

$$\begin{aligned} E_m^{(0)} &= -\langle m|\frac{E_C}{12}\left(\hat{b}^\dagger + \hat{b}\right)^4|m\rangle \\ &= -E_Cm - \frac{1}{2}E_Cm(m-1) - \frac{E_C}{4}. \end{aligned} \tag{1.3.65}$$

Neglecting terms independent from m through the redefinition of the ground state energy we are left with the following expression of the transmon energies at the lowest perturbative order

$$E_m = (\omega_p - E_C)m - \frac{1}{2}E_Cm(m-1) \tag{1.3.66}$$

which leads to the following energy gaps

$$\Delta E_{m+1,m} = E_{m+1} - E_m = (\omega_p - E_C) - E_C m. \tag{1.3.67}$$

This gives a perturbative estimate of the anharmonicity of the system, since it clearly shows that each gap is smaller than the subsequent gap by a quantity E_C, leading to a relative anharmonicity

$$\alpha_r = \sqrt{\frac{E_C}{8E_J}}. \tag{1.3.68}$$

Thanks to this feature it is possible to isolate a two-level system.
Two opposite tendencies emerge from the study of a transmon qubit: if, on the one hand, increasing E_C/E_J leads to a greater anharmonicity which is necessary to realize a qubit, on the other hand, increasing E_J/E_C causes stability with respect to gate fluctuations. For this reason, an intermediate regime is required which can be estimated as follows [22]: the smallest energy scale which need to be accessible experimentally is $\Delta E_{1,0}\alpha_r$. Thus the minimum pulse duration in order to have full coherent control of the system can be estimated as

$$\tau_{p,min} \approx \frac{1}{\Delta E_{1,0}\alpha_r}. \tag{1.3.69}$$

This quantity must remain small with respect to decoherence and dephasing times T_1 and T_2 which are of the order of a few hundreds of nanoseconds, so that reasonably we must have $\tau_{p,min} \approx 10ns$. This corresponds to a maximal anharmonicity of the order $\alpha_r \approx 1/600$ which implies $E_J/E_C \lessapprox 5 \times 10^4$.
Considering results shown in Fig. 1.10 for the flattening of transmon levels, the usual working regime of transmons is indeed [22]

$$20 \lesssim \frac{E_J}{E_C} \lesssim 5 \times 10^4. \tag{1.3.70}$$

Transmon coupled to a resonator We discuss here a possible implementation of a transmon qubit coupled to a resonator, realized by capacitively coupling the qubit with a single mode of a transmission line [44, 63], as depicted in Fig. 1.12.
Supposing that there is only one relevant mode of the resonator which contributes to the coupling, the full Hamiltonian of such circuit is given by [63]

$$\hat{H} = \hat{H}_{tr} + \hat{H}_r + \hat{H}_{int} \tag{1.3.71}$$

with

$$\hat{H}_{tr} = 4E_C(\hat{N} - N_g)^2 - E_J \mathrm{Cos}(\hat{\varphi}) \tag{1.3.72}$$

$$\hat{H}_r = \omega_r \hat{a}^\dagger \hat{a} \tag{1.3.73}$$

$$\hat{H}_{int} = g\hat{N}\left(\hat{a}^\dagger + \hat{a}\right) \tag{1.3.74}$$

where Eq. (1.3.72) is the full Hamiltonian of the transmon and $\hat{a}^\dagger, \hat{a}$ are the ladder operators of the resonant mode defined in Sec 1.3.2. The coupling strength g is determined by circuital elements as

$$g = \frac{2eC_g}{C_{tot}}\sqrt{\frac{\omega_r}{2C_r}} \tag{1.3.75}$$

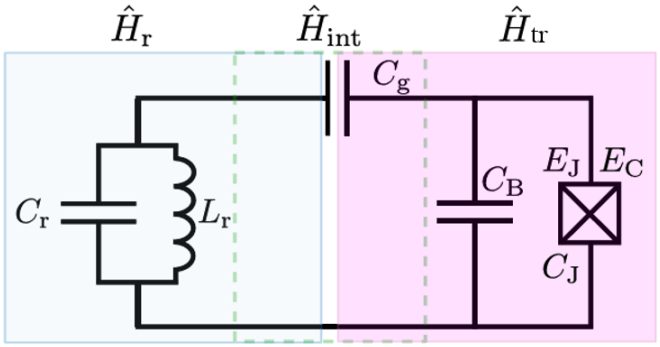

Figure 1.12: Lumped elements scheme for a transmon qubit coupled through a capacitance C_g to a resonator with inductance and capacitance L_r and C_r respectively. The transmon is realized by shunting a SQUID (crossed box) with a large capacitance C_B. E_J and E_C denote respectively the inductive and capacitive energy scales of the qubit. Image taken from [63].

with $C_{tot} = C_g + C_J + C_B$ and $\omega_r = 1/\sqrt{L_r C_r}$ (see Sec. 1.3.2).
The possibility of coupling the qubit with a single mode of the transmission line depends on the relative position of these two devices: the qubit circuit must be realized as near as possible to one of the antinodes (Fig. 1.13) of the electromagnetic mode responsible for the coupling, so that its effect can be maximized.

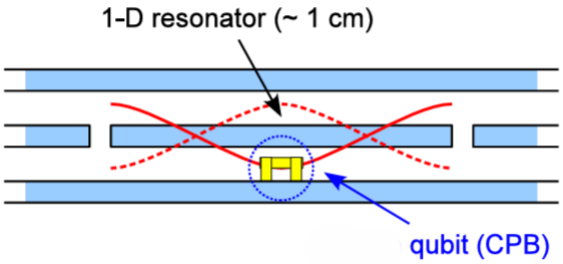

Figure 1.13: Position of the qubit inside the transmission line in order to realize the maximal coupling with a single mode of the electromagnetic field. Image taken from [60]

This circuital scheme is at the basis of Circuit QED [51, 60] and allows the physical implementation of schemes such that discussed in Chapter 3.

1.4 Quantum batteries: generalities and figures of merit

The simplest scheme of a quantum battery is represented by a quantum system for the storage of energy which interacts with another system acting as a charger, which can be both an external classical drive and another quantum system [14]. Typically, the dynamics

of a battery can be divided into two main steps:

- **charging of the battery**, which consists in the interaction with the charger, aimed at transfering energy to the battery;
- **work extraction**, where the charged battery is coupled to suitably engineered systems in order to extract the amount of energy needed.

Many different setup have been proposed in literature, such as two-level system charged by other two-level systems [14], three-level systems charged via an external classical drive [17] and so on.
There have also been proposals for more complex structures of the battery, such as the so called collective quantum batteries, where the energy is stored in a collection of cells [25], but also the collisional ones, where the charging process is performed through sequential interactions with a collection of systems [34]. These will be the main subjects of investigation in the following of the thesis.
The ultimate end of all these works is to show that a quantum advantage can be achieved, both in the charging and discharging processes, due to purely quantum features such as quantum coherences [30] or entanglement, which was the first feature analyzed in this context in the pioneering work by Alicki and Fannes [9].
In the following, we will introduce some key figures of merit for the description of the performances of a battery.

1.4.1 General model of a quantum battery

We start by describing the simplest structure composed by only the battery system S and the charger C. Since more complex structures can be seen as generalizations of this simple model to the case of multiple-cells batteries and multiple chargers ones, it is worth starting the analysis by the single-battery and single-charger case. Denoting with $\hat{H}_S$ and $\hat{H}_C$ respectively the battery and charger Hamiltonian, the global Hamiltonian of the charging process is given by

$$\hat{H}(t) = \hat{H}_S \otimes \mathbb{I}_C + \mathbb{I}_S \otimes \hat{H}_C + \hat{H}_{SC}(t). \tag{1.4.1}$$

This equation clarifies that $\hat{H}_S$ and $\hat{H}_C$ act on the battery and charger Hilbert's spaces $\mathscr{H}_S$ and $\mathscr{H}_C$, whereas the interaction term $\hat{H}_{SC}(t)$ acts on the tensor product of the two spaces. For simplicity we drop the tensor products so that

$$\hat{H}(t) = \hat{H}_S + \hat{H}_C + \hat{H}_{SC}(t) \equiv \hat{H}_0 + \hat{H}_{SC}(t) \tag{1.4.2}$$

where the last expression is only useful to collect the free Hamiltonians. The time evolution of the global system can be formally studied by keeping track of the evolution of its initial state $|\psi(0)\rangle$ under the action of the unitary operator $\hat{U} = \mathcal{T}\left\{e^{-i\int_0^t \hat{H}(t')dt'}\right\}$ [64].
For a complete description of batteries, however, it is worth to recall the density matrix formalism.
According to this formalism, a quantum system can be described by a so called density operator $\hat{\rho}$ such that:

- if the system, at a given time instant, is described by a pure state $|\psi\rangle$ its density matrix will be given by the projector onto this state

$$\hat{\rho} = |\psi\rangle\langle\psi|\,; \tag{1.4.3}$$

- if the state of the system, at a given time, consists in a statistical mixture of a set of quantum states $\{|\psi_i\rangle\}$ with probabilities $\{p_i\}$, then the it will be given by

$$\hat{\rho} = \sum_i p_i \, |\psi_i\rangle\langle\psi_i| \, . \tag{1.4.4}$$

It is straightforward to show [64] that this operator is Hermitian, positive and has unit trace. Furthermore, in the pure case it satisfies the following properties

$$\hat{\rho}^2 = \hat{\rho} \tag{1.4.5}$$

$$P = \mathrm{Tr}\{\hat{\rho}\}^2 = 1. \tag{1.4.6}$$

The quantity introduced above as P is the so called purity of the state and distinguishes pure states, namely state with $P = 1$, from mixed ones, with $P < 1$.
This formalism allows to describe the system in a more general way, taking into account also the presence of mixed states. The time evolution of the density operator is ruled by the von Neumann equation [65]

$$\frac{d\hat{\rho}(t)}{dt} = -i\Big[\hat{H}(t), \hat{\rho}(t)\Big]. \tag{1.4.7}$$

If $\hat{\rho}(t)$ is the global density matrix considering the battery and the charger altogether, the battery is described by the reduced density operator obtained by tracing out the charger degrees of freedom [43]

$$\hat{\rho}_S(t) = \mathrm{Tr}_\mathrm{C}\{\hat{\rho}(t)\}. \tag{1.4.8}$$

1.4.2 Charging process figures of merit

The charging process of a quantum battery can be characterized by different figures of merit such as stored energy, energy fluctuations and charging power [13]. Here, we only deal with those which will be relevant for our study on collisional quantum batteries.

Average stored energy Denoting the initial density matrix of the battery as $\hat{\rho}_S(0)$ and supposing a charging process ruled by the Hamiltonian in Eq. (1.4.2), the average stored energy is given by

$$E_S(t) = \mathrm{Tr}_\mathrm{S}\Big\{\hat{H}_S\hat{\rho}_S(t)\Big\} - \mathrm{Tr}_\mathrm{S}\Big\{\hat{H}_S\hat{\rho}_S(0)\Big\}. \tag{1.4.9}$$

where $\hat{\rho}_S(t)$ is the reduced density matrix of the battery at time t.

Energy fluctuations For the stability of the charging process it is important that the stored energy reaches a stationary value. If this is not the case, a great accuracy is required in controlling the charging time and in switching off the charging mechanism in order to reach the target energy value. For this reason one may be interested in studying fluctuations of various kind [13]. As an example, one can consider the so called Σ fluctuations: given the variance of the battery Hamiltonian

$$\Delta E^2(t) = \mathrm{Tr}\Big\{\hat{H}_S^2\hat{\rho}_S(t)\Big\} - \mathrm{Tr}\Big\{\hat{H}_S\hat{\rho}_S(t)\Big\}^2 \tag{1.4.10}$$

they are defined as its variation in time

$$\Sigma(t) = |\Delta E(t) - \Delta E(0)|. \tag{1.4.11}$$

Maximal energy For batteries with a finite number of discrete energy levels accessible in their operating regime the average stored energy is limited from above by the higher level of the battery spectrum E_{max} before eventually entering the continuum. This is the case of the transmon battery which will be the core of this work. Reaching a situation of complete charging, namely $E(t) = E_{max}$, can be very delicate, since it is difficult to drive the system to E_{max} without spreading in the continuum.

In our work, we are going to analyze the stored energy and purity of the achieved state. For what concerns fluctuations, we will limit to qualitative considerations. Since the charging process of the batteries we are going to analyze is collisional, we postpone considerations on the charging dynamics to Chapter 2.

1.4.3 Energy extraction

Once the battery has been charged, it is important to characterize the extractable work via unitary operations performed on it. In studying the work extraction problem we will refer to [66]: we study the evolution of the density matrix of the battery $\hat{\rho}_S$ under the action of a discharging Hamiltonian $\hat{H}(t)$. The energy variation of the system due to such a discharging process is given by

$$\Delta E = \int_{\tau_i}^{\tau_f} \frac{d}{dt}\Big(\mathrm{Tr}\Big\{\hat{\rho}_S(t)\hat{H}(t)\Big\}dt\Big). \tag{1.4.12}$$

where (τ_i, τ_f) is the time interval of the discharging process. Defining

$$W = \int_{\tau_i}^{\tau_f} \mathrm{Tr}\Big\{\hat{\rho}_S(t)\frac{d}{dt}H(t)\Big\} \tag{1.4.13}$$

$$Q = \int_{\tau_i}^{\tau_f} \mathrm{Tr}\Big\{\frac{d}{dt}\hat{\rho}_S(t)H(t)\Big\} \tag{1.4.14}$$

as respectively the work and heat of the process we obtain the relation [66]

$$\Delta E = W + Q \tag{1.4.15}$$

which corresponds to the First Law of thermodynamics [66, 67]. An interesting case is given by a discharging Hamiltonian of the form

$$\hat{H}(t) = \hat{H}_S + \hat{H}_{dis}(t) \tag{1.4.16}$$

$$\hat{H}_{dis}(t) = (\theta(t-\tau_i) - \theta(t-\tau_f))\hat{V}(t) \tag{1.4.17}$$

where $\theta(t)$ is the *Heaviside* step function. This kind of Hamiltonian, which vanishes out of the time interval (τ_i, τ_f), is usually called cyclic.
In the case of unitary evolution ruled by the Hamiltonian in Eq. (1.4.16) it is straightforward to show that $Q = 0$ [38] so that the work extracted in the process is

$$W_{ext} = -W = \mathrm{Tr}\{\hat{\rho}_S(\tau_i)H_S\} - \mathrm{Tr}\{\hat{\rho}_S(\tau_f)H_S\} = E(\tau_i) - E(\tau_f). \tag{1.4.18}$$

Here, $E(\tau_i)$ represents the energy stored before the discharging, whereas $E(\tau_f)$ stands for the amount of energy which remains trapped in the battery. For applications, it is important to study the possibility of extracting the maximum amount of energy via unitary

operations acting on the battery. Thermodynamics, in fact, states that, if a macroscopic system out of equilibrium is connected to energy extraction systems, the maximum extractable energy is determined by its energy and entropy. This bound, however, is usually not reachable for microscopic quantum systems. From this fact derives the need to study the following figure of merit.

Ergotropy It describes the maximal amount of energy extractable via unitary operations performed over the quantum battery. Starting from Eq. (1.4.18) and writing the density matrix of the system at the end of the extraction process as $\hat{\rho}_S(\tau_f) = U\hat{\rho}_S(\tau_i)U^\dagger$, ergotropy can be defined as [66]

$$\mathcal{E} = \mathrm{Tr}_S\Big\{\hat{\rho}_S(\tau_i)\hat{H}_S\Big\} - \min_{U\in SU(d)} \mathrm{Tr}_S\Big\{U\hat{\rho}_S(\tau_i)U^\dagger\hat{H}_S\Big\} \tag{1.4.19}$$

where d is the dimension of the battery Hilbert's space, and U is the unitary operation responsible for the discharging process. The last term of the above equation, namely

$$E_{f,min} \equiv \min_{U\in SU(d)} \mathrm{Tr}_S\Big\{U\hat{\rho}_S(\tau_i)U^\dagger\hat{H}_S\Big\} \tag{1.4.20}$$

represents the minimum amount of energy remaining in the battery after the discharging. Here, minimization has to be intended with respect to all possible unitary operations acting on the battery. Also, it is fundamental to observe that this is the minimum remaining energy for a given state $\hat{\rho}_S(\tau_i)$. Changing the state which undergoes the discharging will change this value.
In order to analyze ergotropy, we can introduce a particular class of states with no unitarily-extractable energy, called *passive states*. It can be shown that, given the following diagonal form of the battery Hamiltonian

$$\hat{H}_S = \sum_{j=1}^{d} E_j \left|E_j\right\rangle\!\left\langle E_j\right|, \quad \text{with} \quad E_j \leq E_{j+1} \tag{1.4.21}$$

and if the charged battery state is given by

$$\hat{\rho}_S(\tau_i) = \sum_{j=1}^{d} p_j \left|p_j\right\rangle\!\left\langle p_j\right|, \tag{1.4.22}$$

with $\{p_j\}$ denoting the eigenvalues of $\hat{\rho}_S(\tau_i)$ in non-increasing-energy order, there exists a unique passive state $\hat{\sigma}_{\rho_S}$ unitarily connected to it, which has the form

$$\hat{\sigma}_{\rho_S} = \sum_{j=1}^{d} p_j \left|E_j\right\rangle\!\left\langle E_j\right| \quad \text{with} \quad p_j \geq p_{j+1}. \tag{1.4.23}$$

This state is such that its energy corresponds to the minimum of E_f [66], namely

$$E_{f,min} = \mathrm{Tr}_S\Big\{\hat{\sigma}_{\rho_S}\hat{H}_S\Big\} = \sum_{j=1}^{d} p_j E_j. \tag{1.4.24}$$

This leads to the following expression for the ergotropy [66]

$$\begin{aligned}\mathcal{E} &= \mathrm{Tr}_S\{\hat{\rho}_S(\tau_i)H_S\} - \mathrm{Tr}_S\{\hat{\sigma}_{\rho_S}H_S\} = \\ &= \sum_{j,k}^{d} p_j E_k \Big(|\langle p_j|E_k\rangle|^2 - \delta_{j,k}\Big).\end{aligned} \tag{1.4.25}$$

This quantity is related to the purity of the battery. Indeed, supposing that the state of the battery is pure, namely, $\hat{\rho}_S(\tau_i) = |\psi\rangle\langle\psi|$, implies that it can be written in the form of Eq. (1.4.22) setting

$$p_j = \delta_{j,1} \tag{1.4.26}$$

$$|p_1\rangle = |\psi\rangle \tag{1.4.27}$$

Inserting Eq. (1.4.26) coefficients in Eq. (1.4.24) we obtain $E_{f,min} = E_1$ which is the ground state energy of the system.
Thus, a pure battery state maximizes the ergotropy since it is not possible to extract more energy in any other case.

1.5 Examples of quantum batteries models

In this section we analyze some simple examples of quantum batteries models which can be solved exactly [14]. These can be seen as the building blocks of more sophisticated models used to describe collisional and collective quantum batteries [25, 33].

1.5.1 Energy transfer between two-level systems

The first example we analyze is the case of two two-level systems: S (the battery) and C (the charger). The global Hamiltonian is of the form of Eq. (1.4.2), with

$$\hat{H}_S = \frac{\Delta}{2}\hat{\sigma}_z^{(S)} \tag{1.5.1}$$

$$\hat{H}_C = \frac{\Delta}{2}\hat{\sigma}_z^{(C)} \tag{1.5.2}$$

$$\hat{H}_{SC} \equiv g\hat{\sigma}_x^{(S)}\hat{\sigma}_x^{(C)} = g\Big(\hat{\sigma}_+^{(S)} + \hat{\sigma}_-^{(S)}\Big)\Big(\hat{\sigma}_+^{(C)} + \hat{\sigma}_-^{(C)}\Big) \tag{1.5.3}$$

where the respective $\hat{\sigma}_\pm$ operators are defined as

$$\hat{\sigma}_\pm = \frac{1}{2}(\hat{\sigma}_x \pm \hat{\sigma}_y) \quad \rightarrow \quad \sigma_\pm = |\pm\rangle\langle\mp|\,. \tag{1.5.4}$$

The last expression is written in terms of the $\hat{\sigma}_z$ eigenstates. Since we are focusing on energy transfers between the charger and the battery for an initial state of the form

$$|\psi(0)\rangle = |-\rangle_S\,|+\rangle_C \equiv |-,+\rangle \tag{1.5.5}$$

we can neglect the action of terms of the form $\hat{\sigma}_-^{(C)}\hat{\sigma}_-^{(S)}$ and $\hat{\sigma}_+^{(C)}\hat{\sigma}_+^{(S)}$. The evolved state is thus given by [14]

$$|\psi(t)\rangle = e^{-i\Delta t}(\mathrm{Cos}(gt)\,|-,+\rangle - i\mathrm{Sin}(gt)\,|-,+\rangle) \tag{1.5.6}$$

so that evaluating the stored energy as defined in Eq. (1.4.9) leads to

$$E_S(t) = \Delta \mathrm{Sin}^2(gt). \tag{1.5.7}$$

This implies that the maximum amount of energy transferable from the charger to the battery is $E_{max} = \Delta$ which can be obtained after a time

$$\tau = \frac{\pi}{2g}. \tag{1.5.8}$$

At this time, the evolved state of the battery is pure, and the ergotropy is maximized, equaling the stored energy.

1.5.2 Two-level systems charged by a harmonic oscillator

The Hamiltonian we consider here is composed by the following three terms

$$\hat{H}_S = \frac{\Delta}{2}\hat{\sigma}_z \tag{1.5.9}$$

$$\hat{H}_C = \omega_C \hat{a}^\dagger \hat{a} \tag{1.5.10}$$

$$\hat{H}_{SC} \equiv g\Big(\hat{a}^\dagger + \hat{a}\Big)\hat{\sigma}_x = g\Big(\hat{a}^\dagger + \hat{a}\Big)(\hat{\sigma}_+ + \hat{\sigma}_-) \tag{1.5.11}$$

As already discussed in Sec. 1.3.2, the term in Eq. (1.5.10) describes a quantum resonant circuit, whereas Eq. (1.5.9) is the Hamiltonian of a two-level system, which can be implemented as discussed in Sec. 1.3.3. The coupling Hamiltonian in Eq. (1.5.11) can be practically realized by a capacitive coupling of a superconducting qubit with a resonant LC oscillator [44].

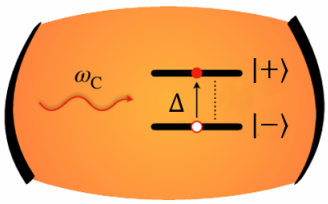

Figure 1.14: Schematic representation of a TLS battery where a single TLS with energy separation Δ is coupled to a single-mode photonic cavity of frequency ω_C. Image taken from [68]

A conventional approach to solve this Hamiltonian in the resonant case $\Delta \approx \omega_C$ and for $g \ll \omega_C$ consists in performing the *rotating wave approximation* (RWA) [46] which allows to neglect the counter rotating terms $\hat{a}^\dagger\hat{\sigma}_+$ and $\hat{a}\hat{\sigma}_-$ leading to

$$\hat{H}_{JC} = \frac{\Delta}{2}\hat{\sigma}_z + \omega_C \hat{a}^\dagger \hat{a} + g\Big(\hat{a}^\dagger\hat{\sigma}_- + \hat{a}\hat{\sigma}_+\Big) \tag{1.5.12}$$

usually referred to as the *Jaynes-Cummings* (JC) Hamiltonian [46].
It provides an accurate description of the complete system provided that $g \lesssim 0.1\omega_C$ holds. It is worth observing that

$$\left[\hat{H}_0, \hat{H}_{SC}\right] = g\left(\hat{a}^\dagger\hat{\sigma}_- + \hat{a}\hat{\sigma}_+\right)(\omega_C - \Delta) \tag{1.5.13}$$

where $\hat{H}_0 = \hat{H}_S + \hat{H}_C$. This implies that if the resonance condition $\Delta = \omega_C$ holds, the number of excitations of the system $S+C$ is conserved during the interaction [14, 46]. This is the ultimate reason for the simplification of the problem. Projecting the Hamiltonian on the orthonormal basis tensor product between the Fock basis of the oscillator and the spin basis of the qubit, namely the set $\{|m, \pm\rangle\}$ with $m \in \mathbb{N}$, this symmetry allows us to focus only on a two dimensional subspace, chosen as $\{|m-1, +\rangle, |m, -\rangle\}$. We obtain then

$$\hat{H}_{JC} = \begin{pmatrix} \left(m - \frac{1}{2}\right)\Delta & g\sqrt{m} \\ g\sqrt{m} & \left(m - \frac{1}{2}\right)\Delta \end{pmatrix}. \tag{1.5.14}$$

We begin by studying the following initial condition

$$|\psi(0)\rangle = |m, -\rangle \tag{1.5.15}$$

that is, the battery is empty and the charger is prepared in a Fock state $|m\rangle$.
In order to do so, we need to compute the evolved state $|\psi(t)\rangle = e^{-i\hat{H}_{JC}t}|\psi(0)\rangle$. We must perform the diagonalization of Eq. (1.5.7) leading to its eigenvalues

$$E_{1,2} = \Delta\left(m - \frac{1}{2}\right) \pm g\sqrt{m} \tag{1.5.16}$$

and eigenvectors

$$|\psi_{1,2}\rangle = \frac{1}{\sqrt{2}}(|m-1, +\rangle \pm |m, -\rangle). \tag{1.5.17}$$

Decomposing $|\psi(0)\rangle$ in terms of such eigenvectors we obtain the following expression for the evolved global state [14]

$$|\psi(t)\rangle = \mathrm{Cos}(g\sqrt{m}t)\,|m, -\rangle - i\mathrm{Sin}(g\sqrt{m}t)\,|m-1, -\rangle \tag{1.5.18}$$

with corresponding density matrix

$$\hat{\rho} = \begin{pmatrix} \mathrm{Sin}^2(g\sqrt{m}t) & -\frac{i}{2}\mathrm{Sin}(2g\sqrt{m}t) \\ \frac{i}{2}\mathrm{Sin}(2g\sqrt{m}t) & \mathrm{Cos}^2(g\sqrt{m}t) \end{pmatrix}. \tag{1.5.19}$$

This leads to the following expression for the energy stored in the battery

$$E_S(t) = \Delta\mathrm{Sin}^2\left(g\sqrt{m}t\right) \tag{1.5.20}$$

which enables us to compute the stored energy when the charger is initialized in a Fock state $|m\rangle$. In this case, it can be noticed that the maximum amount of energy stored in the system E_{max} corresponds to a energy quantum Δ and is reached at

$$\tau = \frac{\pi}{2g\sqrt{m}}. \tag{1.5.21}$$

Comparing this with the previous charging via TLS, the same amount of maximal energy can be stored, but now in a time window reduced by a factor $\frac{1}{\sqrt{m}}$. Thus, from the initial m excitations, only one can be transferred, whereas the others act as catalyzers of the process [14].
Let us suppose now that the charger is initialized in an arbitrary state $\hat{\rho}_C(0)$ with an initial energy $E_C(0) = K\Delta$. Then, the above procedure can be generalized by decomposing its density matrix in the Fock basis. The generalization of Eq. (1.5.20) yields [14]

$$E_S(t) = \Delta \sum_m p_m^{(K)} \mathrm{Sin}^2\left(g\sqrt{m}t\right) \tag{1.5.22}$$

where $p_m^{(K)}$ are $\hat{\rho}_C(0)$ diagonal elements subject to

$$\sum_m m p_m^{(K)} = K. \tag{1.5.23}$$

Eq. (1.5.22) clearly shows that $E_{max} \leq \Delta$ for arbitrary inputs, with Fock states providing optimal performances.

1.5.3 Charging a harmonic oscillator via TLS: towards the Micromaser

It is also possible to invert the preceding model, considering the charging of a harmonic oscillator, initialized in $|\psi(0)\rangle = |m-1, +\rangle$, employing a two-level system, considered again in the resonant limit $\omega_C = \Delta$. The Hamiltonian describing the full process is the same of Eq. (1.5.5). By performing the same analysis we obtain the following expression of the evolved density matrix of the global system in the $\{|m-1,+\rangle, |m,-\rangle\}$ subspace

$$\hat{\rho} = \begin{pmatrix} \mathrm{Cos}^2(g\sqrt{m}t) & -\frac{i}{2}\mathrm{Sin}(2g\sqrt{m}t) \\ \frac{i}{2}\mathrm{Sin}(2g\sqrt{m}t) & \mathrm{Sin}^2(g\sqrt{m}t) \end{pmatrix} \tag{1.5.24}$$

A direct computation of the stored energy as defined in Eq. (1.4.9) leads to the same expression obtained in Eq. (1.5.13). As well as that case, the maximum amount of stored energy is a single excitation Δ. However, given the oscillator multi-level structure it would be of great interest to realize charging setups able to store a greater amount of energy. A possibility is given by the repeated interactions schemes, where a single battery (e.g. the oscillator) is charged via multiple chargers (e.g. qubits). The theoretical background for this approach will be discussed in the next Chapter, while a quantum battery charged in this way, namely the Micromaser quantum battery, will be analyzed in Chapter 3.

Chapter 2

Open quantum systems

Quantum batteries constitute an example of open quantum systems, namely of quantum-mechanical systems exchanging energy with their surroundings. In order to properly characterize them, it is therefore of primary importance to become familiar with the study of the reduced dynamics of systems coupled with an external environment, that is, the dynamics of the reduced density matrix obtained by tracing out environmental degrees of freedom from the density matrix of the whole system. The external environment can be either a *charger* providing energy to the battery or a dissipative environment, which can also cause a class of phenomena usually referred to as *Decoherence* [67].

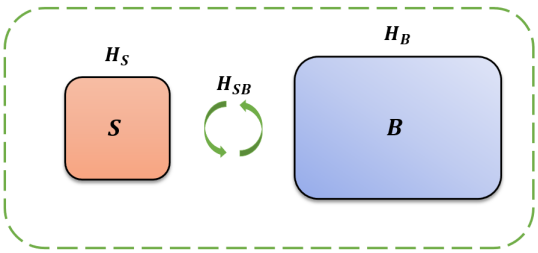

Figure 2.1: Schematic representation of the open quantum system dynamics. The system S is coupled with an external environment B which, in general, represents everything which can be coupled with the system. As will be clarified later, H_S, H_B and H_{SB} respectively represent the system, bath and interaction Hamiltonians.

In order to study the dynamics of an open quantum system it is possible to use different approaches. The most conventional one consists in deriving time evolution equations for the reduced density matrix, usually referred to as Master Equations [10, 67], which can be written in different forms depending on the assumptions made in their derivation. In recent years, however, significant relevance was gained in literature by the so called *Collision Models* [34]. Here, the bath is described as a collection of simple quantum constituents called *ancillae* (usually two-level systems or quantum harmonic oscillators) which interact individually and sequentially with the system. Therefore, the system interacts at first with the first *ancilla*, then with the second one and so on. A great variety of collision models has been proposed: they can be non Markovian or Markovian (whether memory effects between two subsequent interactions are considered or not) [34], homogeneous (if

all *ancillae* are considered to be equal) or inhomogeneous (if they are all different) [34]. In this chapter we will compare these two methods focusing on Markovian processes. First of all, following the approach of [67], we will introduce the concept of *quantum dynamical semigroup* for the description of the dynamics of Markovian processes, obtaining the most general form of its generator. Then we will derive the most general Markovian master equation by means of a microscopic derivation. In the end, in Sec. (2.2) we will change perspective, analyzing quantum collision models, discussing their general features and studying the paradigmatic example of the Micromaser [32, 34]. Before ending the Chapter, we will show that collision models give rise to a discrete Lindblad master equation if we consider the limit of short collision times.

2.1 Master equations for Markovian processes

In general, given a quantum mechanical system described by its density matrix $\hat{\rho}(t)$ and its generally time dependent Hamiltonian $\hat{H}(t)$, its time evolution is described by the *Liouville-Von Neumann* equation [65]

$$\frac{d\hat{\rho}(t)}{dt} = -i\big[\hat{H}(t), \hat{\rho}(t)\big]. \tag{2.1.1}$$

If we denote the density matrix at an initial time t_o as $\hat{\rho}(t_o)$, the evolved density matrix of the system can be written in terms of a unitary evolution operator as

$$\hat{\rho}(t) = \hat{U}(t, t_o)\hat{\rho}(t_o)\hat{U}^\dagger(t, t_o) \tag{2.1.2}$$

with

$$\hat{U}(t, t_o) = \hat{\mathcal{T}}\big\{e^{-i\int_{t_o}^{t}\hat{H}(t')dt'}\big\}. \tag{2.1.3}$$

The operator $\hat{\mathcal{T}}$ introduced above is the so called time ordering operator, which orders products of time-dependent operators such that their time-arguments increase from right to left [65].
This description is carried out in the Schrödinger picture for the quantum time evolution of a system, in which the time dependence is encoded in quantum states. Since we will often apply the methods studied in this chapter to systems whose Hamiltonians can be written as the sum of a time independent Hamiltonian $\hat{H}_0$ and an explicitly time dependent part $\hat{H}_1(t)$, namely

$$\hat{H}(t) = \hat{H}_0 + \hat{H}_1(t) \tag{2.1.4}$$

it is convenient for us to move to the interaction picture. Density matrices and operators in this picture at a given time t can be obtained starting from their Schrödinger counterparts as follows

$$\tilde{\rho}(t) = \tilde{U}(t, t_0)\hat{\rho}(t_0)\tilde{U}^\dagger(t, t_0) \tag{2.1.5}$$

$$\tilde{A}(t) = \hat{U}_0^\dagger(t, t_0)\hat{A}(t)\hat{U}_0(t, t_0) \tag{2.1.6}$$

where U_0 represents the free Hamiltonian evolution operator

$$\hat{U}_0(t, t_0) = e^{-i\hat{H}_0(t-t_0)} \tag{2.1.7}$$

and $\tilde{U}$ is given by [65]

$$\tilde{U}(t, t_0) = \hat{U}_0^\dagger(t, t_0)\hat{U}(t, t_0). \tag{2.1.8}$$

From now on we will use $\tilde{A}$ to denote the interaction picture form of a generic operator $\hat{A}$, dropping the " $\hat{}$ " in order to simplify notations.
It is straightforward to show [65] that $\tilde{U}$ is linked to $\tilde{H}_1(t)$ through the following relation

$$\frac{\partial \tilde{U}(t,t_0)}{\partial t} = -i\tilde{H}_1(t)\tilde{U}(t,t_0) \tag{2.1.9}$$

which leads to the interaction picture $Liouville - Von\ Neumann$ equation

$$\frac{d\tilde{\rho}(t)}{dt} = -i\big[\tilde{H}_1(t), \tilde{\rho}(t)\big]. \tag{2.1.10}$$

This equation represents the starting point of the derivations we are going to perform in the following.
In fact, as anticipated, we are going to study the time evolution of the density matrix of a system S coupled with an external environment B. Therefore, the global Hamiltonian will be the sum of the free Hamiltonians of the system and of the bath, $\hat{H}_S$ and $\hat{H}_B$ respectively, together with a time-dependent coupling $\hat{H}_{SB}(t)$, leading to

$$\hat{H}(t) = \hat{H}_S + \hat{H}_B + \hat{H}_{SB}(t). \tag{2.1.11}$$

In this case $\hat{\rho}(t)$ represents the density matrix of the composite system. Since the global Hamiltonian in Eq. (2.1.11) is of the same form of that in Eq. (2.1.4) provided that we identify $\hat{H}_S + \hat{H}_B$ as $\hat{H}_0$ and $\hat{H}_{SB}(t)$ as $\hat{H}_1(t)$, the dynamics of the global system in the interaction picture can be described by inserting the time dependent coupling $\hat{H}_{SB}(t)$ in Eq. (2.1.10). Since the reduced density matrix of the system S can be obtained by tracing over bath degrees of freedom, its dynamics is ruled by [67]

$$\frac{d\tilde{\rho}_S(t)}{dt} = -i\mathrm{Tr_B}\big\{\big[\tilde{H}_{SB}(t), \tilde{\rho}(t)\big]\big\}. \tag{2.1.12}$$

Solving this equation in a completely general and exact way reveals to be impossible [67]. To proceed further we need to make some simplifier assumptions, which will be discussed in the following sections.

2.1.1 Quantum dynamical semigroup and Lindblad master equations

Following the approach developed in [67], we will at first consider the assumption of short bath correlation times in order to formulate the reduced dynamics of the system by means of the so called *quantum dynamical semigroup* and to obtain the most general form of a Markovian Master Equation, known as Lindblad Master Equation. For the sake of simplicity we will limit our treatment to cases where the Hamiltonian of the system is time independent. We start our discussion by specifying the initial condition for the global system, supposing the initial state at $t = 0$ to be separated as

$$\hat{\rho}(0) = \hat{\rho}_S(0) \otimes \hat{\rho}_B \tag{2.1.13}$$

where $\hat{\rho}_B$ represents a reference environmental state. It is usually assumed as a thermal state at fixed temperature

$$\hat{\rho}_B = \frac{e^{-\beta\hat{H}_B}}{Z} \tag{2.1.14}$$

$$Z = \mathrm{Tr}_B\big\{e^{-\beta\hat{H}_B}\big\}. \tag{2.1.15}$$

All along this section we will work in Schrödinger picture. We can then write the evolved density matrix $\hat{\rho}_S(t)$ by means of a dynamical map $M(t)$ acting on density matrices at a given time, and such that

$$\hat{\rho}_S(t) = \mathrm{Tr}_\mathrm{B}\big\{\hat{U}(t,0)\hat{\rho}_S(0)\otimes\hat{\rho}_B\hat{U}^\dagger(t,0)\big\} \equiv M(t)\hat{\rho}_S(0). \tag{2.1.16}$$

The dynamical maps $\big\{M(t) : t \geq 0\big\}$ constitute a set of superoperators, namely operators acting on the space of quantum operators acting on the quantum system considered, which is also known as *Lioville* space. We will drop the "ˆ" from the superoperators to distinguish them from operators acting on quantum states. Dynamical maps describe therefore the time evolution of the system and they can be characterized by spectrally decomposing the environment density matrix as

$$\hat{\rho}_B = \sum_\alpha \lambda_\alpha \left|\alpha\right\rangle\!\left\langle\alpha\right| \tag{2.1.17}$$

which, together with Eq. (2.1.16), leads to the following decomposition

$$M(t)\hat{\rho}_S(0) = \sum_{\alpha,\beta} W_{\alpha\beta}(t)\hat{\rho}_S(0)W^\dagger_{\alpha\beta}(t) \tag{2.1.18}$$

$$W_{\alpha\beta}(t) = \sqrt{\lambda_\alpha}\left\langle\alpha|\hat{U}(t,0)|\beta\right\rangle. \tag{2.1.19}$$

The new operators $W_{\alpha\beta}(t)$ act on the open system Hilbert space and satisfy the following relation

$$\sum_{\alpha,\beta} W^\dagger_{\alpha\beta}(t)W_{\alpha\beta}(t) = \hat{\mathbb{I}}_S \tag{2.1.20}$$

which in turn causes $M(t)$ to be completely positive and trace preserving [67], features of utmost importance in order to describe physical processes.
Until now, we only re-elaborated the problem without making any progress. What we will do in this section is to suppose that the set of dynamical maps introduced above satisfies the following *semigroup property*

$$M(t_1)M(t_2) = M(t_1+t_2), \forall t \geq 0. \tag{2.1.21}$$

This assumption can be made provided that the characteristic time scale of the free evolution of the system S is much greater than the decay time of bath correlation functions. In this way, memory effects can be neglected and one expects the dynamics to be Markovian [67]. Therefore, the semigroup property introduced above represents a way to formalize the Markovianity of the dynamics. As anticipated, we will further discuss the physical conditions for Markovianity in Sec. 2.1.2. For the moment, however, our focus will be devoted to studying the effects of Eq. (2.1.21).
A set of superoperators $\big\{M(t) : t \geq 0\big\}$ satisfying Eq. (2.1.21) will be referred to as *quantum dynamical semigroup*. It is possible to show that there exists a superoperator L usually referred to as semigroup generator, such that the action of the dynamical map at any given time t can be written as

$$M(t) = e^{Lt} \tag{2.1.22}$$

which, upon derivation with respect of time, leads to the so called Markovian quantum master equation

$$\frac{d\hat{\rho}_S(t)}{dt} = L\hat{\rho}_S(t). \tag{2.1.23}$$

In this expression, which represents the generalization of the *Liouville- Von Neumann* equation to the case of open quantum systems, every detail on the dynamics of the system is hidden in the superoperator L. It is worth noting that this superoperator has no explicit time dependence thanks to the assumption of time independent Hamiltonian. The generalization of our treatment to the time dependent case can be found in [67]. As we will see in Section (2.1.2) its most general form can be derived starting from the knowledge of the coupling Hamiltonian $\hat{H}_{SB}$. Before doing this, however, we briefly discuss how to derive the general form of the generator starting from its definition in Eq. (2.1.22).
To simplify the discussion we only focus on the case of finite Hilbert space dimension for the system S, namely $dim\mathscr{H}_S = N$. In this case, the *Liouville* space of $W_{\alpha\beta}(t)$ operators is a complex space with dimension N^2. We can then choose a basis of operators for this space, which we denote as F_i with $i \in \{1, ..., N^2\}$, such that they are orthonormal with respect to the following scalar product

$$(F_i, F_j) := \mathrm{Tr}_S\{F_i^\dagger F_j\} = \delta_{ij}. \tag{2.1.24}$$

One of this basis operators is usually chosen to be proportional to the identity, namely $F_{N^2} = I_S/N^{\frac{1}{2}}$ so that the other basis operators are traceless.
Decomposing each $W_{\alpha\beta}$ operator over this basis and inserting these decompositions in Eq. (2.1.18) one gets to the following expression for the action of $M(t)$ on the system density matrix

$$M(t)\hat{\rho}_S(t) = \sum_{i,j=1}^{N^2} c_{ij}(t) F_i \hat{\rho}_S(t) F_j^\dagger \tag{2.1.25}$$

where the coefficients c_{ij} form an Hermitian and positive matrix [67] and are given by

$$c_{ij}(t) = \sum_{\alpha,\beta} (F_i, W_{\alpha\beta}(t))(F_j, W_{\alpha\beta}(t))^*. \tag{2.1.26}$$

We can now rewrite Eq. (2.1.23) as

$$\begin{aligned} L\hat{\rho}_S(t) &= \lim_{\epsilon\to 0} \frac{M(\epsilon)\hat{\rho}_S(t) - \hat{\rho}_S(t)}{\epsilon} = \\ &= \lim_{\epsilon\to 0}\Bigg\{ \frac{1}{\sqrt{N}} \sum_{i=1}^{N^2-1} \left(\frac{c_{iN^2}(\epsilon)}{\epsilon} F_i \hat{\rho}_S(t) + \frac{c_{N^2 i}(\epsilon)}{\epsilon} \hat{\rho}_S(t) F_i^\dagger \right) \\ &\quad + \frac{1}{N} \frac{c_{N^2N^2}(\epsilon) - N}{\epsilon} \hat{\rho}_S(t) + \sum_{i,j=1}^{N^2-1} \frac{c_{ij}(\epsilon)}{\epsilon} F_i \hat{\rho}_S(t) F_j^\dagger \Bigg\}. \end{aligned} \tag{2.1.27}$$

Defining

$$a_{N^2N^2} = \lim_{\epsilon\to 0} \frac{c_{N^2N^2}(\epsilon) - N}{\epsilon} \tag{2.1.28}$$

$$a_{iN^2} = \lim_{\epsilon\to 0} \frac{c_{iN^2}(\epsilon)}{\epsilon}, i = 1, ..., N^2 - 1 \tag{2.1.29}$$

$$a_{ij} = \lim_{\epsilon\to 0} \frac{c_{ij}(\epsilon)}{\epsilon}, i, j = 1, ..., N^2 - 1 \tag{2.1.30}$$

which form an Hermitian and positive matrix and applying these definitions to Eq. (2.1.27) it is possible to show [67] that the action of the generator can be rewritten as

$$L\hat{\rho}_S(t) = -i[K, \hat{\rho}_S(t)] + \{G, \hat{\rho}_S(t)\} + \sum_{i,j=1}^{N^2-1} a_{ij} F_i \hat{\rho}_S(t) F_j^\dagger. \tag{2.1.31}$$

Here, K is an Hermitian operator given by [67]

$$K = \frac{1}{2i}(F^\dagger - F) \tag{2.1.32}$$

$$F = \frac{1}{\sqrt{N}} \sum_{i=1}^{N^2-1} a_{iN^2} F_i. \tag{2.1.33}$$

whereas G is given by

$$G = \frac{a_{N^2N^2}}{2N} I_S + \frac{1}{2}\big(F^\dagger + F\big). \tag{2.1.34}$$

This definition of G turns out to be equivalent to

$$G = -\frac{1}{2} \sum_{i,j=1}^{N^2-1} a_{ij} F_j^\dagger F_i \tag{2.1.35}$$

thanks to the trace preserving property of the dynamical semigroup [67], leading to

$$L\hat{\rho}_S(t) = -i[K, \hat{\rho}_S(t)] + \sum_{i,j=1}^{N^2-1} a_{ij} \Big\{ F_i \hat{\rho}_S(t) F_j^\dagger - \frac{1}{2}\Big\{ F_j^\dagger F_i, \hat{\rho}_S(t) \Big\} \Big\}. \tag{2.1.36}$$

The matrix a can be diagonalized by means of a unitary transformation u as

$$uau^\dagger = \begin{pmatrix} \gamma_1 & 0 & \cdots & 0 \\ 0 & \gamma_2 & \cdots & 0 \\ \vdots & \vdots & \ddots & \vdots \\ 0 & 0 & \cdots & \gamma_{N^2-1} \end{pmatrix}. \tag{2.1.37}$$

This unitary operator defines the following change of basis in the Liouville space

$$F_i = \sum_{j=1}^{N^2-1} u_{ij} A_j \tag{2.1.38}$$

which enables us to rewrite Eq. (2.1.36) as

$$L\hat{\rho}_S(t) = -i[K, \hat{\rho}_S(t)] + \sum_{j=1}^{N^2-1} \gamma_j \Big\{ A_j \hat{\rho}_S(t) A_j^\dagger - \frac{1}{2}\Big\{ A_j^\dagger A_j, \hat{\rho}_S(t) \Big\} \Big\} \tag{2.1.39}$$

which is the most general generator we were looking for. We will show in the following the connection between non negative quantities $\{\gamma_j\}$ and environmental correlation functions. The operators $\{A_j\}$ are usually referred to as Lindblad operators and Eq. (2.1.39) is usually called the Lindblad Master Equation [69, 67].
The mathematical proof of the fact that Eq. (2.1.39) represents the most general generator of a *quantum dynamical semigroup* was first given by Gorini, Kossakowski and Sudarshan [70] for finite-dimensional Hilbert spaces and then extended by Lindblad [69] to cases where the index j runs over a countable yet unbounded set.

2.1.2 Microscopic derivation

As anticipated, in this section we derive the most general form of the *dynamical semigroup* generator by directly studying the time evolution of the global system described by $\hat{\rho}$ given its full Hamiltonian

$$\hat{H}(t) = \hat{H}_S + \hat{H}_B + \hat{H}_{SB}(t). \tag{2.1.40}$$

Since this derivation is easily performed in the interaction picture, our starting point is Eq. (2.1.10), which can be applied to our problem by substituting $\tilde{H}_1(t)$ with $\tilde{H}_{SB}(t)$. Upon integration in time, this leads to

$$\tilde{\rho}(t) = \tilde{\rho}(0) - i\int_0^t dt' \Big[\tilde{H}_{SB}(t'), \tilde{\rho}(t')\Big]. \tag{2.1.41}$$

Inserting it back into Eq. (2.1.12) one gets to

$$\frac{d\tilde{\rho}_S(t)}{dt} = -i\mathrm{Tr_B}\Big\{\Big[\tilde{H}_{SB}(t), \rho(0)\Big]\Big\} - \int_0^t dt' \mathrm{Tr_B}\Big\{\Big[\tilde{H}_{SB}(t), \Big[\tilde{H}_{SB}(t'), \tilde{\rho}(t')\Big]\Big]\Big\}. \tag{2.1.42}$$

It is worth observing that it is always possible to re-define $\tilde{H}_{SB}$ in such a way that the first term in right-hand side of Eq. (2.1.42) is zero, and this is the case we will consider henceforth [67].
Note that the equation obtained still contains the global density matrix $\hat{\rho}$. In order to eliminate it from the integral, we will have to perform some approximations, starting from the so called *Born approximation* [67], which assumes a weak system-bath coupling in order to neglect the effects of the system dynamics on the external bath. This allows us to consider a global density matrix at a given time t of the form

$$\hat{\rho}(t) \approx \hat{\rho}_S(t) \otimes \hat{\rho}_B, \forall t. \tag{2.1.43}$$

We underline the fact that this condition still allows to consider the effects of environmental excitations. Inserting it back into Eq. (2.1.42) we are led to

$$\frac{d\tilde{\rho}_S}{dt} = -\int_0^t dt' \,\mathrm{Tr}_B\Big\{\Big[\tilde{H}_{SB}(t), \Big[\tilde{H}_{SB}(t'), \tilde{\rho}_S(t') \otimes \tilde{\rho}_B\Big]\Big]\Big\}. \tag{2.1.44}$$

It is easy to observe that this equation is not yet local in time.
To proceed further, we suppose the coupling Hamiltonian to be time independent and write its Schrödinger's picture form in terms of a basis of operators $\{\hat{\sigma}_i\}$ acting on the system which couple to a set of environment operators $\{\hat{B}_i\}$ in the following way

$$\hat{H}_{SB} = \sum_{i=1}^{N^2-1} \hat{\sigma}_i \otimes \hat{B}_i \tag{2.1.45}$$

where again we denote with N the dimension of the system Hilbert's space. Inserting this in Eq. (2.1.44) we obtain

$$\frac{d\tilde{\rho}_S}{dt} = -\int_0^t dt' \sum_{i,j} \mathrm{Tr}_B\Big\{\Big[\tilde{\sigma}_i(t) \otimes \tilde{B}_i(t), \Big[\tilde{\sigma}_j(t') \otimes \tilde{B}_j(t'), \tilde{\rho}_S(t') \otimes \tilde{\rho}_B\Big]\Big]\Big\}. \tag{2.1.46}$$

We then introduce the bath correlation functions as

$$C_{ij}(t,t') = \mathrm{Tr}_B\{\tilde{B}_i^\dagger(t)\tilde{B}_j(t')\tilde{\rho}_B\} \tag{2.1.47}$$

and assume the environment state $\hat{\rho}_B$ to be stationary, that is $\left[\hat{\rho}_B, \hat{H}_B\right] = 0$. This guarantees the homogeneity of environmental correlation functions

$$C_{ij}(t,t') = C_{ij}(t-t') \tag{2.1.48}$$

and allows us to rewrite Eq. (2.1.46) as

$$\begin{aligned}\frac{d\tilde{\rho}_S}{dt} = -\int_0^t dt' \sum_{i,j}\Big[&C_{ij}(t-t')\{\tilde{\sigma}_i(t)\tilde{\sigma}_j(t')\tilde{\rho}_S(t') - \tilde{\sigma}_j(t')\tilde{\rho}_S(t')\tilde{\sigma}_i(t)\} \\ &+C_{ji}(t'-t)\{\tilde{\rho}_S(t')\tilde{\sigma}_i(t')\tilde{\sigma}_j(t) - \tilde{\sigma}_j(t)\tilde{\rho}_S(t')\tilde{\sigma}_i(t')\}\Big].\end{aligned} \tag{2.1.49}$$

In order to obtain a master equation which is both local in time and Markovian, we need to perform the second approximation, known as *Markov's approximation* which we can split into two steps. Firstly, one needs to substitute $\tilde{\rho}_S(t')$ with $\tilde{\rho}_S(t)$. This is accurate provided that environmental correlation functions $C_{kl}(t-t')$ are peaked around $\tau = t - t' = 0$ and the width τ_B of their peaks is much shorter than the typical time scale of the open system. The second part of *Markov's approximation* consists in extending the integral up to infinity, which is consistent with the assumption made above. Since, due to these assumptions, time scales smaller than τ_B are not resolved, the resultant dynamics is coarse grained in time.
To sum up this first part of the derivation we observe that *Born* and *Markov's* approximations led us to the following Markovian Master Equation

$$\frac{d\tilde{\rho}_S}{dt} = -\int_0^{+\infty} d\tau \sum_{i,j}\big[C_{ij}(\tau)\{\tilde{\sigma}_i(t)\tilde{\sigma}_j(t-\tau)\tilde{\rho}_S(t) - \tilde{\sigma}_j(t-\tau)\tilde{\rho}_S(t)\tilde{\sigma}_i(t)\} + h.c.\big] \tag{2.1.50}$$

but are not sufficient to obtain the most general form of the generator L which we have derived at the end of Section (2.1.1). In order to re-obtain a similar expression we need to perform the so called *secular approximation*. Before doing so, we go through few calculations to simplify the interaction picture expressions of $\{\hat{\sigma}_i\}$ operators, writing them in terms of $\hat{H}_S$ eigenoperators. To simplify our discussion, we assume a discrete spectrum $\{\epsilon\}$. Denoting as $\{\hat{\Pi}(\epsilon)\}$ the set of projectors onto the corresponding eigenspaces, we can define the following operators

$$\hat{\sigma}_i(\omega) = \sum_{\epsilon-\epsilon'=\omega} \hat{\Pi}(\epsilon')\hat{\sigma}_i\hat{\Pi}(\epsilon) \tag{2.1.51}$$

which satisfy the properties [67]

$$\left[\hat{H}_S, \hat{\sigma}_i(w)\right] = -\omega\hat{\sigma}_i(\omega) \tag{2.1.52}$$

$$\left[\hat{H}_S, \hat{\sigma}_i^\dagger(w)\right] = \omega\hat{\sigma}_i^\dagger(\omega) \tag{2.1.53}$$

$$\hat{\sigma}_i^\dagger(\omega) = \hat{\sigma}_i(-\omega) \tag{2.1.54}$$

$$\sum_\omega \hat{\sigma}_i(\omega) = \sum_\omega \hat{\sigma}_i^\dagger(\omega) = \hat{\sigma}_i. \tag{2.1.55}$$

The last equation allows us to write the interaction Hamiltonian as

$$\hat{H}_{SB} = \sum_{i,\omega} \hat{\sigma}_i(\omega) \otimes \hat{B}_i = \sum_{i,\omega} \hat{\sigma}_i^\dagger(w) \otimes \hat{B}_i^\dagger. \tag{2.1.56}$$

whereas Eqs. (2.1.52)-(2.1.54) allows us to write the $\hat{\sigma}_i$ operators in interaction picture as [67]

$$\tilde{\sigma}_i(t) = \sum_{\omega} e^{-i\omega t} \hat{\sigma}_i(\omega) = \sum_{\omega} e^{i\omega t} \hat{\sigma}_i^\dagger(\omega). \tag{2.1.57}$$

We can use these relations to rewrite the terms appearing in the right-hand side of Eq. (2.1.50) as follows

$$\tilde{\sigma}_j(t-\tau) = \sum_{\omega} e^{-i\omega(t-\tau)} \hat{\sigma}_j(\omega) \tag{2.1.58}$$

$$\tilde{\sigma}_i(t) = \sum_{\omega'} e^{i\omega' t} \hat{\sigma}_i^\dagger(\omega') \tag{2.1.59}$$

which leads to

$$\frac{d\tilde{\rho}_S(t)}{dt} = \sum_{i,j,\omega\omega'} e^{i(\omega'-\omega)t} \Gamma_{ij}(\omega) \big[\hat{\sigma}_j(\omega)\tilde{\rho}_S(t)\hat{\sigma}_i^\dagger(\omega') - \hat{\sigma}_i^\dagger(\omega')\hat{\sigma}_j(\omega)\tilde{\rho}_S(t)\big] + h.c. \tag{2.1.60}$$

provided that we define the Fourier transform

$$\Gamma_{ij}(\omega) \equiv \int_0^{+\infty} d\tau e^{i\omega\tau} C_{ij}(\tau) \tag{2.1.61}$$

of the two point environmental correlation function.
Both Eq. (2.1.50) and Eq. (2.1.60) clarify the fact that environmental correlation functions play a significant role in the study of the dynamics of the open system and the latter equation will help us to state the *secular approximation* in a clear way. In order to do so, let us consider the characteristic time scale τ_S of the free evolution of the system S. This can be estimated as the inverse of the typical value of the frequency difference between two distinct and non degenerate states of the system, namely

$$\tau_S \approx \frac{1}{|\omega - \omega'|}. \tag{2.1.62}$$

If τ_S is much greater than the relaxation time of the open system τ_R, we can neglect non secular terms in Eq. (2.1.60), i.e. terms with $\omega \neq \omega'$, given the fact that their oscillations are much faster than the appreciable variations of ρ_S. This leaves us with the following equation

$$\frac{d\tilde{\rho}_S(t)}{dt} = \sum_{i,j,\omega} \big\{\Gamma_{ij}(\omega)\big(\hat{\sigma}_j(\omega)\tilde{\rho}_S(t)\hat{\sigma}_i^\dagger(\omega) - \hat{\sigma}_i^\dagger(\omega)\hat{\sigma}_j(\omega)\tilde{\rho}_S(t)\big) + h.c.\big\}. \tag{2.1.63}$$

Few more algebraic steps must be performed in order to recover the most general form of the dynamical semigroup generator. We begin by the following decomposition of the Fourier transforms $\Gamma_{ij}(\omega)$

$$\Gamma_{ij}(\omega) = \frac{1}{2} a_{ij}(\omega) + i\Sigma_{ij}(\omega) \tag{2.1.64}$$

where

$$\Sigma_{ij}(\omega) = \frac{1}{2i}(\Gamma_{ij}(\omega) - \Gamma^*_{ij}(\omega)) \tag{2.1.65}$$

$$a_{ij}(\omega) = \Gamma_{ij}(\omega) + \Gamma^*_{ij}(\omega) = \int_{-\infty}^{+\infty} e^{i\omega t} C_{ij}(\tau). \tag{2.1.66}$$

This reparameterization of environmental Fourier-transformed correlation functions leads us to the following form of the interaction picture Master Equation, which we can write as

$$\frac{d\tilde{\rho}_S(t)}{dt} = -i\Big[\hat{H}_{LS}, \tilde{\rho}_S(t)\Big] + D[\tilde{\rho}_S(t)]. \tag{2.1.67}$$

provided that we define the *Lamb shift* Hamiltonian $\hat{H}_{LS}$ as

$$\hat{H}_{LS} = \sum_{\omega,i,j} \Sigma_{ij}(\omega)\hat{\sigma}^\dagger_i(w)\hat{\sigma}_j(\omega) \tag{2.1.68}$$

and the dissipative term as

$$D[\tilde{\rho}_S(t)] = \sum_{\omega,i,j} a_{ij}(\omega)\bigg(\hat{\sigma}_j(\omega)\tilde{\rho}_S(t)\hat{\sigma}^\dagger_i(\omega) - \frac{1}{2}\Big\{\hat{\sigma}^\dagger_i(\omega)\hat{\sigma}_j(\omega), \tilde{\rho}_S(t)\Big\}\bigg). \tag{2.1.69}$$

Thus, the microscopic derivation performed in this section led us to Eq. (2.1.67) which resembles Eq. (2.1.36). It can also be expressed in a Lindblad form by diagonalizing the positive [67] $a_{ij}(\omega)$ matrices defined in Eq. (2.1.66) through the following transformation

$$uau^\dagger = \begin{pmatrix} \gamma_1(\omega) & 0 & \cdots & 0 \\ 0 & \gamma_2(\omega) & \cdots & 0 \\ \vdots & \vdots & \ddots & \vdots \\ 0 & 0 & \cdots & \gamma_{N^2-1}(\omega) \end{pmatrix}. \tag{2.1.70}$$

which defines the following change of basis in the *Liouville* space of the system

$$\hat{\sigma}_i(\omega) = \sum_{j=1}^{N^2-1} u_{ij}\hat{A}_j(\omega). \tag{2.1.71}$$

Inserting this in Eq. (2.1.69) we obtain the following form of the dissipator

$$D[\tilde{\rho}_S(t)] = \sum_{\omega,j} \gamma_j(\omega)\bigg(\hat{A}_j(\omega)\tilde{\rho}_S(t)\hat{A}^\dagger_j(\omega) - \frac{1}{2}\Big\{\hat{A}^\dagger_j(\omega)\hat{A}_j(\omega), \tilde{\rho}_S(t)\Big\}\bigg). \tag{2.1.72}$$

Before concluding this section, we focus on some relevant observations. First of all, we observe that the *Lamb shift* Hamiltonian contributes to the dynamics by renormalizing the unperturbed energy levels of the systems. Moreover, we underline that in order to move back to Schrödinger picture, we only need to insert the free Hamiltonian of the system in the commutator in Eq. (2.1.67), obtaining

$$\frac{d\hat{\rho}_S(t)}{dt} = -i\Big[\hat{H}_S + \hat{H}_{LS}, \hat{\rho}_S(t)\Big] + D[\hat{\rho}_S(t)]. \tag{2.1.73}$$

Recalling the corresponding equation obtained in Section (2.1.1)

$$\frac{d\hat{\rho}_S(t)}{dt} = -i[K, \hat{\rho}_S(t)] + \sum_{j=1}^{N^2-1} \gamma_j \left\{ A_j \hat{\rho}_S(t) A_j^\dagger - \frac{1}{2} \left\{ A_j^\dagger A_j, \hat{\rho}_S(t) \right\} \right\} \tag{2.1.74}$$

it is easy to observe that it is of the same form of Eq. (2.1.73) with D defined in Eq. (2.1.72) provided that we identify K with $\hat{H}_S + \hat{H}_{LS}$ and introduce a spectral decomposition of operators $\hat{A}_j$, as done in order to obtain Eq. (2.1.72).

2.2 Collision models

As anticipated, in this section we will consider another way to treat open quantum systems known as *collision models*. In recent years, they have progressively gained more and more importance in the description of energy exchange between a quantum system and a bath, whose role can be played by an environment, which causes energy dissipation, but also by a charger, with opposite effects [10, 33]. The latter option has recently become very popular in literature, spreading in the field of quantum batteries [30, 31, 32, 33].
The key point of collision models consists in modeling the bath as a large collection of quantum subsystems described by a set of density matrices $\{\eta_n\}$, which interact sequentially with the system, and are labelled by an integer index denoting the position of the ancilla in the interaction sequence (see Fig. 2.1).

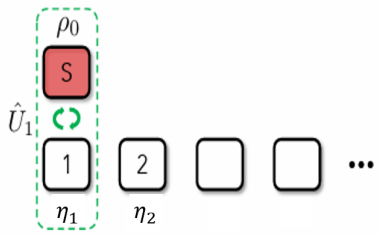

Figure 2.2: Scheme for the sequence of interactions involving the system, with initial density matrix ρ_0, and a single ancilla: S interacts at first with the first ancilla (described with the density matrix η_1) then with the second (described with η_2) and so on. Each ancilla interacts with S only once. Image taken from [34].

We will now derive some properties of collision models and, at the end of the section, we will compare them with the previously derived master equation descriptions. A more detailed discussion of the model can be found in Ref. [34].

2.2.1 Discrete-time evolution: quantum maps

As well as the approach discussed in the previous section, our goal is to study the evolution of the system density matrix. To do so, also in this case we will have to study the

evolution of the complete system and then trace over environmental degrees of freedom. Since our aim is to focus mainly on Markovian collision models, we now make two further assumptions which will simplify our treatment and which are essential to guarantee the Markovianity of the collision model. They consist in considering non interacting and initially uncorrelated ancillae, each of which couples only once with the system. Before starting, we point out that, from now on, the argument n of the reduced density matrix of the system $\hat{\rho}_S(n)$ will denote the interaction with the $n-th$ ancilla.
All considered, we can start building the global density matrix as

$$\hat{\rho}_{SB}(0) = \hat{\rho}_S(0) \otimes \hat{\eta}_1 ... \otimes \hat{\eta}_N \tag{2.2.1}$$

with

- $\hat{\rho}_S(0)$ the initial state of the system
- N the total number of ancillae which corresponds to the total number of collisions taking place in the sequence.

Our aim is to study the time evolution of the system density matrix $\hat{\rho}_S$. To do so, we will study the evolution of $\hat{\rho}_{SB}$, and then trace over the DOFs of the ancillae.
The Hamiltonian governing the $n-th$ step of this process consists in the sum of the free Hamiltonian of the system and of the ancilla, $\hat{H}_S$ and $\hat{H}_n$ respectively, together with their interaction term $\hat{V}_{Sn}$. Thus, considering

$$\hat{H} = \hat{H}_S + \hat{H}_n + \hat{V}_{Sn} \tag{2.2.2}$$

the time evolution of the density matrix $\hat{\rho}_S(n-1) \otimes \hat{\eta}_n$ is ruled by the following unitary operator in Schrödinger's picture

$$\hat{U}_n = e^{-i(\hat{H}_S + \hat{H}_n + \hat{V}_{Sn})\Delta t} \tag{2.2.3}$$

where Δt is the duration of the single collision. For the sake of simplicity we have assumed this time equal for each of the collisions considered, as well as small compared to the characteristic time scales of the systems, in order to drop any time dependence in $\hat{H}$ and simplify the time integral in the exponential defining the general evolution operator. These assumptions can however be relaxed [34].
Since we supposed non interacting ancillae, the first step of the collision model brings to [1]

$$\hat{\rho}_{SB}(1) = \hat{U}_1 \hat{\rho}_{SB}(0) \hat{U}_1^\dagger = \big(\hat{U}_1 \hat{\rho}_S(0) \otimes \hat{\eta}_1 \hat{U}_1^\dagger\big) \otimes \hat{\eta}_2 ... \otimes \hat{\eta}_N. \tag{2.2.4}$$

Iterating this procedure leads to the following expression for the global density matrix after n collisions:

$$\hat{\rho}_{SB}(n) = \big(\hat{U}_n ... \big(\hat{U}_1 \hat{\rho}_S(0) \otimes \hat{\eta}_1 \hat{U}_1^\dagger\big) ... \hat{\eta}_n \hat{U}_n^\dagger\big) \otimes \hat{\eta}_{n+1} ... \otimes \hat{\eta}_N. \tag{2.2.5}$$

Now we would like to trace over bath degrees of freedom. This can be done observing that contributions coming from different ancillae can be separated as

$$\hat{\rho}_S(n) = \mathrm{Tr}_n\big\{\hat{U}_n ... \mathrm{Tr}_1\big\{\hat{U}_1 \hat{\rho}_S(0) \otimes \hat{\eta}_1 \hat{U}_1^\dagger\big\} ... \hat{\eta}_n \hat{U}_n^\dagger\big\} \otimes \mathrm{Tr}_{n+1}\big\{\hat{\eta}_{n+1}\big\} ... \otimes \mathrm{Tr}_N\big\{\hat{\eta}_N\big\} \tag{2.2.6}$$

[1] We will denote with $\hat{\rho}_S(n)$ the system density matrix at $t = n\Delta t$

where last traces are trivially equal to 1 since they consist in tracing density matrices.
It is possible to rewrite Eq. (2.2.6) in order to properly highlight the Markovianity of the interaction process. To do so, we define a quantum map M_n which connects two subsequent steps of the system density matrix discrete evolution, namely

$$\hat{\rho}_S(n) = M_n\big[\hat{\rho}_S(n-1)\big] \tag{2.2.7}$$

which reduces, in our case, to

$$\hat{\rho}_S(n) = M_n\big[\hat{\rho}_S(n-1)\big] = \mathrm{Tr}_n\big\{\hat{U}_n\hat{\rho}_S(n-1)\otimes\hat{\eta}_n\hat{U}_n^\dagger\big\}. \tag{2.2.8}$$

Until now we have considered the general case of inhomogeneous collision model, where both the initial state and the interaction potential change from one ancilla to another, causing the presence of the subscript n in the definition of the quantum map. Inserting this last one in Eq (2.3.6) we are left with the following form

$$\hat{\rho}_S(n) = M_n\big[...M_1\big[\hat{\rho}_S(0)\big]\big] \tag{2.2.9}$$

which consist in successive application of the quantum maps. Since, at every step, the only input needed by the quantum map is the previous step density matrix, this process is clearly Markovian, thanks to all the assumptions made at the beginning of the section. If one makes the assumption of homogeneous collision model, steps are all equal and the evolution reduces to the repeated application of the same map M.

2.2.2 An example: Micromaser quantum map

In order to better clarify what discussed in the previous subsection, here we provide an example of a system which is suitable for a collision model description, namely the Micromaser [10]. The calculations we are about to perform will be useful for a better understanding of chapter three, where we will analyze how a Micromaser can be used to realize a quantum battery [33].
The Micromaser is a model where photons trapped into a resonant cavity interact with a stream of qubits and exchange energy with them. An ideal physical realization is shown in Fig. 2.3.
Ideally, it is possible to realize a sequence of interactions satisfying the Markovianity conditions: all one needs to do is to prepare uncorrelated qubits and send them to the cavity at a rate $r = \frac{1}{\tau}$ such that $\tau > \Delta t$, where again Δt denotes the duration of the interaction, which can be controlled through fine-tuning of the velocity of atoms flying in the cavity.
In the following, we will assume that all these precautions have been taken into account, and treat the interaction process as Markovian.

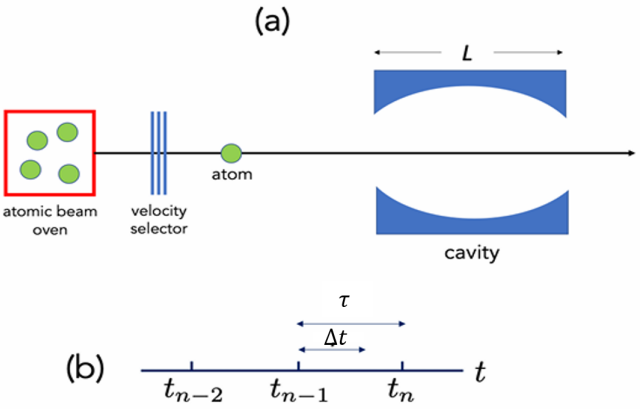

Figure 2.3: (a)Scheme of an ideal experimental Micromaser setup. Here, a flow of atoms with a selected velocity enters a cavity of length L. Controlling the velocity allows to tune the interaction duration Δt (b) Graphical representation of relevant time scales involved in the problem: the duration of each interaction Δt must be shorter than the time interval separating the emission of two subsequent atoms τ. Picture taken from [34].

We begin our calculations from the definition of the mode-qubit Hamiltonian, supposed of the form

$$\hat{H} = \hat{H}_S + \hat{H}_n + \hat{V}_{Sn} \tag{2.2.10}$$

where

$$\hat{H}_S = \omega_c \hat{a}^\dagger \hat{a} \tag{2.2.11}$$

$$\hat{H}_n = \frac{\Delta}{2} \hat{\sigma}_{z,n} \tag{2.2.12}$$

$$\hat{V}_{Sn} = g(\hat{a}^\dagger + \hat{a})(\hat{\sigma}_{-,n} + \hat{\sigma}_{+,n}) \tag{2.2.13}$$

respectively represent the Hamiltonian of the cavity mode considered (see Sec. 1.3.2), the Hamiltonian of the TLS ancilla and the coupling between these two systems [46] which is supposed to be identical for each ancilla.
It is easier to move to the interaction picture with respect to $\hat{H}_S + \hat{H}_n$, so that the interaction term becomes

$$\tilde{V}_{Sn} = g\big(\hat{a}^\dagger \hat{\sigma}_+ e^{i(\Delta+\omega_c)t} + \hat{a}^\dagger \hat{\sigma}_- e^{i(\omega_c-\Delta)t} + \hat{a}\hat{\sigma}_+ e^{i(\Delta-\omega_c)t} + \hat{a}^\dagger \hat{\sigma}_+ e^{-i(\Delta+\omega_c)t}\big). \tag{2.2.14}$$

We focus now on the resonant case $\Delta = \omega_c$, which leads to

$$\tilde{V}_{Sn} = g\big(\hat{a}^\dagger \hat{\sigma}_+ e^{2i\omega_c t} + \hat{a}^\dagger \hat{\sigma}_- + \hat{a}\hat{\sigma}_+ + \hat{a}^\dagger \hat{\sigma}_+ e^{-2i\omega_c t}\big). \tag{2.2.15}$$

Despite moving to interaction picture, we are left with a time evolution problem which is not exactly solvable and needs to be handled numerically. However, a possible way out is represented by the *Rotating wave approximation* (RWA) which, as discussed in Sec. (1.5.2), consists in neglecting oscillating terms in Eq. (2.3.15) since their contribution reveals to be negligible for small values of the ratio $\frac{g}{\omega_c}$.
Thus, performing this approximation leads to reliable results only in the weak coupling regime $g \ll \omega_c$, but they can be extended to the strong coupling regime $g \sim \omega_c$ via

external modulation of cavity and qubit frequencies, as shown in [71]. This leaves us with the *Jaynes-Cummings* (JC) interaction Hamiltonian

$$\tilde{V}_{Sn} = g\big(\hat{a}\hat{\sigma}_+ + \hat{a}^\dagger\hat{\sigma}_-\big). \tag{2.2.16}$$

Due to the fact that Eq. (2.3.16) is now time independent, the evolution operator in interaction picture can be written as

$$\tilde{U}_n = e^{-i\tilde{V}_{Sn}\Delta t}. \tag{2.2.17}$$

In order to characterize the time evolution of the system, the first thing we need to do is to diagonalize V_{Sn}. Projecting this operator on the complete system orthonormal basis obtained with a tensor product between the Fock basis of the oscillator and the spin basis of the qubit, namely the set $\big\{|m,\pm\rangle\big\}$, it is straightforward to obtain the following block-diagonal form:

$$\tilde{V}_{Sn} = \begin{pmatrix} \ddots & 0 & 0 & 0 \\ 0 & \begin{matrix} 0 & g\sqrt{m+1} \\ g\sqrt{m+1} & 0 \end{matrix} & 0 & 0 \\ 0 & 0 & \begin{matrix} 0 & g\sqrt{m} \\ g\sqrt{m} & 0 \end{matrix} & 0 \\ 0 & 0 & 0 & \ddots \end{pmatrix}. \tag{2.2.18}$$

This matrix is clearly infinite-dimensional due to the infinite dimension of the oscillator Fock space. Its block-diagonal structure is a consequence of the conservation of the number of excitations associated to the RWA Hamiltonian and makes the diagonalization simpler, since it is sufficient to focus on a single two-dimensional subspace, like that spanned by $\big\{|m-1,1\rangle, |m,0\rangle\big\}$, obtaining

$$\tilde{V}_{Sn} = \begin{pmatrix} 0 & g\sqrt{m} \\ g\sqrt{m} & 0 \end{pmatrix}. \tag{2.2.19}$$

Given its eigenvalues

$$\Lambda_{1,2} = \pm g\sqrt{m} \tag{2.2.20}$$

and eigenvectors

$$|\psi_{1,2}\rangle = \frac{1}{\sqrt{2}}(|m-1,+\rangle \pm |m,-\rangle) \tag{2.2.21}$$

respectively, we can write, in this subspace, the time evolution operator in Eq. (2.2.17) as

$$\tilde{U}_n = e^{-ig\Delta t\sqrt{m}}\,|\psi_1\rangle\langle\psi_1| + e^{ig\Delta t\sqrt{m}}\,|\psi_2\rangle\langle\psi_2|\,. \tag{2.2.22}$$

In order to regain the complete structure of the full Hilbert space, we sum over the integer index m. Doing this, and using Eq. (2.2.21) we arrive, after a bit of algebra, to:

$$\begin{aligned} \tilde{U}_n = {} & |+\rangle\langle+|_n \left\{\sum_{m=0}^{\infty} |m\rangle\langle m|\,\mathrm{Cos}(g\Delta t\sqrt{m+1})\right\} + \\ & + |-\rangle\langle-|_n \left\{\sum_{m=1}^{\infty} |m\rangle\langle m|\,\mathrm{Cos}(g\Delta t\sqrt{m})\right\} + \\ & -i\,|+\rangle\langle-|_n \left\{\sum_{m=0}^{\infty} |m\rangle\langle m+1|\,\mathrm{Sin}(g\Delta t\sqrt{m+1})\right\} + \\ & -i\,|-\rangle\langle+|_n \left\{\sum_{m=1}^{\infty} |m+1\rangle\langle m|\,\mathrm{Sin}(g\Delta t\sqrt{m+1})\right\}. \end{aligned} \tag{2.2.23}$$

Therefore the interaction picture evolution operator is given by the sum of four terms, each of which can be factorized as the tensor product of a qubit part and a quantum oscillator one. Defining $\hat{N}$ as the oscillator number operator, it is straightforward to demonstrate that the following relations hold

$$\sum_{m=0}^{\infty} |m\rangle\langle m| \operatorname{Cos}(g\Delta t\sqrt{m+1}) = \operatorname{Cos}(g\Delta t\sqrt{\hat{N}+\hat{I}}) := \hat{B} \tag{2.2.24}$$

$$\sum_{m=1}^{\infty} |m\rangle\langle m| \operatorname{Cos}(g\Delta t\sqrt{m}) = \operatorname{Cos}(g\Delta t\sqrt{\hat{N}}) := \hat{C}. \tag{2.2.25}$$

Similarly, the last two terms in Eq. (2.3.23) can be rewritten defining a new operator $\hat{S}$ such that

$$\hat{S} := \frac{\operatorname{Sin}(g\Delta t\sqrt{\hat{N}+\hat{I}})}{\sqrt{\hat{N}+\hat{I}}} \tag{2.2.26}$$

which leads to

$$\sum_{m=0}^{\infty} |m\rangle\langle m+1| \operatorname{Sin}(g\Delta t\sqrt{m+1}) = \hat{S}\hat{a} \tag{2.2.27}$$

$$\sum_{m=0}^{\infty} |m+1\rangle\langle m| \operatorname{Sin}(g\Delta t\sqrt{m+1}) = \hat{a}^{\dagger}\hat{S}. \tag{2.2.28}$$

All these definitions lead to the following expression for the evolution operator

$$\tilde{U}_n = \hat{B}\,|+\rangle\langle+|_n + \hat{C}\,|-\rangle\langle-|_n - i\big\{\hat{S}\hat{a}\,|+\rangle\langle-|_n + \hat{a}^{\dagger}\hat{S}\,|-\rangle\langle+|_n\big\} \tag{2.2.29}$$

which we will use to construct the collision model quantum map.
In an homogeneous collision model, we can define the ancilla density matrix as

$$\hat{\eta}_n = q\,|-\rangle\langle-|_n + (1-q)\,|+\rangle\langle+|_n + c\sqrt{q(1-q)}(|-\rangle\langle+|_n + |+\rangle\langle-|_n) \tag{2.2.30}$$

with q controlling the qubit ground state occupation and c the degree of coherence of the qubit.
In order to obtain the quantum map we need now to evaluate

$$\tilde{\rho}_S(n) = \operatorname{Tr}_n\big\{\tilde{U}_n(\tilde{\rho}_S(n-1)\otimes\hat{\eta})\tilde{U}_n^{\dagger}\big\}. \tag{2.2.31}$$

Thus, using the expression for U_n given by Eq. (2.2.29) and the definition of $\hat{\eta}_n$ the result yields

$$\begin{aligned}
\tilde{\rho}_S(n) = \operatorname{Tr}_n\Big\{ & |+\rangle\langle+|_n \Big[(1-q)\hat{B}\tilde{\rho}_S(n-1)\hat{B} + q\hat{S}\hat{a}\tilde{\rho}_S(n-1)\hat{a}^{\dagger}\hat{S} + \\
& + ic\sqrt{q(1-q)}\big(\hat{B}\tilde{\rho}_S(n-1)\hat{a}^{\dagger}\hat{S} - \hat{S}\hat{a}\tilde{\rho}_S(n-1)\hat{B}\big)\Big] + \\
& + |-\rangle\langle-|_n \Big[q\hat{C}\tilde{\rho}_S(n-1)\hat{C} + (1-q)\hat{a}^{\dagger}\hat{S}\tilde{\rho}_S(n-1)\hat{S}\hat{a} + \\
& + ic\sqrt{q(1-q)}\big(\hat{C}\tilde{\rho}_S(n-1)\hat{S}\hat{a} - \hat{a}^{\dagger}\hat{S}\tilde{\rho}_S(n-1)\hat{C}\big)\Big] + \dots \Big\}
\end{aligned} \tag{2.2.32}$$

where the ellipsis stands for the off diagonal terms of the qubit density matrix. These terms do not contribute to the partial trace defining $\rho_S(n)$ and can therefore be neglected. Performing this last trace one gets to

$$\begin{aligned}\tilde{\rho}_S(n) = (1-q)\Big\{\hat{B}\tilde{\rho}_S(n-1)\hat{B} + \hat{a}^\dagger\hat{S}\tilde{\rho}_S(n-1)\hat{S}\hat{a}\Big\}+ \\ +q\Big\{\hat{C}\tilde{\rho}_S(n-1)\hat{C} + \hat{S}\hat{a}\tilde{\rho}_S(n-1)\hat{a}^\dagger\hat{S}\Big\}+ \\ +ic\sqrt{q(1-q)}\Big\{\hat{C}\tilde{\rho}_S(n-1)\hat{S}\hat{a} - \hat{a}^\dagger\hat{S}\tilde{\rho}_S(n-1)\hat{C}+ \\ + \hat{B}\tilde{\rho}_S(n-1)\hat{a}^\dagger\hat{S} - \hat{S}\hat{a}\tilde{\rho}_S(n-1)\hat{B}\Big\}.\end{aligned} \tag{2.2.33}$$

This last equation, as we will see in chapter three, is the fundamental ingredient to perform numerical simulations for the evolution of the state of a Micromaser charged via sequential interactions with a stream of qubits.

2.2.3 The short collision time limit

In order to compare the collisional approach with the methods discussed in Section (2.1), it is useful to study the small collision time limit of the discrete collision models. In order to simplify the notation we restrict ourselves to homogeneous collision models. Thus, our starting point is the homogeneous version of Eq. (2.2.8), namely

$$\hat{\rho}_S(n) = \mathrm{Tr}_n\big\{\hat{U}(\hat{\rho}_S(n-1)\otimes\hat{\eta})\hat{U}^\dagger\big\}. \tag{2.2.34}$$

Working in interaction picture we recall Eq. (2.2.14) for the unitary evolution operator $\hat{U}$ as

$$\tilde{U} = e^{-i\Delta t\tilde{V}_{Sn}}. \tag{2.2.35}$$

We will also assume the system-ancilla coupling Hamiltonian to be of the form

$$\tilde{V}_{Sn} = \sum_j \tilde{\sigma}_j\otimes\tilde{B}_j \tag{2.2.36}$$

in analogy to what done in Eq. (2.1.45). If Δt is much smaller compared to the characteristic time scales of the system we can expand Eq. (2.2.34) in the interaction picture as

$$\begin{aligned}\tilde{U}\tilde{\rho}_S(n-1)\otimes\eta\tilde{U}^\dagger = \tilde{\rho}_S(n-1) - i\Delta t\mathrm{Tr}_n\big\{\Big[\tilde{V}_{Sn},\tilde{\rho}_S(n-1)\otimes\hat{\eta}\Big]\big\}+ \\ -\frac{\Delta t^2}{2}\mathrm{Tr}_n\big\{\Big[\tilde{V}_{Sn},\Big[\tilde{V}_{Sn},\tilde{\rho}_S(n-1)\Big]\otimes\hat{\eta}\Big]\big\}.\end{aligned} \tag{2.2.37}$$

Due to the assumption made in Eq. (2.2.36), the first order commutator appearing in the above equation can be rearranged as follows

$$\mathrm{Tr}_n\big\{\Big[\tilde{V}_{Sn},\tilde{\rho}_S(n-1)\otimes\hat{\eta}\Big]\big\} = \Big[\mathrm{Tr}_n\big\{\tilde{V}_{Sn}\otimes\hat{\eta}\big\},\tilde{\rho}_S(n-1)\Big]. \tag{2.2.38}$$

If we expand the second order commutator in Eq. (2.2.37) and divide by Δt we obtain

$$\begin{aligned}\frac{\Delta\tilde{\rho}_S(n)}{\Delta t} &= -i\Big[\mathrm{Tr}_n\big\{\tilde{V}_{Sn}\otimes\hat{\eta}\big\},\tilde{\rho}_S(n-1)\Big]+\\ &+\Delta t\mathrm{Tr}_n\Big\{\tilde{V}_{Sn}(\tilde{\rho}_S(n-1)\otimes\hat{\eta})\tilde{V}_{Sn}-\frac{1}{2}\Big\{\tilde{V}_{Sn},\tilde{\rho}_S(n-1)\otimes\hat{\eta}\Big\}\Big\}.\end{aligned} \tag{2.2.39}$$

As shown in [34], performing a spectral decomposition of the ancilla density matrix

$$\hat{\eta}=\sum_{\alpha}p_\alpha\,|\alpha\rangle\langle\alpha| \tag{2.2.40}$$

and defining the following set of operators

$$L_{\alpha,\beta}=\sqrt{p_\alpha\Delta t}\,\langle\beta|\tilde{V}_{Sn}|\alpha\rangle \tag{2.2.41}$$

leads to the following form for Eq. (2.2.36)

$$\begin{aligned}\frac{\Delta\tilde{\rho}_S(n)}{\Delta t} &= -i\Big[\mathrm{Tr}_n\big\{\tilde{V}_{Sn}\otimes\hat{\eta}\big\},\tilde{\rho}_S(n-1)\Big]+\\ &+\sum_{\alpha,\beta}L_{\alpha,\beta}\tilde{\rho}_S(n-1)L^\dagger_{\alpha,\beta}-\frac{1}{2}\Big\{L^\dagger_{\alpha,\beta}L_{\alpha,\beta},\tilde{\rho}_S(n-1)\Big\}.\end{aligned} \tag{2.2.42}$$

This equation can be seen as the discretized version of Eq. (2.1.67), provided that we define

$$\hat{H}_{LS}=\mathrm{Tr}_n\big\{\tilde{V}_{Sn}\otimes\hat{\eta}\big\} \tag{2.2.43}$$

$$D[\tilde{\rho}_S(t)]=\sum_{\alpha,\beta}L_{\alpha,\beta}\tilde{\rho}_S(n-1)L^\dagger_{\alpha,\beta}-\frac{1}{2}\Big\{L^\dagger_{\alpha,\beta}L_{\alpha,\beta},\tilde{\rho}_S(n-1)\Big\}. \tag{2.2.44}$$

So far, we have not carried out the proper continuous time limit, considering a finite and small Δt such that the time evolution operator could be replaced by its second order expansion. However, if the total evolution time of the system is much greater than Δt, it is possible to apply a coarse graining procedure which consists in replacing the discretized time with a continuous variable, namely

$$t_n=n\Delta t\to t. \tag{2.2.45}$$

In doing so, all functions depending on the step number n become continuous evolving functions. The price to be paid is that the new approach will not provide us with any useful information on the dynamics of the system at time scales smaller than Δt.
Coarse graining procedure allows us not to perform the rigorous limit $\Delta t\to 0$ which is a delicate step since, as expressed in Eqs. (2.3.41)-(2.3.42), it would make the dissipative terms to disappear. One possible way out would consists in performing this limit together with the introduction of a diverging coupling strength so that $L_{\alpha,\beta}$ Lindblad operators remain finite. This procedure is very delicate since it may cause other non-physical behaviours, as shown in [34].

2.2.4 Towards collisional quantum batteries

As seen in this section, collision models represent a valid alternative to continuous time approaches in the description of open quantum systems. Along the entire section we have considered quantum systems coupled with a bath B. Usually, the role of B is played by an external environment which causes dissipative phenomena, but nothing prevents from employing these models in situations where B causes opposite effects. As we will see in the following, this is the case of collisional quantum batteries, whose charging protocol can be described by a collision model where the bath B acts as a charger. Obviously, collision models could be used also in hybrid situations, where a system interacts both with a charger and with an environment, both described by a collection of quantum systems. An example of this situation can be found in [32].

Chapter 3

Harmonic collisional quantum batteries: the Micromaser

In this chapter we will consider in more details one of the most relevant examples of collisional quantum batteries, known as the Micromaser, already introduced briefly in Sec. 2.2.2. Although this system has been extensively studied both at the theoretical and experimental level [72, 73] and many works, focused on the creation of Micromaser pure states, have been proposed [73, 74], the majority of them is based on assumptions such as weak or highly fine-tuned values of the coupling, which are incompatible with the possibility of building a fast-charging and stable battery. It is possible to show [32, 33], however, that assuming a Jaynes-Cummings (JC) collision model with a stream of coherent qubits as a charger leads to an interesting behaviour of the system in terms of

- **stored energy and purity**, since the charging process drives the system towards an highly-excited and almost pure steady state;
- **stability** with respect to coupling fluctuations and small losses of coherence of charging qubits.

The upsaid features are due to the so called *trapping dynamics* of the JC collision model. This consists in the fact that the system is driven towards an almost pure steady state, localized in a finite-size region of the cavity Hilbert space, provided that the coupling interaction is properly fine-tuned [32, 33, 73]. This trapping condition can be achieved both in the coherent and incoherent case, leading to different kind of steady states. What makes the coherent protocol more promising is its stability with respect to deviations of the coupling from fine-tuned values, whereas in the incoherent case [32], such deviations break of the *trapping dynamics*.
We will use here results from Sec. 2.2.2 as the starting point and will retrace the work done in [32, 33].
In the first section we will focus on the main analytical features of incoherent [32] and coherent [73, 74] collisional charging of an harmonic oscillator, above all the possibility of building excited and almost pure steady states under proper conditions.
Subsequently we will numerically retrace the work done in [32, 33]. After analyzing the presence of trapping states in the incoherent case and showing their instability with respect to the breaking of the trapping condition discussed above, we will proceed further by gradually increasing quantum coherences until reaching the fully-coherent protocol. In

doing so, we will go beyond existing literature, since intermediate coherences have not yet been investigated. For each of the regimes studied we will show results for the stored energy and state purity of the battery, also analyzing its density matrix to properly visualize trapping states.
At the end of the chapter we will discuss the stability of the obtained results with respect to the introduction of counter rotating terms in the coupling Hamiltonian.

3.1 Micromaser dynamics

Before starting, we recall Eq. (2.2.30) for the quantum map of the Micromaser homogeneous collision model in the JC limit, given by

$$\begin{aligned}\tilde{\rho}_S(n) = (1-q)\Big\{\hat{B}\tilde{\rho}_S(n-1)\hat{B} + \hat{a}^\dagger\hat{S}\tilde{\rho}_S(n-1)\hat{S}\hat{a}\Big\}+\\ +q\Big\{\hat{C}\tilde{\rho}_S(n-1)\hat{C} + \hat{S}\hat{a}\tilde{\rho}_S(n-1)\hat{a}^\dagger\hat{S}\Big\}+\\ +ic\sqrt{q(1-q)}\Big\{\hat{C}\tilde{\rho}_S(n-1)\hat{S}\hat{a} - \hat{a}^\dagger\hat{S}\tilde{\rho}_S(n-1)\hat{C}+\\ + \hat{B}\tilde{\rho}_S(n-1)\hat{a}^\dagger\hat{S} - \hat{S}\hat{a}\tilde{\rho}_S(n-1)\hat{B}\Big\}\end{aligned} \tag{3.1.1}$$

where $\tilde{\rho}_S(n)$, with $n \geq 1$ denoting the current step, is the reduced Micromaser density matrix, whereas c and q respectively represent the degree of coherence and the ground state population of each ancilla (see Sec. 2.2.2). $\hat{B}, \hat{C}, \hat{S}$ were defined in Eqs. (2.2.21)-(2.2.23) as functions of both the number operator of the cavity $\hat{N}$ and θ, which is given by the product of the system-ancilla coupling with the single interaction duration, namely $\theta = g\Delta t$.
This form of the quantum map was derived using the RWA [46]. Although neglecting counter rotating terms strongly reduces the dimension of the Hilbert's space and reveals to be crucial in order to simplify the interaction picture evolution operator used to derive Eq. (3.1.1), its validity is limited to the weak coupling regime $g \ll \omega_c$ of the resonant interaction between the system and each ancilla [46]. This makes it substantially incompatible with the fast charging of a battery [33]. Thus, a desirable situation would be to have a system described by a Jaynes-Cummings Hamiltonian also in the ultrastrong coupling regime (USC) $0.1 \lesssim \frac{g}{\omega_c} \lesssim 1$. As already mentioned in Section (2.2.2), this can be accomplished via an external modulation of the cavity and qubits frequencies [71]. Following the approach developed in [32, 33], we will assume this modulation has been performed and push our numerical analysis up to USC, postponing considerations on the relevance of counter rotating terms to Sec. 3.2.3.

3.1.1 Incoherent charging protocol

In this case, $c = 0$, thus Eq. (3.1.1) reads

$$\begin{aligned}\tilde{\rho}_S(n) = (1-q)\big\{\hat{C}\tilde{\rho}_S(n-1)\hat{C} + \hat{a}^\dagger\hat{S}\tilde{\rho}_S(n-1)\hat{S}\hat{a}\big\}+\\ +q\big\{\hat{B}\tilde{\rho}_S(n-1)\hat{B} + \hat{S}\hat{a}\tilde{\rho}_S(n-1)\hat{a}^\dagger\hat{S}\big\}.\end{aligned} \tag{3.1.2}$$

We now focus on the k–th diagonal element

$$\tilde{\rho}_{S,k}(n) \equiv \langle k|\tilde{\rho}_S(n)|k\rangle \tag{3.1.3}$$

where $|k\rangle$ represents the k–th cavity eigenstate. Considering the action of the operators $\hat{B}$, $\hat{C}$ and $\hat{S}$ on the number states we can rewrite Eq. (3.1.3) as

$$\begin{aligned}\tilde{\rho}_{S,k}(n+1) = r_{k+1}^2(\theta)\Big[q\tilde{\rho}_{S,k+1}(n) - (1-q)\tilde{\rho}_{S,k}(n)\Big] + \\ + r_k^2(\theta)\Big[(1-q)\tilde{\rho}_{S,k-1}(n) - q\tilde{\rho}_{S,k}(n)\Big] + \tilde{\rho}_{S,k}(n),\end{aligned} \tag{3.1.4}$$

where

$$r_k(\theta) \equiv \mathrm{Sin}(\theta\sqrt{k}). \tag{3.1.5}$$

This equation clarifies the reason behind the choice of focusing only on the populations of the cavity density matrix, since it implies that populations at a given step n only depend on preceding populations, with no off-diagonal term contributing to the process.
The dynamics described by this equation turns out to be peculiar for appropriate values of θ given by

$$\theta_{ft} = \frac{\pi}{\sqrt{l}} \quad \rightarrow \quad r_l(\theta_{ft}) = 0 \tag{3.1.6}$$

with l a positive integer. We start discussing this point by further simplifying the dynamics, assuming ancillae to be completely excited, that is, setting $q = 0$ in Eq. (3.1.4). Since we are looking for steady states we must solve the equation

$$r_{k+1}^2(\theta)\tilde{\rho}_{S,k}(n) - r_k^2(\theta)\tilde{\rho}_{S,k-1}(n) = 0. \tag{3.1.7}$$

The striking consequence of setting $\theta = \theta_{ft}$ is that this steady state condition is satisfied by a state ρ_S^{stat} such that [32]

$$\rho_{S,k}^{stat} = \delta_{k,l-1}. \tag{3.1.8}$$

Thus, by properly fine-tuning the coupling and the duration of the interaction, a collisional charging process with completely excited and incoherent qubits drives the system towards the number state $|l-1\rangle$. This property is known as *trapping*.
As anticipated in Sec. 1.4, purity is strictly connected to ergotropy, since a pure state of the battery optimizes the amount of extractable work. Given the importance of this feature in view of realizing stable quantum batteries, it would be desirable to obtain something similar also in more general situations, where $q \neq 0$ and $c \neq 0$ and also where the coupling is not fine tuned.
We now try to extend these considerations to the $q \neq 0$ case, postponing the coherent protocol to the following subsection. We can study this case starting from Eq. (3.1.4). If $q \neq 0$ the stationary state condition takes the form

$$r_{k+1}^2(\theta)\big[q\tilde{\rho}_{S,k+1}(n) - (1-q)\tilde{\rho}_{S,k}(n)\big] + r_k^2(\theta)\big[(1-q)\tilde{\rho}_{S,k-1}(n) - q\tilde{\rho}_{S,k}(n)\big] = 0. \tag{3.1.9}$$

As pointed out in [32], using again Eq. (3.1.6) for the value of θ the solution of this equation takes the form

$$\rho_{S,k}^{stat} = \begin{cases} R^k f(R) & \text{if } k < l \\ 0 & \text{if } k \geq l \end{cases} \tag{3.1.10}$$

where

$$f(R) = \frac{R-1}{R^{l+1}-1} \tag{3.1.11}$$

$$R = \frac{1-q}{q}. \tag{3.1.12}$$

This implies that the *trapping dynamics* is preserved, since the non-zero steady state populations are confined in a part of the system density matrix with $0 \leq k < l$, but modified, since the state is no longer a number state.
For what concerns purity, given the fact that the Micromaser density matrix in the incoherent case is diagonal, it can be evaluated as

$$P(n) = \mathrm{Tr}_S\{\tilde{\rho}_S^2(n)\} = \sum_k \tilde{\rho}_{S,k}^2(n). \tag{3.1.13}$$

Using the stationary state defined in Eq. (3.1.10) we are left with [32]

$$P^{stat} = \frac{R-1}{R+1}\frac{(R^2)^{l+1}-1}{(R^{l+1}-1)^2}. \tag{3.1.14}$$

To get a sense of its values, we can consider the fact that, for sufficiently large R, it can be approximated as

$$P^{stat} \approx \frac{R-1}{R+1} = 1-2q. \tag{3.1.15}$$

This implies that, if the charging qubits are not completely excited, the purity of the steady state lowers, causing the ergotropy to lower in turn.
What remains to be considered is the case of non fine-tuned values for the coupling g. In such a situation, the steady state equation does not admit a trapping solution. As we will see in Sec. 3.2.1, a numerical approach shows that this has relevant consequences in terms of storage and stability of the battery.
To summarize, an incoherent collision model drives the system towards a *trapping* steady state only if the coupling is fine tuned as expressed in Eq. (3.1.6). The resulting trapping state is pure only if $q = 0$ whereas, if $q \neq 0$, its purity decreases.

3.1.2 Coherent charging protocol

Now it is time to re-introduce quantum coherent ancillae in the Micromaser collision charging process. In order to study the resulting dynamics, we will follow the approach of [73, 74].
In order to simplify the treatment, we momentarily leave aside the study of the Micromaser density matrix and begin analyzing the following state for the oscillator-ancilla composite system at the beginning of the n–th step of the collision model

$$|\psi_i(n)\rangle = \sum_k \lambda_k |k\rangle \otimes (\sqrt{1-q}\,|+\rangle_n + \sqrt{q}\,|-\rangle_n) \tag{3.1.16}$$

written in terms of the number basis $\{|k\rangle\}$ and the ancilla basis $\{|\pm\rangle_n\}$. The n–th step of the model is governed, in the interaction picture, by the unitary operator defined in Eq. (2.2.26)

$$\tilde{U}_n = \hat{B}\,|+\rangle\langle+|_n + \hat{C}\,|-\rangle\langle-|_n - i\{\hat{S}\hat{a}\,|+\rangle\langle-|_n + \hat{a}^\dagger\hat{S}\,|-\rangle\langle+|_n\}.$$

This leads to the following form of the system-ancilla state at the end of the n–th step [73]

$$|\psi_f(n)\rangle = |f_+\rangle \otimes |+\rangle_n + |f_-\rangle \otimes |-\rangle_n \tag{3.1.17}$$

where

$$|f_+\rangle = \sum_k \lambda_k \{ \sqrt{1-q}\,\mathrm{Cos}\Big(\theta\sqrt{k+1}\Big)\,|k\rangle - i\sqrt{q}\,\mathrm{Sin}\Big(\theta\sqrt{k}\Big)\,|k-1\rangle \} \tag{3.1.18}$$

$$|f_-\rangle = \sum_k \lambda_k \{ \sqrt{q}\,\mathrm{Cos}\Big(\theta\sqrt{k}\Big)\,|k\rangle - i\sqrt{1-q}\,\mathrm{Sin}\Big(\theta\sqrt{k+1}\Big)\,|k+1\rangle \}. \tag{3.1.19}$$

Thus, if, at a given step of the collision model, the state $|k\rangle$ is populated then the two states $|k+1\rangle$ and $|k-1\rangle$ will be populated at the subsequent step, with respective populations given by $\mathrm{Sin}^2(\theta\sqrt{k+1})$ and $\mathrm{Sin}^2(\theta\sqrt{k})$. Now it is time to define a particular state $|k_p\rangle$ such that

$$\sqrt{k_p+1}\theta = p\pi \tag{3.1.20}$$

with p a positive integer. Under the above condition the population of $|k_p+1\rangle$ at the subsequent step is zero and we will we will call it an *upward trapping state*. Analogously if

$$\sqrt{k_p}\theta = p\pi \tag{3.1.21}$$

we will call it a *downward trapping state*, since now the non-populated state is $|k_p-1\rangle$. A direct consequence of these definitions is that a *upward trapping state* is always followed by a *downward trapping state*. This has very important consequences on the system dynamics: let us suppose that, given a value of the coupling θ_p, there exist two integers p, k_p which satisfy Eq. (3.1.21). Then, the system states space will be separated by $|k_p\rangle$ into dynamically disconnected sections, one with $k \leq k_p$ and the other with $k > k_p$.
As shown in [73] it is possible to set up a self-consistency argument in order to demonstrate the possibility of building an almost pure steady state in one of these disconnected blocks. We only report the following recursive relations between the populations of the harmonic oscillator in such a steady state. One must have, $\forall\ k < k_p$,

$$\rho^{stat}_{S,k} = \frac{1-q}{q}\mathrm{Cot}^2\left(\frac{\pi}{2\sqrt{k_p}}\sqrt{k}\right)\rho^{stat}_{S,k-1}. \tag{3.1.22}$$

This formula will be useful in the following section, where numerical results will show that, although the coherent charging protocol has better performances in terms of stability for a given value the coupling, the stored energy is lower than the one in the incoherent case. The reason for this is the difference between populations of the coherent and incoherent protocol steady state. Indeed, while in the first case the cotangent factors in Eqs. (3.1.22) suppress populations of states with k near k_p, this does not happen in the incoherent one.

3.2 Charging up the Micromaser

In this section we will show results of the numerical simulations carried out to study the Micromaser collision model, at first concentrating only on the resonant JC evolution, which was studied analytically above. For this case we will assume that the quantum map describing the process is the one obtained in Sec. 2.2.2. This will be evaluated numerically

step by step by employing methods provided by the QuTiP library [35].
Subsequently, we introduce the effects of counter rotating terms. Since their presence do not allow to solve exactly the dynamics of the system, we will resort to approximated methods of the same library. Further details on the numerical implementation can be found in the Appendix.
The relevant parameters for the numerical calculations are: q and c, pure real numbers respectively representing the population of the ground state of each ancilla and their degree of coherence, both assumed the same at each step; $\theta = g\Delta t$, with Δt the duration of each interaction of the collision model, since the operators in the quantum map of Eq. (2.2.30) depend on its value. Without loss of generality, we will assume Δt as our reference time unit, so that other physical quantities will be rescaled accordingly.
In all simulations we will consider an initially completely discharged Micromaser (empty battery) with density matrix

$$\tilde{\rho}_S(0) = |0\rangle\langle 0| \,. \tag{3.2.1}$$

3.2.1 Incoherent protocol

We begin our numerical analysis with the study of the fully-incoherent collision model. As seen in Sec. 3.1.1 the expected trapping steady state will be diagonal on the basis of eigenvectors of the Micromaser, its purity will depend on q values and it will be destroyed by deviations of the coupling with respect to fine-tuned values.
We will show this for fine tuned coupling values of the form given by Eq. (3.1.6), with $l = 12$ and $l = 39$, comparing results for each of these with results obtained for a corresponding non-fine tuned value. For all simulations of the incoherent protocol we will assume $c = 0$ and $q = 0.25$, independently of the considered coupling.

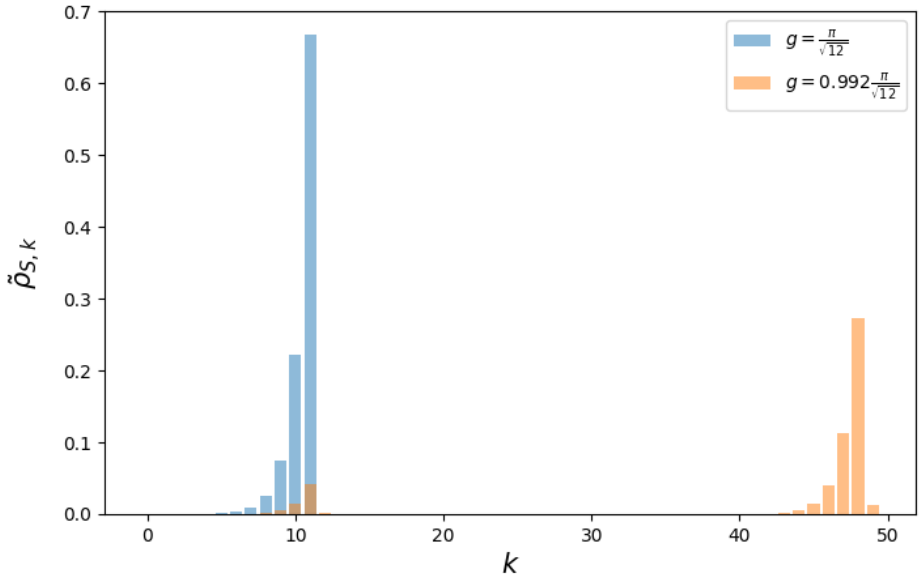

Figure 3.1: Populations of the Micromaser state after 10000 collisions: comparison between $g = \frac{\pi}{\sqrt{12}}$ (fine-tuned) and $g = 0.992\frac{\pi}{\sqrt{12}}$ (non fine-tuned) assuming $c = 0$, $q = 0.25$, $\Delta t = 1$. Here, k denotes the k–th diagonal element of the density matrix taken into account (same notation as that employed in Sec. 3.1.1).

We begin by showing the breaking of the trapping condition through plots of the populations of the system density matrix, since the incoherent dynamics only affects its diagonal elements. In Fig. 3.1 we show the populations of $\rho_{S,k}^{stat}$ for two selected values of the coupling. As we expected, in the fine-tuned case $g = \frac{\pi}{\sqrt{12}}$ the system is trapped within a region of the cavity Hilbert's space with $k \leq 11$, whereas this trapping condition is broken for the non fine-tuned case $g = 0.992\frac{\pi}{\sqrt{12}}$, since the steady state populations are no more localized and the finite-size computational Hilbert's space is almost saturated.
After displaying trap states and their breaking, it is worth discussing the consequences of these facts. We will analyze the stored energy and purity as functions of the number of completed steps of the collision model, namely

$$E(n) = \mathrm{Tr}\{H_S \tilde{\rho}_S(n)\} \tag{3.2.2}$$

$$P(n) = \mathrm{Tr}\{\tilde{\rho}_S^2(n)\}. \tag{3.2.3}$$

Results shown in Figs. 3.2 and 3.3 for the stored energy and purities with $q = 0.25$ confirm what we anticipated: non fine-tuned values of the coupling drive a Micromaser charged by incoherent ancillae to steady states which are not pure nor stable with respect to coupling deviations. It is worth observing that the asymptotic value of the purity is in agreement with the theoretical prediction of Eq. (3.1.15), namely $P \approx 1 - 2q = 0.5$ for $q = 0.25$. We can thus conclude that the incoherent charging protocol do not allow the coupling to slightly move away from fine-tuned values.

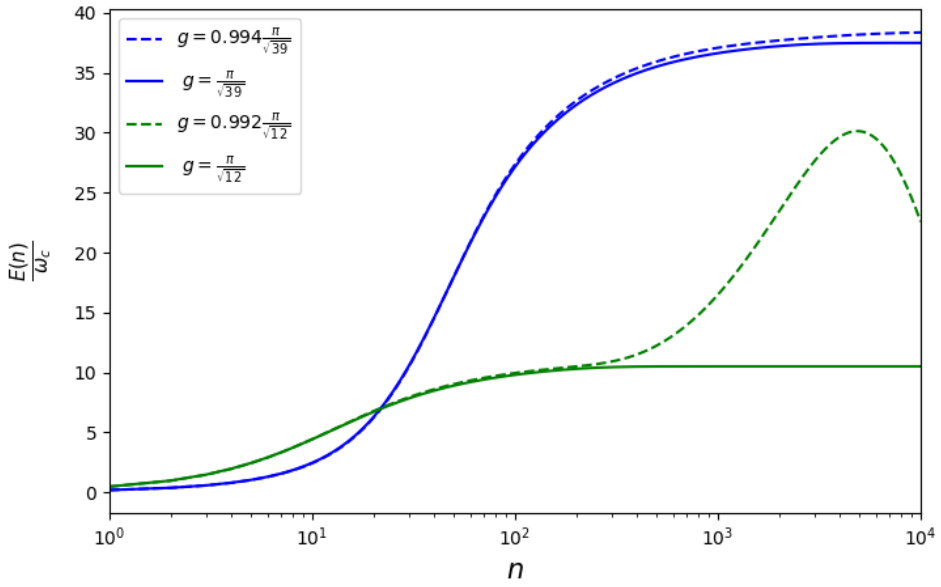

Figure 3.2: Energy stored in the Micromaser as a function of the number of collision model steps n (in units of the Micromaser frequency ω_c) assuming $q = 0.25$, $c = 0$: comparison between $g = \frac{\pi}{\sqrt{12}}$ (fine-tuned, solid), $g = 0.992\frac{\pi}{\sqrt{12}}$ (non fine-tuned, dashed) and $g = \frac{\pi}{\sqrt{39}}$ (fine-tuned, solid), $g = 0.994\frac{\pi}{\sqrt{39}}$ (non fine-tuned, dashed).

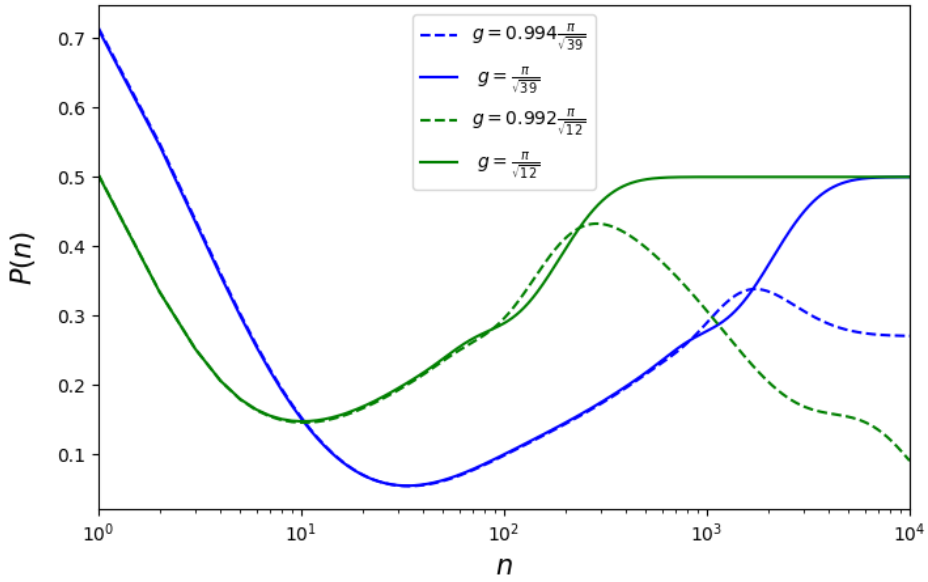

Figure 3.3: Purity of the Micromaser state as a function of the number of collision model steps n assuming $q = 0.25$, $c = 0$: comparison between $g = \frac{\pi}{\sqrt{12}}$ (fine-tuned, solid), $g = 0.992\frac{\pi}{\sqrt{12}}$ (non fine-tuned, dashed) and $g = \frac{\pi}{\sqrt{39}}$ (fine-tuned, solid) $g = 0.994\frac{\pi}{\sqrt{39}}$ (non fine-tuned, dashed).

3.2.2 Effects of increasing quantum coherences

The theoretical description of the Micromaser dynamics performed in Sec 3.1 suggests that adding quantum coherences to ancillae density matrices could cause:

- smaller values of stored energy, due to cotangent factors in the evolved steady state populations as expressed in Eq. (3.1.22);
- better performances in terms of purity (and ergotropy) of the evolved Micromaser state, also for $q \neq 0$.

As anticipated, these points have already been discussed in [33, 32], both analytically and numerically, for the $c = 1$ case. Here, we will increase quantum coherences, exploring intermediate regimes which have not yet been considered in literature. Eventually, we will also show results for the fully-coherent protocol.
We will analyze the effects of the presence of quantum coherences comparing both the stored energy and purity of the Micromaser for only two values of the coupling, namely $g_{ft} = \frac{\pi}{\sqrt{12}}$ and $g_{nft} = 0.992\frac{\pi}{\sqrt{12}}$, and studying the collision model behaviour varying c.
At first we analyze the stored energy, shown in Fig. 3.4. It can be easily observed that relevant differences between the fine-tuned and non fine-tuned protocols still arise if c remains below $c = 0.5$. In this regime, the non fine-tuned protocols are not suitable for the realization of a quantum battery, since stored energy does not reach a stable value but indefinitely increases. This is an undesired feature when studying the Micromaser, since it drives the system to high energy states where anharmonicity effects may emerge. Effects of the presence of anharmonicity on the battery performances are postponed to Chapter 4.
It is worth observing, however, that the accordance between fine-tuned and non fine-tuned protocols increases by increasing quantum coherences. For what concerns purity, we still

expect a similar drift in the non fine-tuned case below $c = 0.5$.

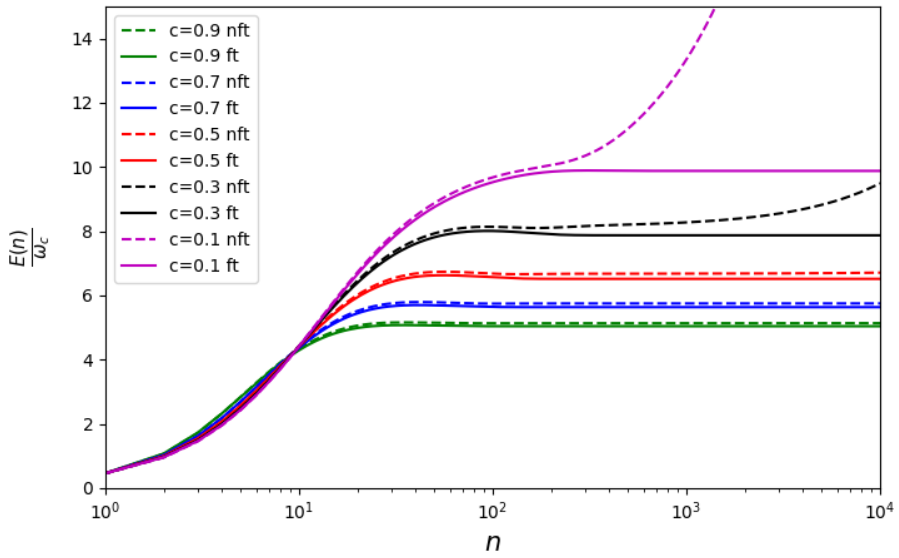

Figure 3.4: Energy stored in the Micromaser as a function of the number of collision model steps n (in units of the Micromaser frequency ω_c). For each value of c (see legend for more details) we compare $g = \frac{\pi}{\sqrt{12}}$ (fine-tuned, solid) and $g = 0.992\frac{\pi}{\sqrt{12}}$ (non fine-tuned, dashed) assuming $q = 0.25$.

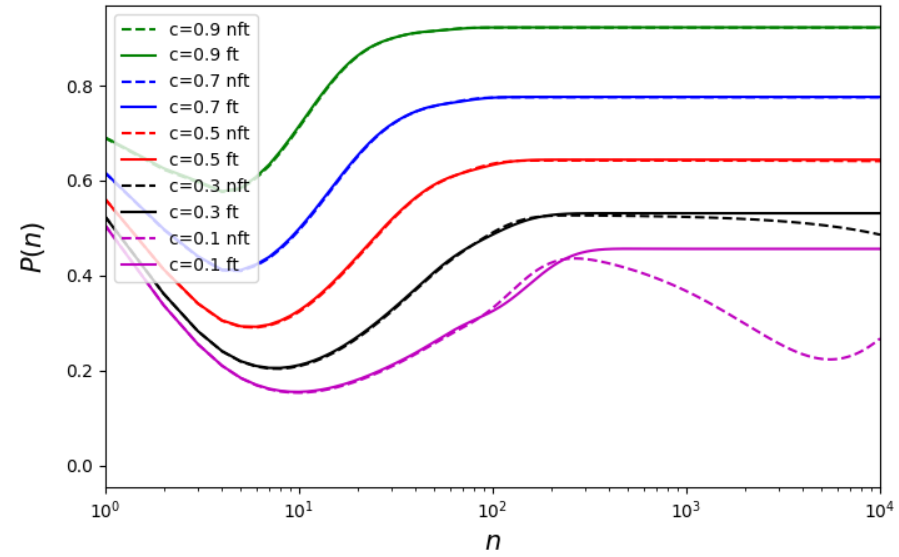

Figure 3.5: Purity of the Micromaser state as a function of the number of collision model steps n. For each value of c (see legend for more details) we compare $g = \frac{\pi}{\sqrt{12}}$ (fine-tuned, solid) and $g = 0.992\frac{\pi}{\sqrt{12}}$ (non fine-tuned, dashed) assuming $q = 0.25$.

Numerical results for purity are shown in Fig. 3.5. and confirm what we expected, since they show: the progressive stabilization of results with respect to slight deviations from fine-tuned values, but only for $c > 0.5$; an increasing steady state purity in correspondence with the increasing of coherences. Since simulations of intermediate regimes

suggest that moving towards the fully-coherent protocol could lead to stabilization with respect to slight deviations from fine-tune couplings we now try to investigate this regime. In Sec. 3.1 we stated that the coherent charging protocol of a Micromaser drives the system towards an almost pure and excited steady state. The striking feature of a coherent charging protocol, pointed out for the first time in [33], is that the same performances in terms of energy and purity of the steady state can be reached also if the coupling is not perfectly fine-tuned. In this case, in fact, it was shown that although the trapping condition is slightly broken, the breaking is not relevant enough to modify the stored energy and purity of the battery with respect to the one obtained in the fine-tuned case. For all simulations of the coherent protocol we will assume $c = 1$ and $q = 0.25$ independently from the pair considered. We start the comparison between the fine-tuned and non fine-tuned case by showing the breaking of the trapping condition caused by non fine-tuned values of the coupling. We observe that, in the fine tuned case (Fig. 3.6(a)) the evolved Micromaser density matrix is populated only within a block of size $l = 11$. This is what we expected since, as explained in Section 3.1.2, choosing $g_{ft} = \frac{\pi}{\sqrt{12}}$ leads to the separation of the state space of the Micromaser into two dynamically disconnected blocks, one formed by Micromaser states $|k\rangle$ with $k < 12$ and another with the remaining states. Thus, initializing the system in the first block (Eq. (3.2.1)) constrains the dynamics in the trap shown in Fig. 3.6(a). On the other hand, Fig. 3.6(b) shows, for $g = 0.992\frac{\pi}{\sqrt{12}}$, a slight breaking of the perfectly trapped dynamics of the fine-tuned case. It is worth noting, however, that the vast majority of the populations remain localized in the same block of the fine-tuned case, while a very small portion of spectral density "leaks" into a region at higher Micromaser states.

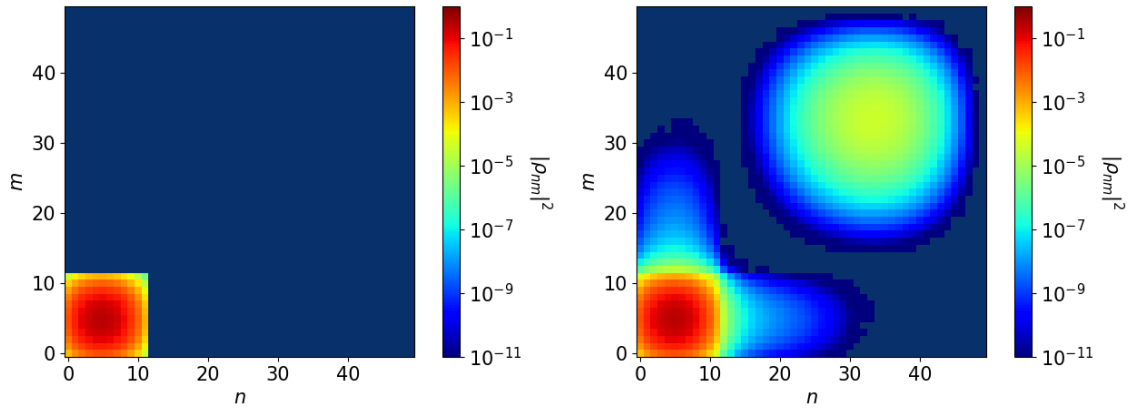

(a) $g = \frac{\pi}{\sqrt{12}}$ (b) $g = 0.992\frac{\pi}{\sqrt{12}}$

Figure 3.6: Density plot showing the absolute values of Micromaser density matrix elements after 10000 collisions of a JC collision model for $q = 0.25$, $c = 1$, $\Delta t = 1$. Comparison between (a) $g = \frac{\pi}{\sqrt{12}}$ (fine-tuned) and (b) $g = 0.992\frac{\pi}{\sqrt{12}}$ (non fine-tuned).

The trapping dynamics has interesting consequences in terms of the energy stored in the battery and its purity. We start discussing this point by analyzing the stored energy, which is shown as a function of the number n of completed steps of the collision model in Fig. 3.7 for different values of g.
Comparing results for fine-tuned values of the coupling (continuous curves) with non-fine

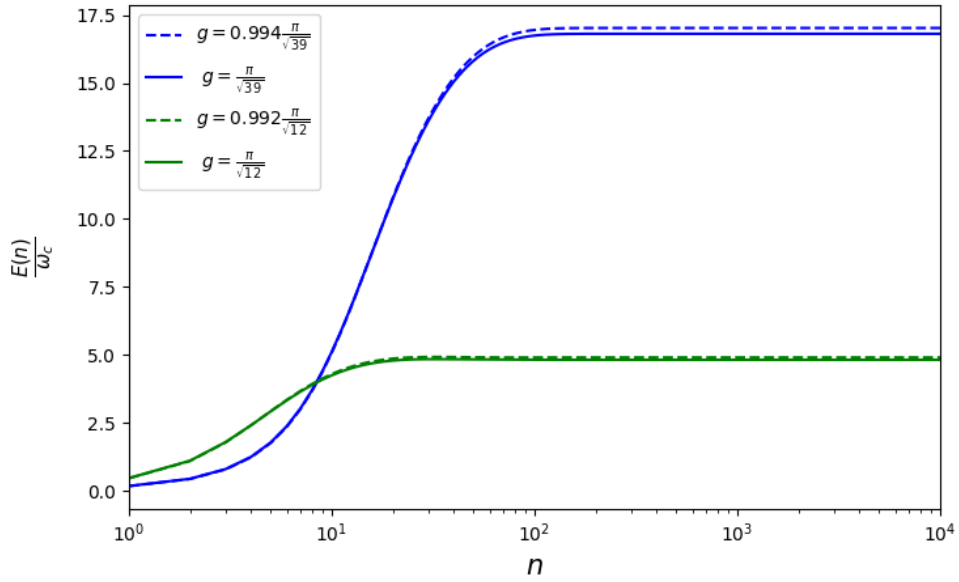

Figure 3.7: Energy stored in the Micromaser as a function of the number of collision model steps n (in units of the Micromaser frequency ω_c) assuming $q = 0.25$, $c = 1$: comparison between $g = \frac{\pi}{\sqrt{12}}$ (fine-tuned, solid), $g = 0.992\frac{\pi}{\sqrt{12}}$ (non fine-tuned, dashed) and $g = \frac{\pi}{\sqrt{39}}$ (fine-tuned, solid), $g = 0.994\frac{\pi}{\sqrt{39}}$ (non fine-tuned, dashed).

tuned values results (dashed curves), the most striking feature to observe is that there is no relevant difference in terms of stored energy, as pointed out in [33]. This is a direct consequence of what observed in Fig. 3.6(b) about populations of the density matrix: relevant populations remain localized in the original trap, whereas populations arising out of this block reveal to be negligible.
Another interesting aspect emerges if one confronts two different fine-tuned values: the smaller one drives the system towards an higher stored energy. This is not surprising since, as seen both analytically (Section 3.1.2) and numerically (Fig. 3.6), the fine-tuned coupling and the size of the trapping block are inversely proportional. Two other interesting features emerge from these figures. The first is the fact that the coherent protocol reveals to be faster at reaching stability. Indeed, the incoherent one, which we analyzed in Sec. 3.2.1 took hundreds of collision in order to reach stable values of energy and purity, whereas the coherent protocol analyzed here takes tens, one hundred at most. Secondly, the steady state energy results to be smaller than the one obtained in the incoherent case. This is in agreement with what seen at the end of Sec. 3.1.2, where we anticipated the fact that cotangent factors appearing in the coherent case steady state populations suppress high energy populations.

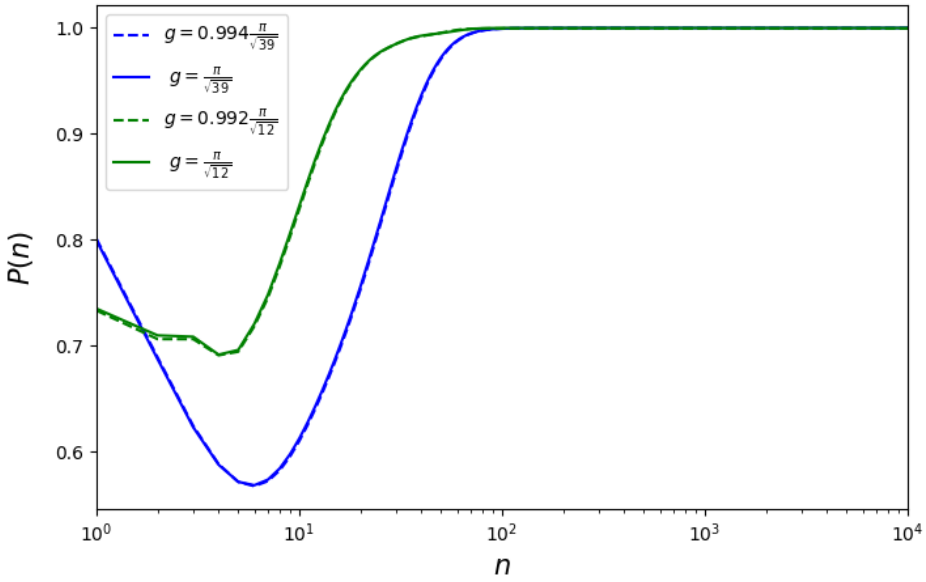

Figure 3.8: Purity of the Micromaser state as a function of the number of collision model steps assuming $q = 0.25$, $c = 1$: comparison between $g = \frac{\pi}{\sqrt{12}}$ (fine-tuned, solid), $g = 0.992\frac{\pi}{\sqrt{12}}$ (non fine-tuned, dashed) and $g = \frac{\pi}{\sqrt{39}}$ (fine-tuned, solid) $g = 0.994\frac{\pi}{\sqrt{39}}$ (non fine-tuned, dashed).

The absence of relevant differences between fine-tuned and non fine-tuned protocols in the coherent case can be noticed also by studying the purity of the Micromaser state, which we show in Fig. 3.8 as a function of the number n of completed steps of the collision model. As anticipated, the difference, in terms of purity, between fine-tuned and non fine-tuned case is almost imperceptible, and in both cases the evolved state of the Micromaser is approximately pure already after one hundred collisions, in accordance with results shown in [33]. This implies that the amount of extractable work from the battery is maximized in both cases.

To summarize, in this Section we showed numerical results for the stored energy and purity of a Micromaser quantum battery in presence of increasing coherences of the ancillae, until reaching the fully-coherent regime, whose results are in agreement with those shown in [33] and with the theoretical description carried out in Sec. 3.1.2.

3.2.3 Beyond the JC model

We have already mentioned that the possibility to extend the RWA, leading to JC Hamiltonian, towards the USC regime can be achieved by performing a proper external modulation of qubit and cavity frequencies [71]. Nonetheless, it is important to analyze the stability of the properties discussed above also in presence of counter rotating terms, in absence of modulation. Thus, we studied again the Micromaser time evolution in the interaction picture, this time without performing RWA, with the system-ancilla interaction Hamiltonian given by the following expression defined in Eq. (2.2.12)

$$\tilde{V}_{Sn} = g\big(a^\dagger\sigma_+ e^{2i\omega_c t} + a^\dagger\sigma_- + a\sigma_+ + a^\dagger\sigma_+ e^{-2i\omega_c t}\big). \tag{3.2.4}$$

If, in previous Sections, we were able to obtain an analytical expression for the quantum map, this is not the case for the collision model employing $\tilde{V}_{Sn}$ in Eq. (3.2.4), due to the

presence of counter rotating terms. For this reason, simulations in the presence of counter rotating terms must be performed by using a full numerical approach which carries out every system-ancilla interaction in an approximated way. The solver we used in our implementation is QuTiP *mesolve*. Further details on the implemented code can be found in Appendix.
The most important thing to underline before proceeding further is that we have checked that employing this solver with a Jaynes-Cummings Hamiltonian leads to the same results obtained throughout the previous Sections of this Chapter, where we performed numerical computation of the exact quantum map in Eq. (3.1.1) without relying on approximated methods. In Fig. 3.9 we show the comparison between results obtained in the regimes $\frac{g}{\omega_c} = 0.1$ and $\frac{g}{\omega_c} > 0.1$.

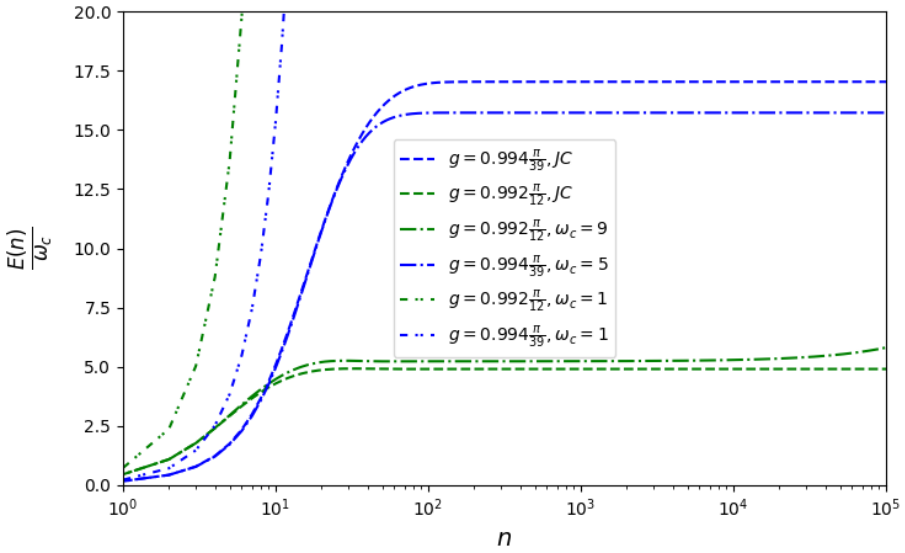

Figure 3.9: Energy stored in the Micromaser as a function of the number of collision model steps (in units of the Micromaser frequency ω_c) assuming $q = 0.25$, $c = 1$: comparison between JC evolution and complete interaction evolution for different values of g and $\frac{g}{\omega_c}$, with g chosen as a non fine-tuned value (for the coherent protocol there is no relevant difference between fine-tuned and non fine-tuned values).

We see that for $\frac{g}{\omega_c} > 0.1$ all typical features of the dynamics in the JC regime are lost. On the other hand, if $\frac{g}{\omega_c} = 0.1$, we see that the presence of qualitative differences between JC and complete dynamics crucially depends on the value of g: if $g = 0.994\frac{\pi}{39}$, the presence of counter rotating terms cause a deviation from JC dynamics, which appears after 10^4 collisions, whereas if $g = 0.992\frac{\pi}{12}$ (blue lines), there is no qualitative difference on the dynamics, but only a quantitative one at the level of the stored energy. We also analyzed values of $\frac{g}{\omega_c}$ below 0.1, showing that no relevant differences due to counter rotating terms emerges below 0.05, confirming the results claimed in [33]. Thus, we conclude that the RWA leads to reliable results only if $\frac{g}{\omega_c} < 0.1$.
While below $\frac{g}{\omega_c} = 0.05$ it coincides with the full interaction dynamics, the interval $0.05 \leq \frac{g}{\omega_c} \leq 0.1$ is more insidious, since the RWA validity depends also on the value of g.

3.3 Conclusions

Comparing numerical results shown in the second Section of this Chapter with the theoretical treatment of Sec. 3.1, we can conclude that they are in agreement and can be summarized in the following steps:

- **coherent charging protocol** stabilizes the charging of the battery with respect to coupling deviations from fine-tuned values and allows the creation of almost pure steady state independently from the populations q of the ancillae involved in the charging;
- **incoherent charging protocol** exhibits instability with respect to the above coupling deviations, although being more effective in the fine-tuned case, where it is able to store a greater amount of energy.

Furthermore, numerical results exhibit stability with respect to the introduction of counter rotating terms which we neglected in the simulations performed to obtain the above results, provided that we limit ourselves to regimes where $\frac{g}{\omega_c} < 0.1$.

Chapter 4

The transmon as a quantum battery: anharmonicity at work

In this Chapter we present original results concerning the collisional charging of a transmon quantum battery, together with a discussion on the extractable energy once the charging is complete. Using a transmon platform provides us with a multi-level structure which, compared to harmonic batteries, allows us to study the effects of anharmonicity on the battery charging.
After introducing the collisional model for the transmon in Sec. 4.1, we discuss in Sec. 4.2 the most subtle numerical issues for simulating this kind of model. Finally, in Sec. 4.3, we show original results for the transmon stored energy, purity and ergotropy, comparing the coherent and incoherent charging protocols.

4.1 Collision model set up

The collisional model we are going to study consists in a transmon battery S which sequentially interacts with a set of chargers modeled as two-level systems (ancillae). As done in previous Chapters, we will focus on Markovian processes, assuming these charging units to be non interacting and initially uncorrelated, together with the assumption that each of them interacts only once with the system (see Sec. 2.2.1). We will denote with $\{\hat{\eta}_n\}$, $n \in \mathbb{N}$, the set of density matrices describing the ancillae and with $\hat{\rho}_S(n)$ the battery reduced density matrix after the interaction with n ancillae. As anticipated in Sec. 2.2.1, the evolution of the system is determined step by step by a quantum map

$$\hat{\rho}_S(n) = M_n[\hat{\rho}_S(n-1)] \quad (\text{with} \quad n \geq 1) \tag{4.1.1}$$

which allows to compute the density matrix at the end of the n–th step starting from the one at the end of the previous one. Such dynamics can be determined once the Hamiltonian of the n–th step and an initial condition have been specified. To this end, as done before in Chapter 3, we will employ the same initial condition for each ancilla as used for the Micromaser (see Eq. (2.2.27)), namely

$$\hat{\eta}_n = q\,|-\rangle\langle-|_n + (1-q)\,|+\rangle\langle+|_n + c\sqrt{q(1-q)}(|-\rangle\langle+|_n + |+\rangle\langle-|_n), \tag{4.1.2}$$

with c and q respectively their degree of coherence and ground state population. In order to guarantee the homogeneity of the collision model, also the Hamiltonian must be

independent from the step considered. According to this we will assume it of the form

$$\hat{H}(t) = \hat{H}_S + \hat{H}_n + \hat{V}_{S,n} \tag{4.1.3}$$

with

$$\hat{H}_S = 4E_C(\hat{N} - N_g)^2 - E_J\mathrm{Cos}(\hat{\varphi}) \tag{4.1.4}$$

$$\hat{H}_n = \frac{\Delta}{2}\hat{\sigma}_{z,n} \tag{4.1.5}$$

$$\hat{V}_{S,n} = g\hat{N}(\hat{\sigma}_{+,n} + \hat{\sigma}_{-,n}) \tag{4.1.6}$$

which respectively represent the transmon free Hamiltonian derived in Sec. 1.3.3, the n–th ancilla free Hamiltonian and the corresponding interaction term. The latter can be realized by capacitively coupling two superconducting circuits in the transmon regime [44], with the one playing the role of the ancilla described as a TLS. This is accurate provided that its anharmonicity is sufficiently high to allow to choose two of its eigenstates as these of an effective TLS, essentially decoupled from the others.
No parameter depends from the step index n, as required before. For what concerns the initial condition of the battery, we will assume it to be starting in its ground state.
Differently from what done in Sec. 2.2.2, the quantum map associated to the Hamiltonian in Eq. (4.1.3) cannot be solved exactly. To proceed, we thus employ a numerical approach. See Sec. 4.2 for details.

4.1.1 Free transmon Hamiltonian

In order to have a better insight on the physics of the transmon, we present here some features obtained with the approximated approach introduced in Sec. 1.3.3 for the transmon limit $E_J \gg E_C$ of the Hamiltonian in Eq. (4.1.4). This reveals to be useful to choose suitable parameters for the numerical simulations, which, however, will be carried out using the non-approximated Hamiltonian of Eq. (4.1.4). To this end, we rewrite it in terms of its eigenvalues and eigenvectors

$$\hat{H}_S = \sum_{m=0}^{+\infty} E_m \left|E_m\right\rangle\!\left\langle E_m\right| \tag{4.1.7}$$

where E_m can be approximated, in the transmon limit $E_J \gg E_C$, by Eq. (1.3.66) as

$$E_m \approx (\omega_p - E_C)m - \frac{1}{2}E_C m(m-1) \tag{4.1.8}$$

with $\omega_p = \sqrt{8E_J E_C}$. This implies that the energy gap between two levels is smaller than the preceding energy gap by a quantity E_C (see Sec. 1.3.3). This leads to a relative anharmonicity of the system given by Eq. (1.3.68) as

$$\alpha_r \approx \frac{E_C}{\omega_p - E_C} \approx \sqrt{\frac{E_C}{8E_J}}. \tag{4.1.9}$$

The ratio E_J/E_C also determines the number N_b^{th} of bound eigenstates within the cosine well in Eq. (4.1.4), namely states with $|E_m| < E_J$. Since this is a finite well it allows, in fact, only a finite number of bound states, which are localized in the φ coordinate.

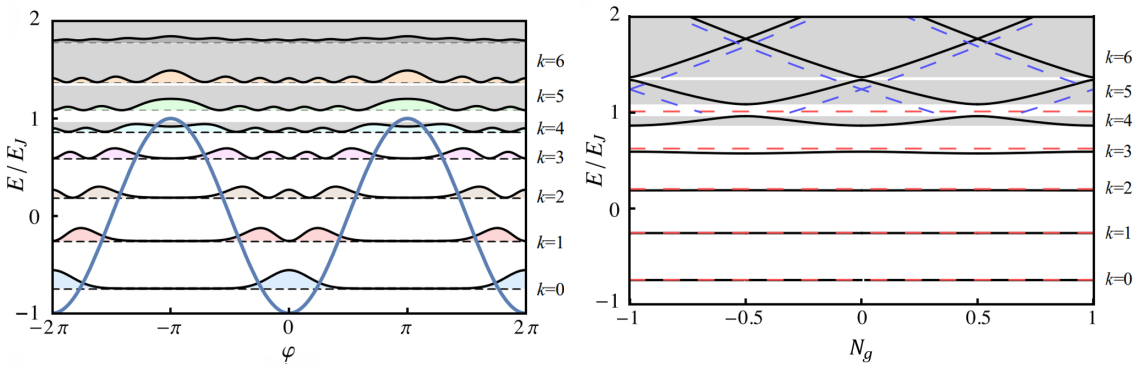

Figure 4.1: (a) Eigenvalues E_k of the transmon for $E_J/E_C = 30$ as functions of φ in units of E_J (black dotted lines). On top of each line, the absolute square of the corresponding Mathieu eigenfunction is shown (see Sec. 1.3.3). The blue line represents the cosine well. The energy bands from (b) are reported with gray. (b) Eigenvalues E_k of the transmon for $E_J/E_C = 30$ as functions of N_g in units of E_J (black solid lines) compared with the duffing oscillator levels (dashed red) and the $E_J = 0$ levels (dashed blue). The charge dispersion of the highest levels leads to energy bands denoted with grey. Image taken from [63].

Outside the well, on the contrary, states are no more localized in the φ coordinate as shown in Fig. 4.1(a).
This figure confirms what anticipated in Sec. 1.3.3 for the flattening of the transmon eigenvalues. However, it also shows that when the eigenvalues exceed the well they become sensitive to N_g variations, leading to a band-like energy structure (see Fig. 4.1(b)).
The number of bound states N_b^{th} can be estimated by requiring $E_{N_b^{th}-1} \approx E_J$ leading to [63]

$$N_b^{th} \approx \sqrt{\frac{E_J}{E_C}}. \tag{4.1.10}$$

The apex th (theoretical) is used to distinguish this value, estimated within the transmon approximation, by the effective number of bound states N_b which emerges from simulations, which will be discussed in Sec. 4.2.1 .
As we will see, the effective number of bound states N_b is usually smaller than this prediction. Eq. (4.1.10), however, allows us to adopt a guideline in choosing the values of E_J and E_C in our simulations: in order to have a significant number of trapped and charge-insensitive states we must choose $E_J/E_C \gg 1$ but, at the same time, exceeding in this direction would imply too small anharmonicities (see Eq. (4.1.9)), whose effects are the object of this thesis. Thus, always remaining in the transmon working regime $20 \lesssim E_J/E_C \ll 5 \times 10^4$ (see Sec. 1.3.3), these two aspects need to be balanced.

4.1.2 Transmon-ancilla interaction

For numerical convenience, the simulations of the transmon battery will be carried out in the interaction picture. To proceed further, it is useful to rewrite Eq. (4.1.6) in terms of

the free Hamiltonian eigenvectors as

$$\hat{V}_{S,n} = g\left(\sum_{m,l=0}^{+\infty} N_{lm} \left|E_l\right\rangle\!\left\langle E_m\right|\right)(\hat{\sigma}_{+,n} + \hat{\sigma}_{-,n}) \tag{4.1.11}$$

with

$$N_{lm} = \langle E_l|\hat{N}|E_m\rangle\,. \tag{4.1.12}$$

This simplifies the interaction picture expression $\tilde{V}_{S,n}$ for the coupling Hamiltonian since

$$\left|\tilde{E}_m\right\rangle = e^{i\hat{H}_S t}\left|E_m\right\rangle = e^{iE_m t}\left|E_m\right\rangle \tag{4.1.13}$$

so that

$$\begin{aligned}
\tilde{V}_{S,n} &= g\left(\sum_{m,l=0}^{+\infty} N_{lm} e^{i(E_l - E_m)t}\left|E_l\right\rangle\!\left\langle E_m\right|\right)\left(\hat{\sigma}_{+,n}e^{i\Delta t} + \hat{\sigma}_{-,n}e^{-i\Delta t}\right) = \\
&= g\left(\sum_{m,l:l\geq m}^{+\infty} N_{lm} e^{i(\delta E_{l,m}+\Delta)t}\left|E_l\right\rangle\!\left\langle E_m\right|\hat{\sigma}_{+,n} + \sum_{m,l:l\geq m}^{+\infty} N_{lm} e^{i(\delta E_{l,m}-\Delta)t}\left|E_l\right\rangle\!\left\langle E_m\right|\hat{\sigma}_{-,n}\right) + \\
&+ g\left(\sum_{m,l:l<m}^{+\infty} N_{lm} e^{i(-\delta E_{m,l}+\Delta)t}\left|E_l\right\rangle\!\left\langle E_m\right|\hat{\sigma}_{+,n} + \sum_{m,l:l<m}^{+\infty} N_{lm} e^{i(-\delta E_{m,l}-\Delta)t}\left|E_l\right\rangle\!\left\langle E_m\right|\hat{\sigma}_{-,n}\right)
\end{aligned} \tag{4.1.14}$$

where we have defined

$$\delta E_{l,m} = E_l - E_m. \tag{4.1.15}$$

Provided that $N_{lm} \neq 0$, the corresponding projector in Eq. (4.1.14) causes a jump from the level m to the level l of the transmon. In analogy with the approach used for the oscillating terms in the oscillator-ancilla interaction Hamiltonian considered in the Micromaser case (see Sec. 2.2.2 and Chapter 3), we can perform the rotating wave approximation neglecting fastly oscillating terms in the weak coupling regime. There is, however, a fundamental difference between this case and the oscillator-TLS one: here, anharmonicity causes the presence of many different transition frequencies $\delta E_{l,m}$ whereas, in the latter case, there is only one frequency associated to the system. This fact forces us to carefully reconsider the weak coupling regime to determine terms that can be neglected. Numerical issues on this point are discussed in Sec. 4.2.2.

4.2 Numerical details

Once the theoretical model has been introduced, we now focus on the numerical aspects. While performing calculations, we dealt with two main problems:

- The stability of results with respect to the type and size of the basis used to represent quantum operators;
- The presence of the counter rotating terms discussed in Sec. 4.1.2, which cause the simulations to be highly time-consuming.

In the following we will discuss the solutions adopted to overcome these issues. Further details on the code layout are shown in the Appendix.

4.2.1 Stabilization of the transmon eigenproblem

To numerically evaluate the eigenvalues and eigenvectors of the transmon battery, one needs to choose a basis over which the system is represented in order to perform calculations. To this end, we explored two possibilities:

- The eigenbasis of a harmonic oscillator. This choice is consistent with the idea that the transmon Hamiltonian can be approximated by a Duffing oscillator $\hat{H}_{tr} \approx 4E_C\hat{N}^2 + \frac{E_J\hat{\varphi}^2}{2} - \frac{E_J\hat{\varphi}^4}{24}$ (see Sec. 1.3.3);
- The eigenbasis of the operator $\hat{N}$ appearing in the transmon Hamiltonian.

The eigenbasis of $\hat{N}$ revealed to be the most suitable. Another important aspect is that, as for the harmonic oscillator, the transmon is a infinite dimensional system and its Hilbert space needs to be truncated to a finite numerical size D. The optimal numerical basis and D must be chosen in order to obtain:

- Bound states which are stable with respect to variations of D;
- Optimization of execution times of the single transmon-ancilla interaction.

In order to determine the best D we required that the number of stable eigenvalues $N_{st}(D)$ with respect to variations of D satisfied the following condition

$$N_b < N_{st}(D). \tag{4.2.1}$$

In order to estimate $N_{st}(D)$, we started from a given numerical size D and, after fixing E_C and E_J, we diagonalized the transmon Hamiltonian of Eq. (4.1.4). Then, we increased D by five units, diagonalized again the transmon Hamiltonian and deemed stable eigenvalues as those with a relative energy variation smaller than 10% . We repeated this procedure until satisfying Eq. (4.2.1).

$\alpha_r/10^{-3}$	D	N_b^{th}	N_b	$N_{st}(D)$
5.9	91	60	54	67
6.9	81	50	46	47
8.8	61	40	36	45
10.2	51	34	31	35
11.8	41	30	27	32

Table 4.1: Study of the stability of the exact diagonalization for each value of the anharmonicity α_r considered in this thesis. N_b^{th} is the estimated number of bound states, whereas N_b is the effective number of bound states emerging from simulations. $N_{st}(D)$ is the number of stable eigenvalues varying the numerical size D.

Table 4.1 shows results for the stability analysis for all the considered values of anharmonicity. As anticipated, we observe that N_b, the number of transmon eigenstates with $|E_m| < E_J$, is always smaller compared with the approximated estimate N_b^{th} of Eq. (4.1.10).
Comparing the fourth and fifth column we can observe that all the numerical sizes chosen do guarantee the stability as required by Eq. (4.2.1).

4.2.2 Neglecting counter rotating terms in transmon-ancilla interaction

The expression for the interaction Hamiltonian of Eq. (4.1.14) can be consistently simplified by neglecting counter rotating (CR) terms. This can be done in different ways. The first possibility consists in adapting Δ depending on the considered step: initializing the battery in its ground state, the first ancilla is initialized at $\Delta = E_1 - E_0$, that is, resonant with the energy transition between the excited state and the ground state; then, all oscillating terms are neglected; finally, fine tuning of the system-ancilla interaction duration allows to drive the system to the first excited state. Repeating this procedure n times allows to create a pure state, namely the level $|E_n\rangle$. However, this approach, inspired by what done in [75], requires a great technological effort, since it calls for extremely finely tunable ancillae.
For these reasons, we focused on a second approach where all the ancillae are initialized with the same gap $\Delta = E_1 - E_0$ and a frequency cutoff is introduced in the interaction term. We started from simulations employing the complete $\tilde{V}_{S,n}$ in Eq. (4.1.14) and gradually neglected CR terms with frequencies $\delta E_{l,m} > k\omega_p$, with $k < N_b$. In analogy with the RWA performed to obtain the JC Hamiltonian, we expect the counter rotating terms to be irrelevant in the weak coupling regime, which here we identify as $g \ll \omega_p$ in order to guarantee that $g \ll |\delta E_{l,m}| = |E_l - E_m| \ \forall \ l, m$. Here, $\{E_l\}$ is the numerically exact spectrum of the Hamiltonian in Eq. (4.1.4).
Starting from $k = 30$ and gradually reducing it, we observed that all counter rotating terms with $\delta E_{l,m} > 2\omega_p$ can be safely neglected for all coupling values examined ($0.01 \lesssim g/\omega_p \lesssim 0.03$) without affecting the figures of merit of interest, namely the stored energy and purity as functions of the number of collisional steps. The presence of high frequency terms, in fact, do not cause variations of the above quantities up to numerical accuracy.

4.3 Results

In this section we show results for the collisional charging of a transmon. The regimes of parameters we tested in this work include the values of α_r listed in Tab. 4.1 and weak couplings $0.01 \lesssim \frac{g}{\omega_p} \lesssim 0.03$.
The reason for not choosing smaller coupling values is that they usually require a great number of collisions in order to reach the asymptotic value of the stored energy and long execution times for the numerical calculations, so that we decided to focus on couplings which could guarantee a faster charging. The study of smaller coupling regimes, however, constitutes a possible future development of this work. On the contrary, as I will show in the following, increasing the coupling value drives the system towards stationary states with a small stored energy, in such a way that it progressively goes below a threshold value, chosen as $E \approx 2\Delta$, which make these cases of no interest for our purposes.
Motivated by the results of the previous Chapter, we will mainly focus on the case of coherent ancillae. In particular, we will discuss both the stored energy and purity of the coherent charging protocol (Sec. 4.3.1), the energy extraction processes (Sec. 4.3.2) and finally focus on the effects of removing quantum coherences (Sec. 4.3.3). The results obtained are summarized in Sec. 4.3.4.

4.3.1 Charging the transmon

Here we will show results for:

- the stored energy $E(n)$ as a function of the collision model steps reported either in units of the battery maximum capacity E_{max}, namely the maximum amount of energy which can be stored in the bound states of the system, or in units of E_C, which has been taken equal for all anharmonicities considered;
- the purity of the battery $P(n)$ as a function of the collision model steps, which will be relevant when dicussing the extractability of the stored energy (see Sec. 1.4.3).

The need for the study of $E(n)/E_{max}$ derives from the fact that different values of E_J and E_C, that means, different values of anharmonicities, correspond to different numbers of states trapped in the potential well of the transmon (see Table 4.1) and a different maximal energy E_{max} which can be stored in the battery. Fig. 4.2(a) compares $E(n)/E_{max}$ for different anharmonicities with a fixed coupling $g/\omega_p = 0.01$.

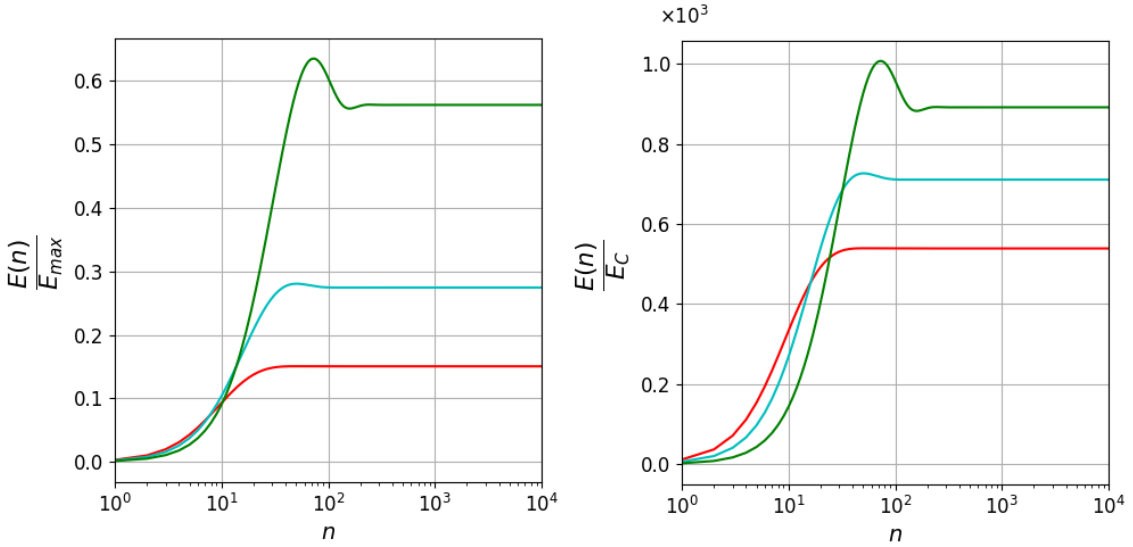

(a) (b)

Figure 4.2: Stored energy in units of E_{max} (panel (a)) and E_C (panel(b)) as a function of the collision model steps n assuming $c = 1$, $q = 0.25$. Comparison between different anharmonicities $\alpha_r = 5.9 \times 10^{-3}$ (red), 6.9×10^{-3} (cyan), 8.8×10^{-3} (green) for $\frac{g}{\omega_p} = 0.01$.

We observe that all α_r values considered allow to store a non negligible energy. The most striking features are: the increasing of $E(n)/E_{max}$ when the anharmonicity is progressively increased; the fact that its stabilization is much slower, namely requires more collisions, for high anharmonicities than for the small ones. The first point does not allow us to conclude that the stored energy increases with the anharmonicity, given the dependence of E_{max} from α_r shown in Fig. 4.3.
If, on the other hand, one is interested in studying the amount of stored energy not caring about the maximum capacity, then results for different values of the anharmonicity can be shown in units of the common energy scale E_C.
This is shown in Fig. 4.2(b). We see that, in this case with $g/\omega_p = 0.01$, the stored energy increases for increasing α_r.

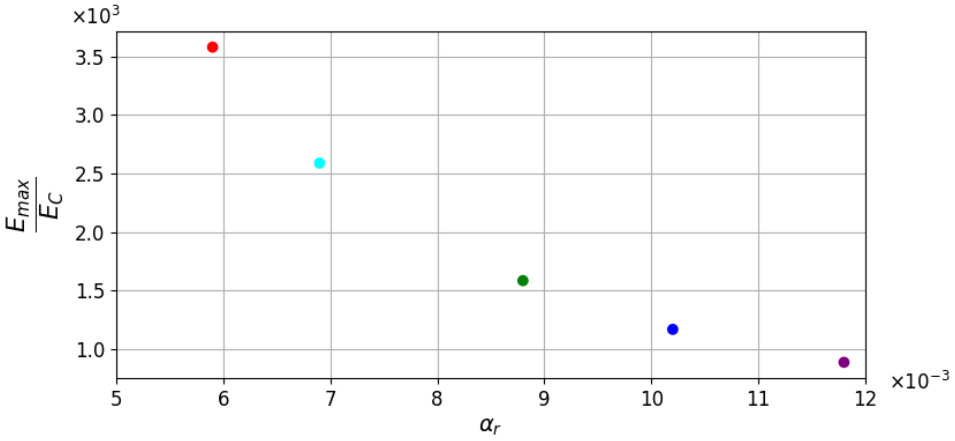

Figure 4.3: Behaviour of E_{max} (in units of the capacitive energy scale E_C) as a function of α_r.

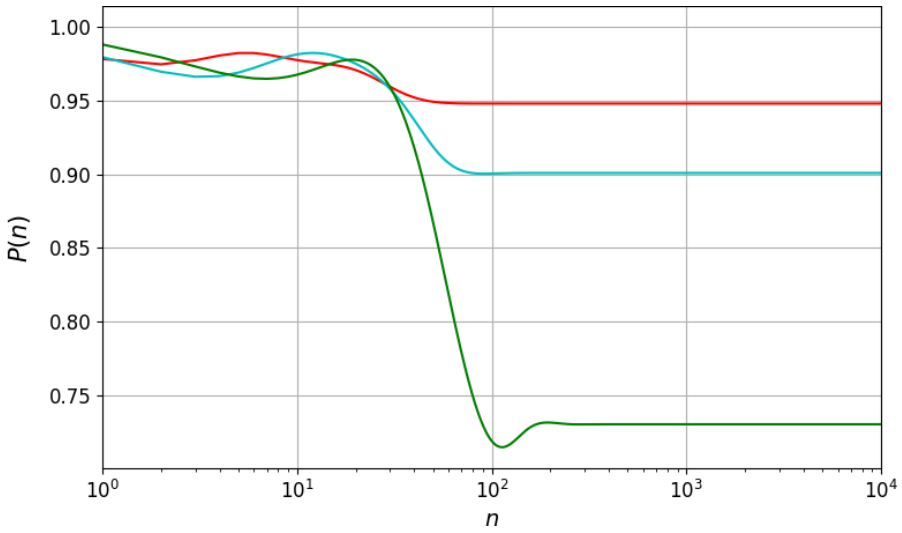

Figure 4.4: Purity of the transmon as a function of the number of collision model steps n assuming $q = 0.25$, $c = 1$. Comparison between different anharmonicities $\alpha_r = 5.9 \times 10^{-3}$ (red), 6.9×10^{-3} (cyan), 8.8×10^{-3} (green) for $\frac{g}{\omega_p} = 0.01$.

Another interesting feature of the coherent collisional charging is the progressive degradation of the purity by increasing α_r, shown in Fig. 4.4. The two smallest anharmonicities considered guarantee a high purity of the evolved steady state, such that $0.9 \lesssim P \lesssim 1$, whereas the highest value presents a smaller P.

One can also analyze what happens when the coupling changes. For this reason, we show the same quantities for the case of a stronger coupling $g/\omega_p = 0.018$ starting from the stored energy, which is shown in Fig. 4.5(a) in units of E_{max}.

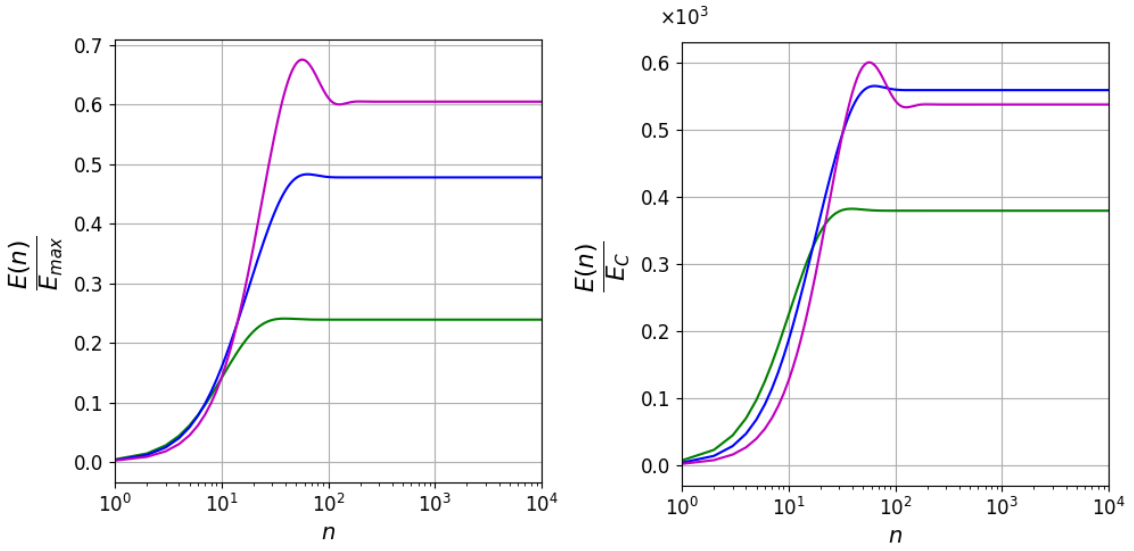

(a) (b)

Figure 4.5: Stored energy in units of E_{max} (panel (a)) and E_C (panel(b)) as a function of the collision model steps n assuming $c = 1$, $q = 0.25$. Comparison between different $\alpha_r = 8.8 \times 10^{-3}$ (green), 10.2×10^{-3} (blue), 11.8×10^{-3} (purple) for $\frac{g}{\omega_p} = 0.018$.

We notice some similarities with the previous case, such as the increasing $E(n)/E_{max}$ and charging time when the anharmonicity is increased. Inspecting $E(n)/E_C$, shown in Fig. 4.5(b), however, exhibits a relevant difference with respect to the case of smaller coupling that was shown in Fig. 4.2(b): the stored energy does not increase for increasing anharmonicities. This confirms that in order to study the stored energy as a function of α_r it is not sufficient to rely on $E(n)/E_{max}$, due to the dependence of E_{max} from α_r, shown in Fig. 4.3.
The purity, shown in Fig. 4.6, has a similar behaviour with respect to the one in Fig. 4.4.

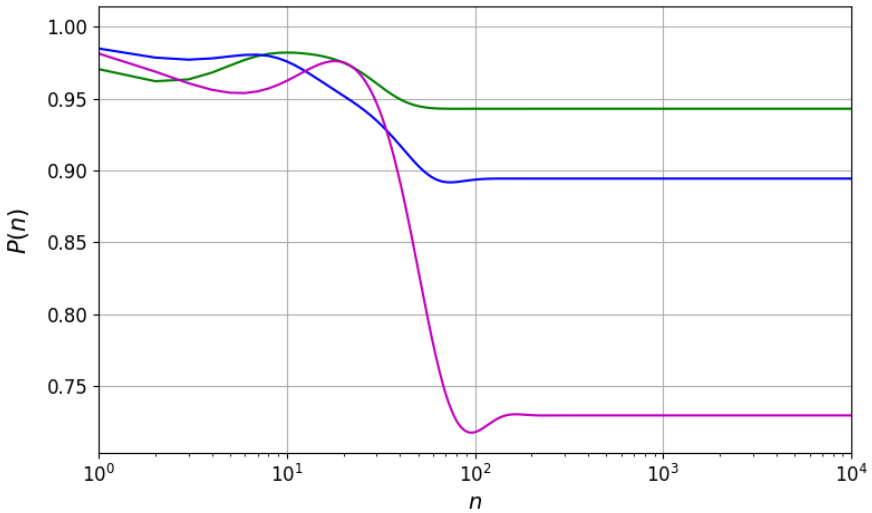

Figure 4.6: Purity of the transmon as a function of the number of collision model steps n assuming $q = 0.25$, $c = 1$. Comparison between different anharmonicities $\alpha_r = 8.8 \times 10^{-3}$ (green), 10.2×10^{-3} (blue), 11.8×10^{-3} (purple) for $\frac{g}{\omega_p} = 0.018$.

The values of α_r discussed in Figs. 4.5 and 4.6 are different from those discussed in Figs. 4.2 and 4.4. The reason for this is that, for fixed α_r, the stored energy decreases with the increasing of the coupling, so that for $\alpha_r = 5.9 \times 10^{-3}$ and $\alpha_r = 6.9 \times 10^{-3}$ the energy stabilizes below $E = 2\Delta$ when g/ω_p is increased up to 0.018. Therefore, these two values loose relevance for the realization of a quantum battery.
To support this last observation we show $E(n)$ in Fig. 4.7 for two different anharmonicities and for different values of the coupling.

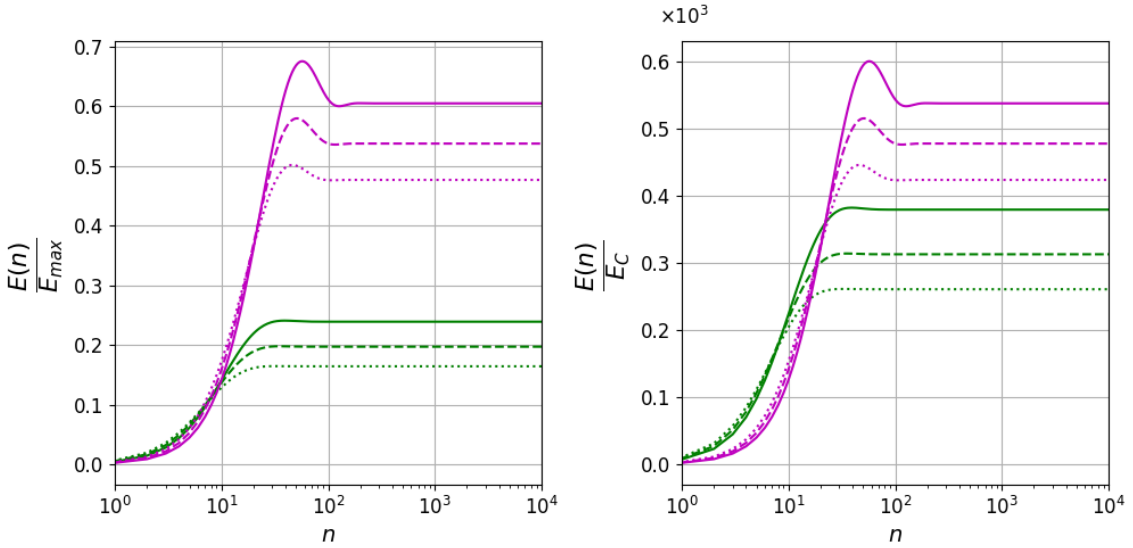

(a) (b)

Figure 4.7: Stored energy in units of E_{max} (panel (a)) and E_C (panel(b)) as a function of the collision model steps n assuming $c = 1$, $q = 0.25$. Comparison between different anharmonicities α_r, namely $\alpha_r = 8.8\times10^{-3}$ (green) and $\alpha_r = 11.8\times10^{-3}$ (purple) for $\frac{g}{\omega_p} = 0.018$ (solid), $\frac{g}{\omega_p} = 0.020$ (dashed) and $\frac{g}{\omega_p} = 0.022$ (dotted).

This shows that, for both the anharmonicities, increasing the coupling causes a decreasing of both $E(n)/E_{max}$ and $E(n)/E_C$ and of the number of collisions needed to reach stability.
Another interesting feature is the presence of peaks of the stored energy before the stabilization: these would represent the best performances obtained with this device, so that it could be relevant and non-trivial to further investigate the charging transient regime, in order to hit the maximum value of the stored energy. This, however, is not an easy task, since one should be able to stop the collisional charging process at the exact number of collisions corresponding to this maximum. Usually, in fact, the user does not know the exact position of this maximum a priori, and may need to be sure of the stabilization before stopping the charging. For these reasons, we focus our attention to properties after the stabilization of the stored energies. A more detailed study of the transient regime, however, provides a natural future development of this work.

To summarize, two different behaviours of $E(n)/E_{max}$ emerge in the asymptotic limit of large n:

- increasing when the anharmonicity is increased at fixed g/ω_p;
- decreasing when the coupling is increased at fixed α_r.

From this point of view, however, the increasing when the anharmonicity is changed from $\alpha_r = 8.8 \times 10^{-3}$ (purple) to $\alpha_r = 11.8 \times 10^{-3}$ (green) is more relevant than the decreasing caused by the coupling variations considered, as clearly emerges from Fig. 4.8.

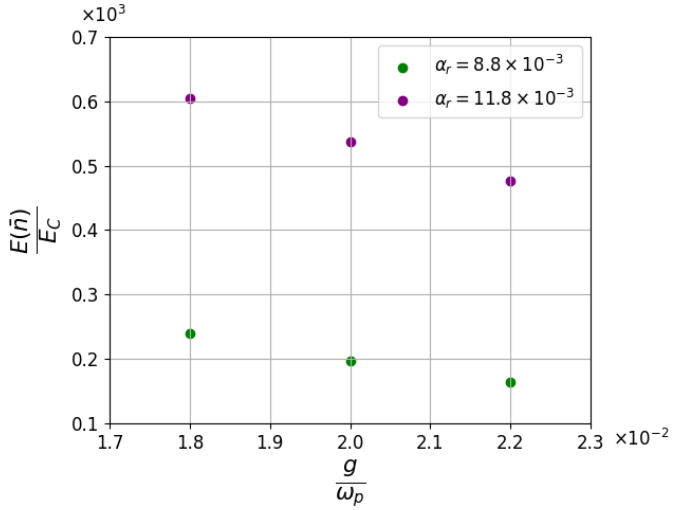

Figure 4.8: Asymptotic stored energy $E(\bar{n})$ in units of E_C as a function of $\frac{g}{\omega_p}$ assuming $c = 1$, $q = 0.25$. Comparison between different anharmonicities $\alpha_r = 8.8 \times 10^{-3}$ (green) and $\alpha_r = 11.8 \times 10^{-3}$ (purple). Here, $\bar{n} = 10000$.

The fact that the stored energy decreases while increasing the coupling occurred also in the case of the Micromaser (see Sec. 3.2). This was ascribable to the fact that increasing the fine-tuned coupling value caused a smaller size of the corresponding trapping state (see Sec. 3.1 and 3.2). The main difference between the Micromaser and the transmon case regards the fact that, while in the former case there is a correspondence between fine-tuned values of the coupling and the size of the trapping states, this structure of fine-tuned values is lost in the latter.
However, it is possible to observe that the evolved stationary states of the transmon take a form which reminds the Micromaser trapping states. Examples for this are shown in Fig. 4.9, where the evolved density matrix $\hat{\rho}_S(\bar{n})$ of the transmon is shown when $\bar{n} = 10000$ for a fixed value of the anharmonicity, namely $\alpha_r = 8.8 \times 10^{-3}$, and for different values of the coupling, in order to show that increasing it from $g/\omega_p = 0.022$ (panel (a)) to $g/\omega_p = 0.028$ (panel (b)) causes the shrinking of the populated region towards lowest energy states. These two values of the coupling have been chosen to magnify the effect. For what concerns the more gradual variations of the coupling considered in Fig. 4.7 we observed this shrinking to be more gradual as well.

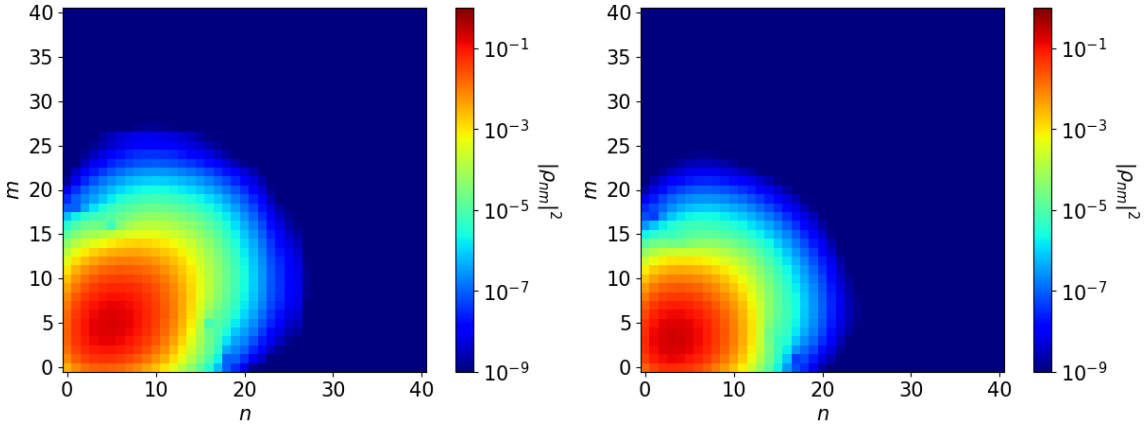

Figure 4.9: Density plots $|\hat{\rho}_S(\bar{n})|^2$ for $\alpha_r = 11.8 \times 10^{-3}$ assuming $c = 1$ and $q = 0.25$. Comparison between: (a) $\frac{g}{\omega_p} = 0.022$ and (b) $\frac{g}{\omega_p} = 0.028$. Here $\bar{n} = 10000$.

On the other hand, another factor that could cause the shrinking of such trap-like states is reducing the anharmonicity with fixed coupling. This is shown in Fig. 4.10 for the same coupling of Fig. 4.9(a) and smaller anharmonicity $\alpha_r = 8.8 \times 10^{-3}$.

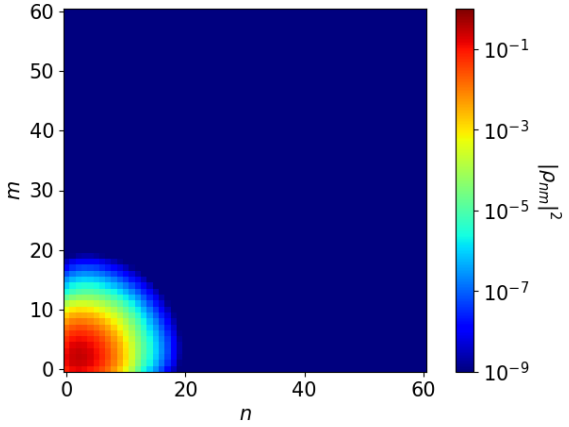

Figure 4.10: Density plot $|\hat{\rho}_S(\bar{n})|^2$ for $\alpha_r = 8.8 \times 10^{-3}$ assuming $c = 1$, $q = 0.25$ and $\frac{g}{\omega_p} = 0.022$. Here $\bar{n} = 10000$.

Comparing Fig. 4.9(a) with Fig. 4.10 highlights that the size of the trap-like state increases with the anharmonicity.
This structure of the evolved density matrix explains the reason behind energy variations discussed above: at high couplings or low anharmonicities the shrinking of the trap-like states causes low stored energies.

For the sake of completeness we analyze the behaviour of the purity of the battery when the coupling is changed. Fig. 4.11 shows the purity for the same couplings and anharmonicities used in Fig. 4.7, confirming that appreciable variations can be seen both by changing the coupling and the anharmonicity: increasing the coupling causes the increasing of the purity of the evolved state whereas increasing the anharmonicity causes an opposite and more evident effect.

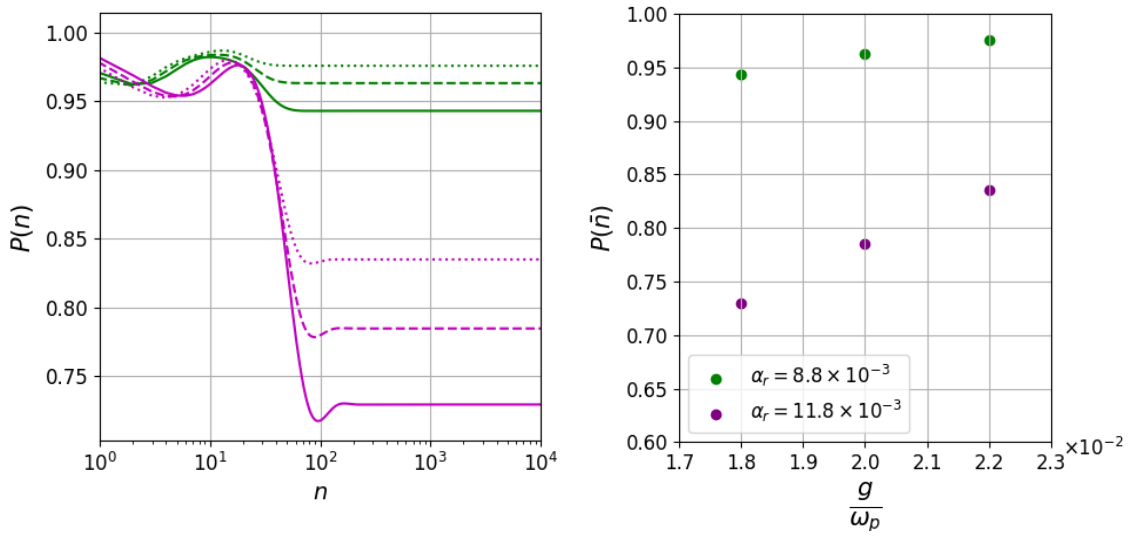

(a) (b)

Figure 4.11: (a) Purity as a function of the collision model steps n assuming $c = 1$, $q = 0.25$. Comparison between different values of α_r, namely $\alpha_r = 8.8 \times 10^{-3}$ (green) and $\alpha_r = 11.8 \times 10^{-3}$ (purple) for $\frac{g}{\omega_p} = 0.018$ (solid), $\frac{g}{\omega_p} = 0.020$ (dashed) and $\frac{g}{\omega_p} = 0.022$ (dotted). (b) Asymptotic purity $P(\bar{n})$ for parameters of panel (a) as a function of $\frac{g}{\omega_p}$, for $\bar{n} = 10000$.

The points discussed until now cannot be extended to arbitrarily high anharmonicities. This is linked to the decreasing of the number of bound states within the well when α_r is increased and to the corresponding increasing of the size of trap-like state, which we pointed out when comparing Fig. 4.9(a) and Fig. 4.10. These two effects cause the saturation of the space of bound states used in simulations, so that relevant populations of the density matrix arise also in states out of the well. Since our purpose is to store energy in the battery by populating its bound excited eigenstates, we focused our analysis on the anharmonicities values shown in Table 4.1 without increasing it further.

4.3.2 Extractable energy

In this section we show results for the ergotropy, which we defined in Sec. 1.4.3 as the maximum amount of unitarily extractable energy. Our purpose here is to study it as a function of the number of completed steps n of the collisional charging, namely to study

$$\mathcal{E}(n) = \mathrm{Tr}_S\left\{\hat{\rho}_S(n)\hat{H}_S\right\} - \min_{\hat{U}\in SU(d)} \mathrm{Tr}_S\left\{\hat{U}\hat{\rho}_S(n)\hat{U}^\dagger\hat{H}_S\right\} \tag{4.3.1}$$

with $n \geq 1$, where $\hat{U}$ is the unitary operator associated to a discharging Hamiltonian (see Sec. 1.4.3). According to the general recipe discussed in Sec. 1.4.3, it is necessary to diagonalize $\tilde{\rho}_S(n)$ in such a way that

$$\tilde{\rho}_S(n) = \sum_{j=1}^{D} p_j(n)\,|p_j(n)\rangle\langle p_j(n)| \tag{4.3.2}$$

at any given step and evaluate the ergotropy as expressed in Eq. (1.4.26)

$$\mathcal{E}(n) = \sum_{j,k=1}^{D} p_j(n) E_k \Big(|\langle p_j(n)|E_k\rangle|^2 - \delta_{j,k} \Big). \tag{4.3.3}$$

Since the purpose of this section is to compare the ergotropy with the stored energy, we will limit to report these quantities in units of E_{max}.
Fig. 4.12(a) shows this comparison for the same anharmonicities shown in Fig. 4.2 for $\frac{g}{\omega_p} = 0.01$, whereas Fig.4.12(b) shows the ratio

$$\xi(n) = \frac{\mathcal{E}(n)}{E(n)} \tag{4.3.4}$$

for the same parameters values.

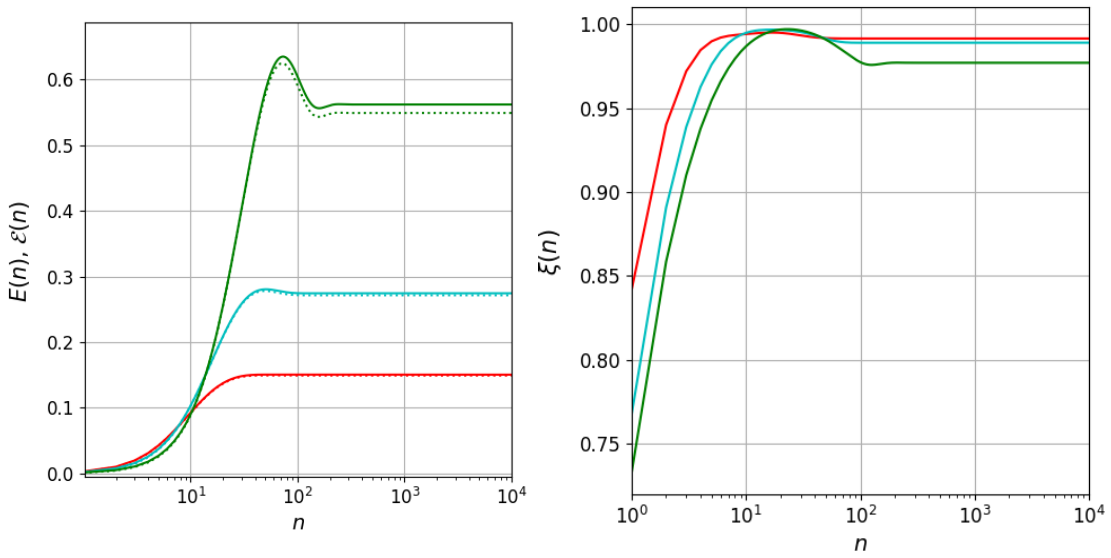

(a) (b)

Figure 4.12: (a) Comparison between the stored energy $E(n)$ (solid) and ergotropy $\mathcal{E}(n)$ (dotted) in units of E_{max} for $\alpha_r = 5.9 \times 10^{-3}$ (red), $\alpha_r = 6.9 \times 10^{-3}$ (cyan), $\alpha_r = 8.8 \times 10^{-3}$ (green). (b) Plots for the ratio $\xi(n)$ for the same anharmonicities. Both are shown as functions of the number of collision model steps n and assuming $q = 0.25$, $c = 1$ and $\frac{g}{\omega_p} = 0.01$.

Interestingly, almost all the stored energy can be extracted through unitary operations on the system. There is, however, an intriguing relationship linking the ergotropy to the purity. To show this, let us compare the results of Fig. 4.12(b) with the purity shown in Fig. 4.4. As can be seen, for $\alpha_r = 5.9 \times 10^{-3}$ and $\alpha_r = 6.9 \times 10^{-3}$ the solid and dotted lines are almost superposed, whereas this is not the case of $\alpha_r = 8.8 \times 10^{-3}$, where the difference between $E(n)$ and $\mathcal{E}(n)$, though not dramatic, is visible. This is linked to the fact, anticipated at the end of Sec. 1.4.3, that ergotropy and purity are related quantities: the value of α_r, among the three considered here, which presents the most evident difference between $E(n)$ and $\mathcal{E}(n)$ is the same which shows the smallest purity in Fig. 4.4. This confirms that the more the state of the battery is pure, the higher is the extractable energy.

These points imply that increasing the anharmonicity causes slightly worse performances in terms of energy extraction, which are however not very relevant given the fact that the fraction of extractable energy is always greater than 95%, as emerges from Fig. 4.12.

A similar behaviour can be found increasing the coupling, as can be seen in Figs. 4.13(a) and (b), which respectively show, for $g/\omega_p = 0.018$, the stored energy together with the ergotropy and $\xi(n)$.

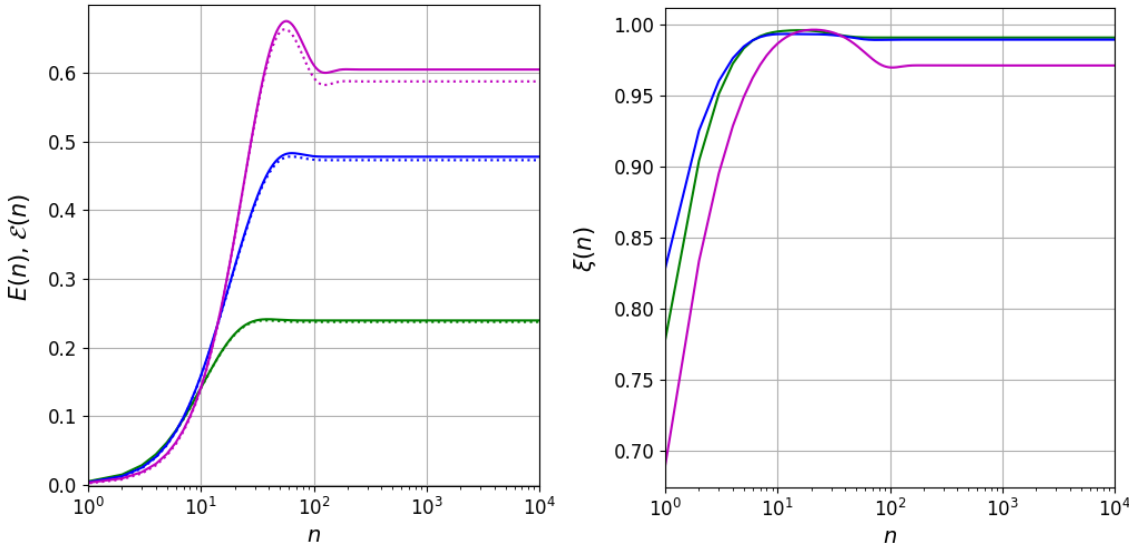

(a) (b)

Figure 4.13: (a) Comparison between the stored energy $E(n)$ (solid) and ergotropy $\mathcal{E}(n)$ (dotted) in units of E_{max} for $\alpha_r = 8.8 \times 10^{-3}$ (green), $\alpha_r = 10.2 \times 10^{-3}$ (blue), $\alpha_r = 11.8 \times 10^{-3}$ (purple). (b) Plots for the ratio $\xi(n)$ for the same anharmonicities. Both are shown as functions of the number of collision model steps n and assuming $q = 0.25$, $c = 1$ and $\frac{g}{\omega_p} = 0.018$.

Since the stored energy decreases if the coupling increases, as seen in Fig. 4.7, it is interesting to analyze also whether the ergotropy itself decreases with the increasing of the coupling. To this end Fig. 4.14 shows $\xi(n)$ varying g/ω_p for two different values of the anharmonicity $\alpha_r = 8.8 \times 10^{-3}$ (green) and $\alpha_r = 11.8 \times 10^{-3}$ (purple).
This shows that, even though the stored energy varies appreciably with the coupling (see Fig. 4.7), the fraction of extractable energy $\xi(n)$ remains almost unaffected, and this is true for both the α_r values examined. Similar results can be observed for all coupling values up to $\frac{g}{\omega_p} = 0.03$ but with a smaller amount of stored energy.
Furthermore, $\xi(n)$ exhibits its maximum value, where $\xi \approx 1$, in correspondence with the position of the peaks shown in Fig. 4.7 which, as already discussed, could be interesting when studying the transient charging regime.

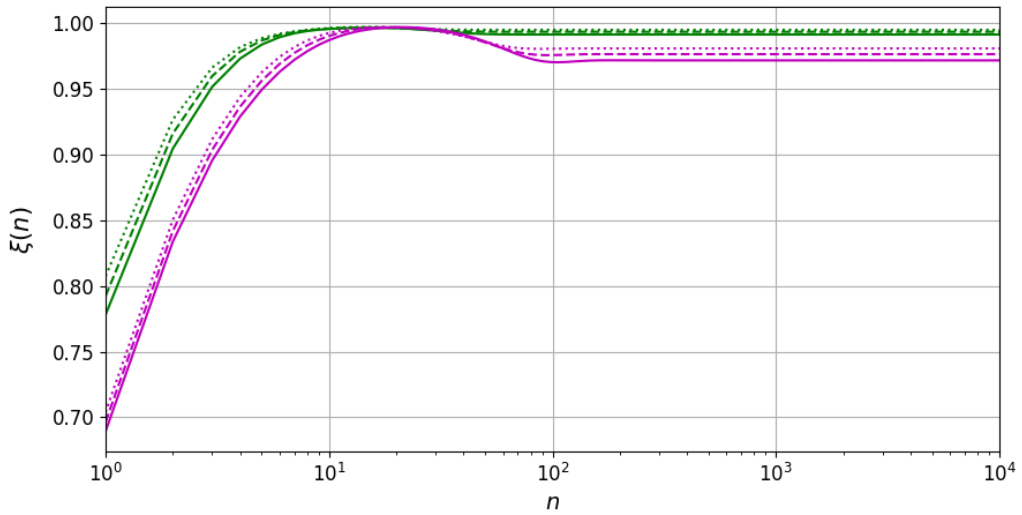

Figure 4.14: Plots of $\xi(n)$ shown as a function of the number of collision model steps n. Comparison between $\frac{g}{\omega_p} = 0.018$ (solid), 0.020 (dashed) 0.022 (dotted) for $\alpha_r = 8.8 \times 10^{-3}$ (green) and $\alpha_r = 11.8 \times 10^{-3}$ (purple) assuming $q = 0.25$, $c = 1$

We can conclude, as expected, that the decreasing of the stored energy causes the ergotropy to lower in turn, with their ratio remaining almost unchanged. This figure also confirms the relationship between purity and ergotropy already discussed: $\xi(n)$ is indeed slight smaller for $\alpha_r = 11.8 \times 10^{-3}$ (purple) than for $\alpha_r = 8.8 \times 10^{-3}$ (green), consistently with what happens for the purity. Ergotropy variations, however, are not as evident as the corresponding purity variations.

4.3.3 Quantum advantage

We compare here the coherent and incoherent charging protocol, obtained by initializing each ancilla in the state in Eq. (4.1.2) respectively with $c = 1$ and $c = 0$. Here, the stored energy is only discussed in units of E_{max}. Fig. 4.15 shows the comparison in terms of stored energy (Fig. 4.15(a)) and purity (Fig. 4.15(b)) for $g/\omega_p = 0.01$ and the corresponding anharmonicities already discussed in Figs. 4.2, 4.4 and 4.12.
Two striking features emerge from these plots: the amount of stored energy in the incoherent protocol is almost irrelevant compared with that of the coherent protocol, and this is valid for each of the anharmonicities considered; moreover the purity in the incoherent case stabilizes far below that of the coherent one, reaching $P \approx 0.5$ independently from α_r. Fig. 4.16 shows similar results for $g/\omega_p = 0.018$.

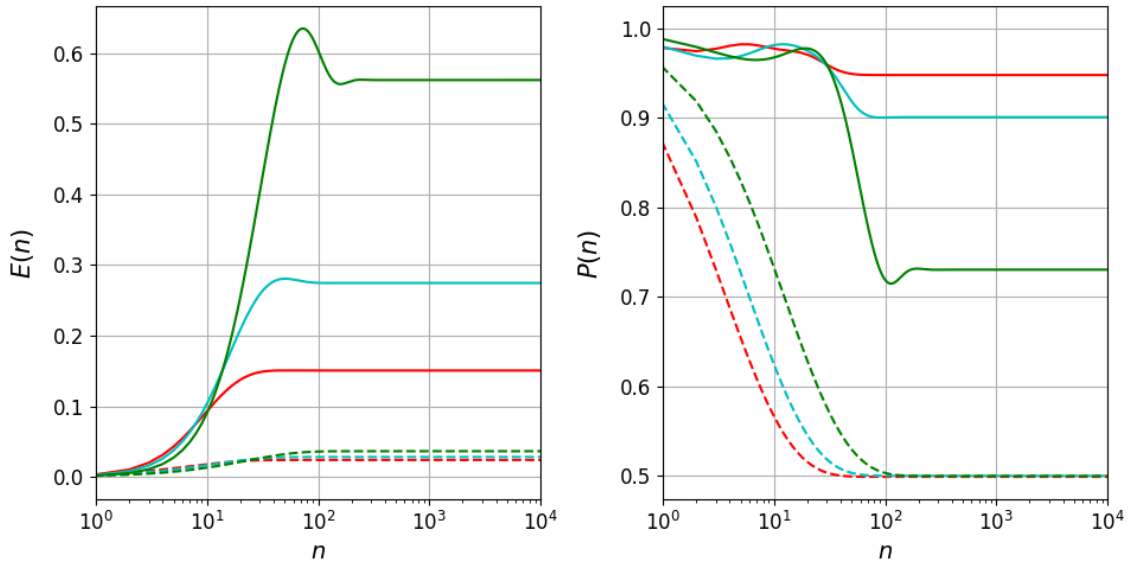

(a) (b)

Figure 4.15: (a) Stored energy $E(n)$ in units of E_{max}: comparison between the coherent charging protocol ($c = 1$, solid) and the incoherent one ($c = 0$, dashed) for $\alpha_r = 5.9 \times 10^{-3}$ (red), $\alpha_r = 6.9 \times 10^{-3}$ (cyan), $\alpha_r = 8.8 \times 10^{-3}$ (green). (b) Analogous plots for the purity $P(n)$. Both are shown as functions of the number of collision model steps n and assuming $q = 0.25$ and $\frac{g}{\omega_p} = 0.01$.

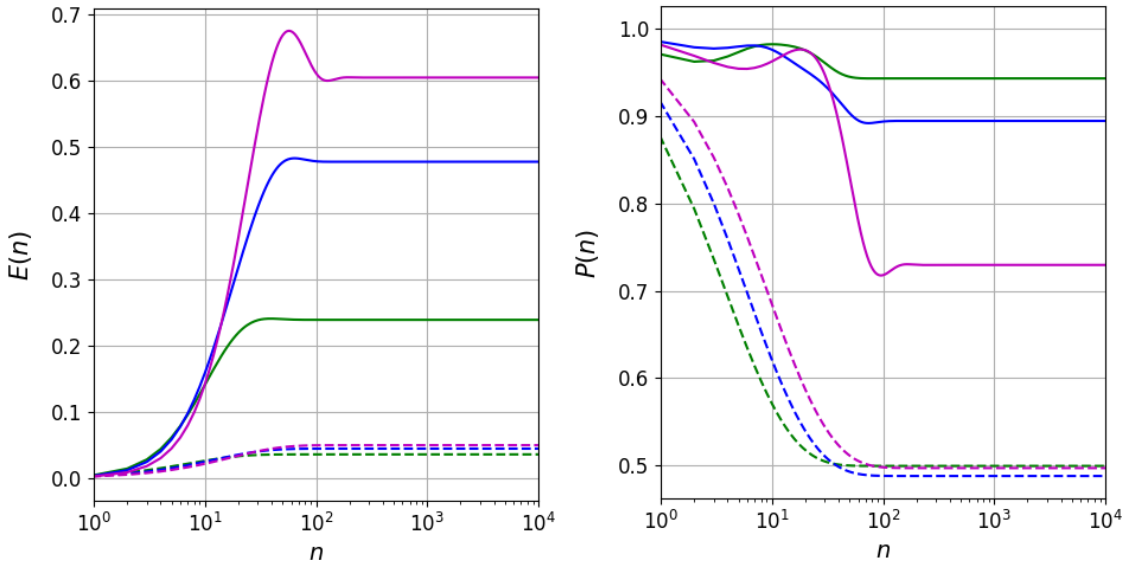

(a) (b)

Figure 4.16: (a) Stored energy $E(n)$ in units of E_{max}: comparison between the coherent charging protocol ($c = 1$, solid) and the incoherent one ($c = 0$, dashed) for $\alpha_r = 8.8 \times 10^{-3}$ (green), $\alpha_r = 10.2 \times 10^{-3}$ (blue), $\alpha_r = 11.8 \times 10^{-3}$ (purple). (b) Analogous plots for the purity $P(n)$. Both are shown as functions of the number of collision model steps n and assuming $q = 0.25$ and $\frac{g}{\omega_p} = 0.018$.

This marks a very significant difference with respect to the Micromaser case, where a significant amount of energy could be stored in the battery also in the incoherent case which, however, revealed to be instable with respect to coupling deviations.
These results not only point out the supremacy, in terms of stored energy, of the coherent charging protocol but also suggest that the very small amount of stored energy of the incoherent protocol cannot be entirely extracted, given the purity behaviour shown in Figs. 4.15(b) and 4.16(b). To confirm this, in Fig. 4.17 we show $\xi(n)$ defined in Eq. (4.3.4) for the incoherent protocol.

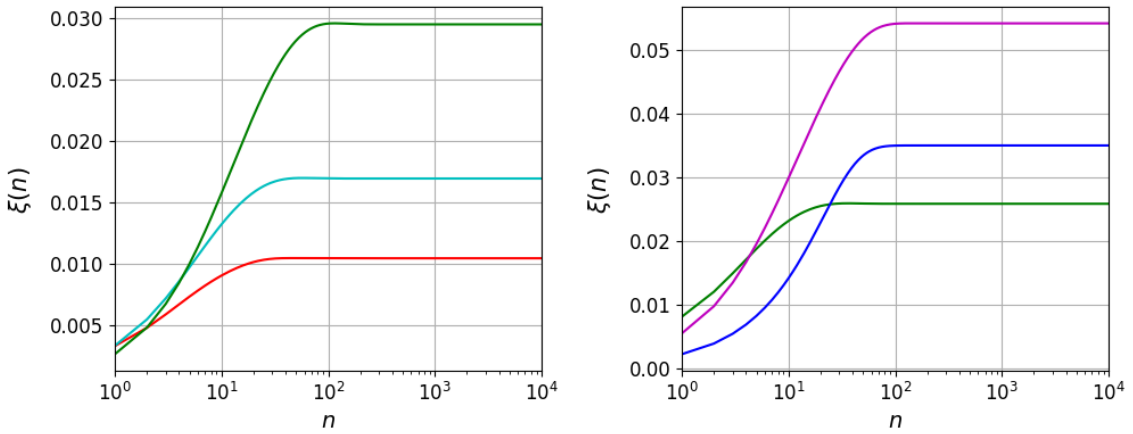

(a) (b)

Figure 4.17: $\xi(n)$ as a function of the number of collision model steps n assuming $c = 0$, $q = 0.25$ for: (a) $g/\omega_p = 0.01$, comparing $\alpha_r = 5.9 \times 10^{-3}$ (red), 6.9×10^{-3} (cyan), 8.8×10^{-3} (green). (b) $g/\omega_p = 0.018$, comparing $\alpha_r = 8.8 \times 10^{-3}$ (green), 10.2×10^{-3} (blue), 11.8×10^{-3} (purple).

From these figures it is clear that only a small fraction $\xi(n) \lesssim 5\%$ of the stored energy can be extracted in the incoherent case. Since the amount of stored energy is also very small, as shown in Figs. 4.15 and 4.16, we can conclude that the incoherent protocol is outperformed by its coherent counter part. This can be made clearer by showing plots for

$$\chi(n) = \frac{\mathcal{E}^{(i)}(n)}{\mathcal{E}^{(c)}(n)} \tag{4.3.5}$$

where $\mathcal{E}^{(i)}(n)$ and $\mathcal{E}^{(c)}(n)$ respectively denote the incoherent and coherent ergotropy at a given step n.
This is shown in Fig. 4.18, confirming what anticipated: the coherent charging protocol outmatches the incoherent one in terms of energy which can be extracted from the battery. Indeed, for all considered cases, we have that after the stabilization $\chi(n) \lesssim 0.5\%$.

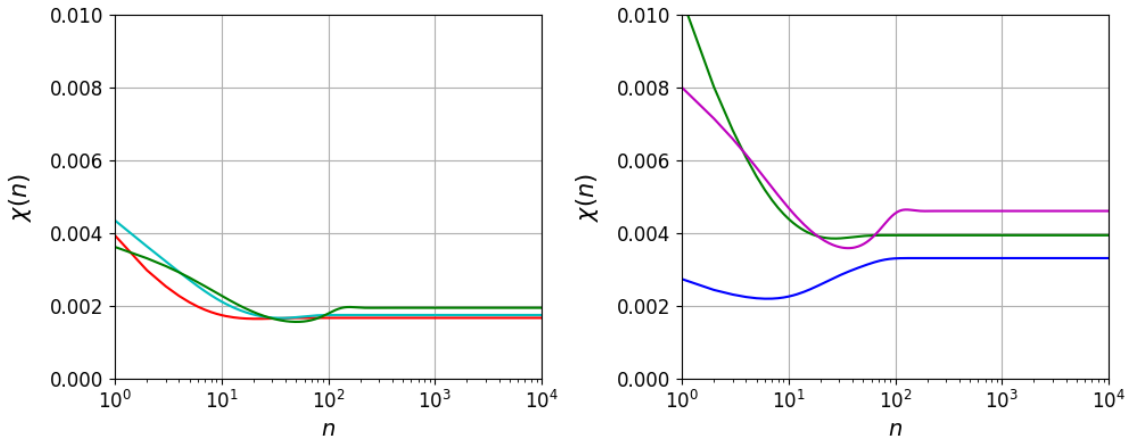

(a) (b)

Figure 4.18: Plots for $\chi(n)$ as a function of the number of collision model steps n assuming $q = 0.25$ for: (a) $g/\omega_p = 0.01$, comparing $\alpha_r = 5.9 \times 10^{-3}$ (red), 6.9×10^{-3} (cyan), 8.8×10^{-3} (green). (b) $g/\omega_p = 0.018$, comparing $\alpha_r = 8.8 \times 10^{-3}$ (green), 10.2×10^{-3} (blue), 11.8×10^{-3} (purple).

The discussed supremacy of the coherent protocol is preserved when the coupling changes. This is evident in Fig. 4.19, where χ is shown as a function of n for multiple couplings and two anharmonicities $\alpha_r = 11.8 \times 10^{-3}$ and $\alpha_r = 8.8 \times 10^{-3}$, From this figure it is clear that changing the coupling is not effective in order to improve the incoherent protocol performances. This confirms that the supremacy of the coherent protocol in terms of stored energy (Figs. 4.15 and 4.16) and the small ergotropy of the incoherent one (Fig. 4.17) are preserved for all coupling values considered.

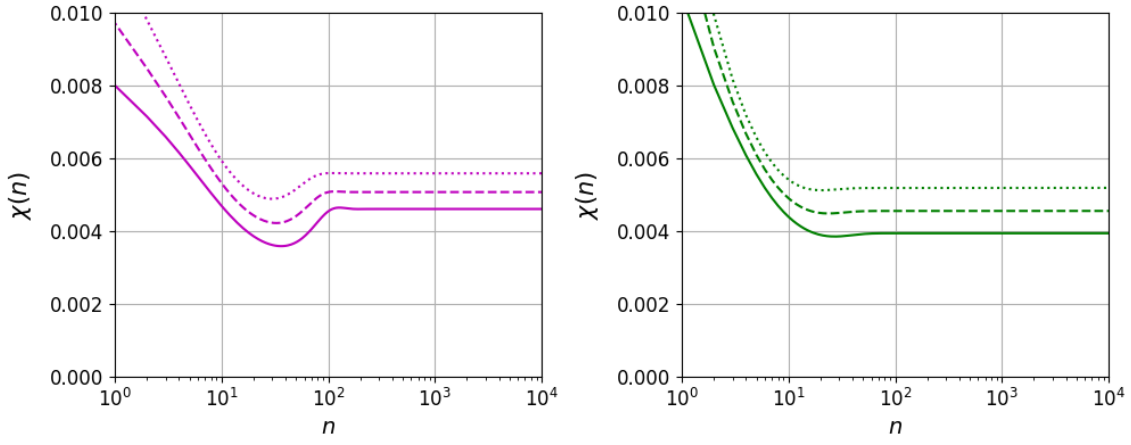

(a) (b)

Figure 4.19: Plots for $\chi(n)$ as a function of the number of collision model steps n, assuming $q = 0.25$. Comparison between $g/\omega_p = 0.018$ (solid), 0.020 (dashed), 0.022 (dotted) for: (a) $\alpha_r = 11.8 \times 10^{-3}$, (b) $\alpha_r = 8.8 \times 10^{-3}$.

4.3.4 Conclusions

The analysis carried out in this section suggests that a superconducting circuit in the transmon configuration is a promising platform to realize a collisional quantum battery characterized by excellent performances for both the storage and the extractability of energy. More in detail, we have observed, for the coherent charging protocol, that:

- a significant amount of energy can be stored in the system for anharmonicities such that $5.9 \times 10^{-3} \lesssim \alpha_r \lesssim 1.18 \times 10^{-2}$, provided that a suitable coupling regime is chosen for each anharmonicity;
- increasing the anharmonicity at fixed coupling causes the increasing of the fraction of stored energy compared to the maximum capacity of the battery E_{max} and also of the number of collisions needed for the stabilization, accompanied by the decreasing of the purity of the battery quantum state;
- the decreasing of E_{max} with respect to α_r, however, does not allow to state that the absolute value of the stored energy increases with the anharmonicity (see Fig. 4.5(b));
- despite the decrasing of the purity discussed above, the extractability of the stored energy remains very close to saturation, as pointed out by the high values of the ergotropy-energy ratio, always greater than 95%;
- the amount of stored energy and the purity may also depend on the specific value of the coupling, which is related to the size of the trap-like states appearing in the eveolved density matrix of the transmon. This affects the stored energy and purity stabilization value.

The above points, therefore, clarify that a significant amount of energy can be stored in the transmon also in the presence of anharmonicity, provided that a suitable coupling regime is chosen.

These relevant properties, however, are almost completely lost in the incoherent protocol. In this case a very small amount of energy can be stored in the system and, out of this, only a even smaller fraction can be extracted. This is confirmed by the small values of the ratio between the extractable energy of the incoherent and coherent case, which is always smaller than 0.5% after the stabilization.
These results seems to confirm that quantum coherences play a crucial role in enhancing and stabilizing the collisional charging of a anharmonic multi-level battery, though in a different way if compared with their role in the Micromaser case. As shown in Chapter 3, in fact, their role was to stabilize the stored energy with respect to coupling changes, but a significant amount of energy could also be stored in the Micromaser anyway. Here, their contribution is far more crucial, since they are fundamental in order to guarantee a relevant energy storage and extraction.

Conclusions and perspectives

This thesis fits in the context of quantum batteries, namely of quantum mechanical systems aimed at storing energy leveraging on their quantum features to outperform their classical counterparts. In particular, this work focused on a class of quantum batteries, known as collisional quantum batteries.

As shown in Chapter 2, collisional models constitute a possible approach to the study of open quantum systems, namely of systems interacting with an environment modeled as a collection of simple quantum systems, which can exchange energy with the system [10, 34]. The aim of collisional quantum batteries is to prove that, by properly engineering a sequence of interactions between the battery and a collection of simple quantum systems acting as chargers, it is possible to store energy in the battery in a profitable way.
To this end, various models of collisional quantum batteries have been proposed, such as a cavity charged by repeated interactions with a stream of two-level systems [31, 32, 33], proving them to be excellent testbeds for the role played by quantum features such as entanglement and quantum coherences in the enhancement of energy transfers between quantum systems [15, 31].

The aim of this thesis is to analyze the effects of the anharmonicity in multi-level collisional quantum batteries, characterizing both the charging and energy extraction processes and comparing the coherent and incoherent charging protocols, all going beyond existing literature.

To this end, we started studying the harmonic case focusing on one of the most significant model proposed, the aforementioned Micromaser [32, 33]. We reproduced the results of these works on the advantages of employing coherent chargers, consisting of two level systems charging up a cavity, compared with the incoherent case. The collisional dynamics of a cavity with a collection of incoherent two-level systems allows to store a significant amount of energy only for a set of fine-tuned values of the cavity-ancilla coupling. This energy, however, reveals to be instable with respect to slight deviations of the coupling from such values, so that the incoherent charging protocol of a Micromaser is not suitable for the realization of a stable battery. This problem reveals to be solvable by introducing quantum coherences in the chargers, which prove to act as stabilizers with respect to slight deviations from fine-tuned values. In reproducing such results, we also considered intermediate regimes of quantum coherences which were not explored in literature, showing the gradual stabilization (with respect to coupling deviations from fine tuned values) of the energy, obtained by gradually increasing quantum coherences.

After doing so, we moved to anharmonic systems playing the role of the battery, focusing on a superconducting circuit in the transmon regime, which allowed us to explore significantly anharmonic systems (see Sec. 4.1.1). To characterize this battery we studied its stored energy and its purity, together with the ergotropy, which is the maximal amount of energy extractable from the system through unitary operations. The numerical approach we performed allows us to show that a significant amount of energy can be stored in the system in the weak coupling regime in the coherent charging protocol case. Furthermore, almost the totality of this energy reveals to be extractable, with the ratio between the ergotropy and the stored energy never going below 95% after the stored energy stabilization.
Such noteworthy properties of charging and extraction processes, however, are destroyed by removing quantum coherences. Results for the incoherent charging protocol show, in fact, that a small amount of energy can be stored in the system and that an even smaller quantity of stored energy can be extracted from it.
This certifies the supremacy of the coherent charging protocol, in an even more evident way than in the Micromaser case: in the transmon case, quantum coherences are no more acting only as stabilizers, but constitute the fundamental ingredient for both the storage and extraction of energy.

Possible future developments inspired by this work could be focused on a more detailed study of the transient regime before the stabilization of the stored energy. This could be done, for example, by analyzing the possibility of hitting the peak values of the stored energy shown in Sec. 4.3.1 or, alternately, studying figures of merit which have been not characterized in this work such as the charging power.

However, if, as done in this work, one focuses on the asymptotic value of the stored energy for a large number of collisions, many aspects could be investigated further, both on the enhancement of the collisional charging and on the study of dissipative environmental effects, which we have not considered in this work. For what concerns the first point, it could be realized, for example, through a more detailed study of the energy balance of the global system. This may include the optimization of the energy transfers from the ancillae to the battery through the optimization of the model parameters and a wider scanning of the parameter space. A preliminary analysis in this direction, in fact, showed that a significant amount of energy remains in the ancillae after their interaction with the battery, so that it could be worth trying to extract it. Also, another noteworthy figure of merit is the energetic cost of switching-on and off the system ancilla interaction as much times as required for the stabilization of the battery.
For what concerns dissipative environmental effects, one could add a dissipative term to the quantum map ruling the single collision, as done in [32] for the study of a lossy Micromaser quantum battery or, otherwise, set up a second collision model, different from the charging one, for the dissipative interaction between the system and the environment.

Appendix: collision models simulations

We provide here a rough scheme of the most relevant parts of the code structure for the simulations of a collision model, which have been realized using tools provided by QuTiP (quantum Toolbox in Python) for matrix calculations and Master Equations solving [35]. We begin by the initialization of the simulation: the parameters and the Hamiltonian of both the battery (transmon, in this case) and the ancillae must be specified.

```
import numpy as np
from qutip import *
import time
import math

# INPUT AND RELEVANT PARAMETERS CALCULATIONS:
i = complex(0,1)
INPUTS = np.loadtxt('transmon.txt',usecols = 1)
E_J = INPUTS[0]            #Josephson energy
E_C = INPUTS[1]            #Capacitive energy
tr_size = int(INPUTS[2])   #transmon numerical size
delta_t = INPUTS[3]        #Single interaction duration
q = INPUTS[4]              #Ancillae ground state occupation
c = INPUTS[5]             #Ancillae degree of coherence
collisions = int(INPUTS[6]) #Total number of collisions
tr_initial_state = int(INPUTS[7]) #Initial state: e.g. gnd: 0
up_lim_jumps = int(INPUTS[8]) #Upper limit for the counter
   rotating frequencies
Lambda = E_C/E_J               #Anharmonicity
w_p = np.sqrt(8*E_C*E_J)       #Zeroth order frequency
g = 2*w_p/100                  #Coupling strength

# TRANSMON HAMILTONIAN AND EXACT DIAGONALIZATION:
#Charge term of the transmon hamiltonian
N_square = np.diag(4*E_C*(np.arange(-tr_size, tr_size + 1)**
   2))
N = Qobj(np.diag(np.arange(-tr_size, tr_size + 1)))
#Phase term in the N basis
M = 0.5*E_J*(np.diag(-np.ones(2*tr_size), 1) + np.diag(-np.
   ones(2*tr_size), -1))
```

```
H_tr = Qobj(N_square+M)
#Diagonalization of the transmon Hamiltonian
tr_eigenvalues, tr_eigenstates = H_tr.eigenstates()

# ANCILLA FREE HAMILTONIAN:
up = basis(2,0)
down = basis(2,1)
D = tr_eigenvalues[tr_initial_state+1]-tr_eigenvalues[
   tr_initial_state] #Energy gap of the ancilla
H_qb = 0.5*D*sigmaz()
#\sigma_- operator for the ancilla
sm = down*up.dag()

# FREE HAMILTONIANS:
# in order to perform calculations, all matrices involved
   must have the suitable sizes
H_0_tr = tensor(H_tr,qeye(2))
H_0_qb = tensor(qeye(tr_size),H_qb)
```

This can be extended to the Micromaser case by substituting the code for the transmon Hamiltonian with the oscillator Hamiltonian in terms of the annihilation operator as follows

```
a = destroy(osc_size)
H_ho = w_osc*a.dag()*a
```

and by inserting the oscillator and ancilla frequencies *w_osc* and D and the size *osc_size* among the input parameters.
Then, a single collision of the model can be carried out by employing the *mesolve* method to solve the quantum map as defined in Sec. 2.2.
The only inputs needed by the quantum map function are the battery and ancilla density matrices at the beginning of the collision. This can be implemented as follows.

```
def quantum_map(dm_init,dm_ancilla):
   dm0 = tensor(dm_init, dm_ancilla)  # global initial state
   duration_single_int = delta_t      # duration of the
   collision
   steps_single_int = 100             # output sampling times
   t_single_int = np.linspace(0,duration_single_int,
   steps_single_int)
   H_args = g
   results = mesolve(V,dm0,t_single_int,[],[],H_args)
   dm_tot_ev = results.states[len(t_single_int)-1] #final
   state
   dm_tot_herm = (dm_tot_ev+dm_tot_ev.dag())*0.5
 return dm_tot_herm
```

Focusing on the *mesolve* method, four inputs are required in the case of the evolution of a closed system (in this case, the system composed by the battery and the ancilla). From left to right: the interaction potential between the two systems V; an initial density

matrix $dm0$ given by the tensor product of the battery and ancilla initial conditions; an array with times for the evaluation of the output; the arguments H_args needed for the implementation of V (which depends from the system considered). The output consists in an array of density matrices evaluated at each value of the time in the input time array. Now, this structure needs to be iterated for the total number of collisions needed. To this end one can define the following function which, for each collision, carries out the single interaction through *quantum_map*.

```
def CM(dm_initial, dm_ancilla, collisions, g):
    times = np.zeros(collisions)
    energies = np.zeros(collisions)
    purities = np.zeros(collisions)
    ergotropies = np.zeros(collisions)
    energies[0] = E_initial
    times[0] = 0
    purities[0] = p_initial
    ergotropies[0] = E_initial
    for k in range(1, collisions, 1):

        #collision and evaluation of energy and purity
        dm_tot_herm = quantum_map(dm_initial,dm_ancilla)
        dm_ev = dm_tot_herm.ptrace(0)
    #system evolved reduced density matrix
        dm_herm = (dm_ev+dm_ev.dag())*0.5
    #hermitianization of the reduced density matrix
        Hrho = (H_tr*dm_herm+(H_tr*dm_herm).dag())*0.5
        energy = Hrho.tr()
    #energy of the system
        purity = (dm_herm*dm_herm).tr()
    #purity of the system

        #evaluation of the ergotropy (Sec. 1.4.2)
        dm_herm_eigenvalues, dm_herm_eigenstates = dm_herm.
    eigenstates()
        sorted_indices = np.argsort(dm_herm_eigenvalues)[::-1]
        dm_eigenvalues_sorted = dm_herm_eigenvalues[
    sorted_indices]
        dm_eigenstates_sorted = dm_herm_eigenstates[
    sorted_indices]
        en_fin_min = 0
        for i in range(0,len(tr_eigenvalues),1):
            en_fin_min = en_fin_min + dm_eigenvalues_sorted[i
    ]*tr_eigenvalues[i]
        ergotropy = energy - en_fin_min

        times[k] = k
        energy[k] = energy
        purity[k] = purity
```

```
94          ergotropies[k] = ergotropy
95          #updating the system density matrix for the next step
96          dm_initial = dm_herm
97          #This is the suitable point to extract some feedback
        results while the simulation progresses
98
99      return times,energies,purities,ergotropies,dm_herm
```

Bibliography

[1] A. Acín et al. "The quantum technologies roadmap: a European community view". In: *New Journal of Physics* **20**, 080201 (2018).

[2] D. P. DiVincenzo. "Quantum Computation". In: *Science* **270**,255-261 (1995).

[3] D. P. DiVincenzo. "The Physical Implementation of Quantum Computation". In: *Fortschritte der Physik* **48**, 771–783 (2000).

[4] I. M. Georgescu, S. Ashhab, and F. Nori. "Quantum simulation". In: *Review of Modern Physics* **86**,153–185 (2014).

[5] B. Fröhlich et al. "A quantum access network". In: *Nature* **501**,69–72 (2013).

[6] J. Buchmann et al. "Quantum cryptography: a view from classical cryptography". In: *Quantum Science and Technology* **2**, 020502 (2017).

[7] C. L. Degen, F. Reinhard, and P. Cappellaro. "Quantum sensing". In: *Review of Modern Physics* **89**,035002 (2017).

[8] C. A. Vincent and B. Scrosati. *Modern batteries*. Butterworth-Heinemann, 1997.

[9] R. Alicki and M. Fannes. "Entanglement boost for extractable work from ensembles of quantum batteries". In: *Physical Review E* **87**, 042123 (2013).

[10] G. Strini and G. Benenti. *Principles of quantum computation and information*. World scientific publishing, 2008.

[11] F. Binder et al. "Quantum thermodynamics of general quantum processes". In: *Physical Review E* **91**, 032119 (2015).

[12] F. Campaioli et al. "Enhancing the Charging Power of Quantum Batteries". In: *Physical Review Letters* **118**, 150601 (2017).

[13] F. Campaioli et al. *Colloquium: Quantum Batteries*. 2023. arXiv: `2308.02277 [quant-ph]`.

[14] G. M. Andolina et al. "Charger-mediated energy transfer in exactly solvable models for quantum batteries". In: *Physical Review B* **98**, 205423 (2018).

[15] G. M. Andolina et al. "Charger-mediated energy transfer for quantum batteries: an open system approach". In: *Physical Review B* **99**, 035421 (2019).

[16] F.-Q. Dou, Y.-J. Wang, and J.-A. Sun. "Highly efficient charging and discharging of three-level quantum batteries through shortcuts to adiabaticity". In: *Frontiers of Physics* **17**, 31503 (2021).

[17] G. Gemme et al. "Qutrit quantum battery: Comparing different charging protocols". In: *Physical Review Research* **6**, 023091 (2024).

[18] F. C Binder et al. "Quantacell: powerful charging of quantum batteries". In: *New Journal of Physics* **17**, 075015 (2015).

[19] F.A. Campaioli F. Pollock and S. Vinjanampathy. *Thermodynamics in the Quantum Regime*. Springer, 2018.

[20] I. Buluta, S. Ashhab, and F. Nori. "Natural and artificial atoms for quantum computation". In: *Reports on Progress in Physics* **74**, 104401 (2011).

[21] D. Loss and D. P. DiVincenzo. "Quantum computation with quantum dots". In: *Physical Review A* **57**, 120–126 (1998).

[22] J. Koch et al. "Charge-insensitive qubit design derived from the Cooper pair box". In: *Physical Review A* **76**, 042319 (2007).

[23] A Crescente et al. "Charging and energy fluctuations of a driven quantum battery". In: *New Journal of Physics* **22**,063057 (2020).

[24] G. Gemme et al. "IBM Quantum Platforms: A Quantum Battery Perspective". In: *Batteries* **8**,5 (2022).

[25] D. Ferraro et al. "High-Power Collective Charging of a Solid-State Quantum Battery". In: *Physical Review Letters* **120**, 117702 (2018).

[26] G. M. Andolina et al. "Quantum versus classical many-body batteries". In: *Physical Review B* **99**, 235446 (2019).

[27] J. Q. Quach et al. "Superabsorption in an organic microcavity: Toward a quantum battery". In: *Science Advances* **8** (2022).

[28] C.-K. Hu et al. "Optimal charging of a superconducting quantum battery". In: *Quantum Science and Technology* **7**, 045018 (2022).

[29] M. B. I. Wenniger et al. "Experimental Analysis of Energy Transfers between a Quantum Emitter and Light Fields". In: *Physical Review Letters* **131**, 260401 (2023).

[30] S. Seah et al. "Quantum Speed-Up in Collisional Battery Charging". In: *Physical Review Letters* **127**, 100601 (2021).

[31] R. Salvia et al. "Quantum advantage in charging cavity and spin batteries by repeated interactions". In: *Physical Review Research* **5**, 013155 (2023).

[32] V. Shaghaghi et al. "Lossy Micromaser Battery: Almost Pure States in the Jaynes–Cummings Regime". In: *Entropy* **25**, 430 (2023).

[33] V. Shaghaghi et al. "Micromasers as quantum batteries". In: *Quantum Science and Technology* **7**, 04LT01 (2022).

[34] F. Ciccarello et al. "Quantum collision models: open system dynamics from repeated interactions". In: *Physics Report* **954**, 1-70 (2022).

[35] J.R. Johansson, P.D. Nation, and F. Nori. "QuTiP: An open-source Python framework for the dynamics of open quantum systems". In: *Computer Physics Communications* **183**, 1760–1772 (2012).

[36] G. Wang, L. Zhang, and J. Zhang. "A review of electrode materials for electrochemical supercapacitors". In: *Chemical Society Reviews* **41**, 797–828 (2012).

[37] M. Polini et al. *Materials and devices for fundamental quantum science and quantum technologies*. 2022. arXiv: `2201.09260 [quant- ph]`.

[38] S. Bhattacharjee and A. Dutta. "Quantum thermal machines and batteries". In: *The European Physical Journal B* **94** (2021).

[39] S. Vinjanampathy and J. Anders. "Quantum thermodynamics". In: *Contemporary Physics* **57**, 545–579 (2016).

[40] N. Linden, S. Popescu, and P. Skrzypczyk. "How Small Can Thermal Machines Be? The Smallest Possible Refrigerator". In: *Physical Review Letters* **105**, 130401 (2010).

[41] A. Auffèves. "Quantum Technologies Need a Quantum Energy Initiative". In: *PRX Quantum* **3**, 020101 (2022).

[42] J. Stevens et al. "Energetics of a Single Qubit Gate". In: *Physical Review Letters* **129**, 110601 (2022).

[43] M. Le Bellac. *A Short Introduction to Quantum Information and Quantum Computation*. Cambridge University Press, 2006.

[44] P. Krantz et al. "A quantum engineer's guide to superconducting qubits". In: *Applied Physics Reviews* **6** (2019).

[45] M. H. Devoret, A. Wallraff, and J. M. Martinis. *Superconducting Qubits: A Short Review*. 2004. arXiv: `cond-mat/0411174 [cond-mat.mes-hall]`.

[46] W.P. Schleich. *Quantum Optics in Phase Space*. Wiley, 2011.

[47] G. Wendin and V. S. Shumeiko. *Experiments with single photons emitted by single atoms*. 2019. DOI: `10.13140/RG.2.2.33220.17288`.

[48] J. H. Davies. *The Physics of Low-dimensional Semiconductors: An Introduction*. Cambridge University Press, 1997.

[49] Y. V. Nazarov and Y. M. Blanter. *Quantum Transport: Introduction to Nanoscience*. Cambridge University Press, 2009.

[50] C. Livermore et al. "The Coulomb Blockade in Coupled Quantum Dots". In: *Science* **274**,1332-1335 (1996).

[51] A. Blais et al. "Circuit quantum electrodynamics". In: *Reviews of Modern Physics* **93**, 025005 (2021).

[52] N. K. Langford. *Circuit QED - Lecture Notes*. 2013. arXiv: `1310.1897 [quant-ph]`.

[53] A. F. Kockum and F. Nori. *Fundamentals and Frontiers of the Josephson Effect*. Springer International Publishing, 2019.

[54] F. Yoshihara et al. "Superconducting qubit–oscillator circuit beyond the ultrastrong-coupling regime". In: *Nature Physics* **13**,44–47 (2016).

[55] G. Grosso and G.P. Parravicini. *Solid State Physics*. Elsevier Science, 2000.

[56] G. Wendin and V. S. Shumeiko. *Superconducting Quantum Circuits, Qubits and Computing*. 2005. arXiv: `cond-mat/0508729 [cond-mat.supr-con]`.

[57] B. D. Josephson. "The discovery of tunnelling supercurrents". In: *Review of Modern Physics* **46**, 251-254 (1974).

[58] B.D. Josephson. "Possible new effects in superconductive tunnelling". In: *Physics Letters* **1**, 251-253 (1962).

[59] A. Barone and G. Paternò. *Physics and Applications of the Josephson Effect*. Wiley, 1997.

[60] S. Olivares. *Lecture notes on Quantum Computing*. 2015. URL: `http://solivarescq.ariel.ctu.unimi.it`.

[61] R. P. Feynman, R. B. Leighton, and M. Sands. *The Feynman lectures on physics: The Definitive Edition (Vol. 3)*. Pearson, 2009.

[62] M. Kjaergaard et al. "Superconducting Qubits: Current State of Play". In: *Annual Review of Condensed Matter Physics* **11**, 369–395 (2020).

[63] I. Pietikäinen et al. "Photon blockade and the quantum-to-classical transition in the driven-dissipative Josephson pendulum coupled to a resonator". In: *Physical Review A* **99**, 063828 (2019).

[64] C. Cohen-Tannoudji, B. Diu, and F. Laloe. *Quantum Mechanics, Volume 1: Basic Concepts, Tools, and Applications*. Wiley, 2019.

[65] J. J. Sakurai. *Modern quantum mechanics; rev. ed.* Addison-Wesley, 1994.

[66] A. E Allahverdyan, R Balian, and Th. M Nieuwenhuizen. "Maximal work extraction from finite quantum systems". In: *Europhysics Letters (EPL)* **67**, 565–571 (2004).

[67] H.-P. Breuer and F. Petruccione. *The Theory of Open Quantum Systems*. Oxford University, 2006.

[68] A. Crescente. "New perspectives in the theoretical study of quantum batteries". PhD thesis. 2023. DOI: `10.15167/crescente-alba_phd2023-03-09`.

[69] G. Lindblad. "On the Generators of Quantum Dynamical Semigroups". In: *Communications in Mathematical Physics* **48**, 119-130 (1976).

[70] V. Gorini, A. Kossakowski, and E. C. G. Sudarshan. "Completely Positive Dynamical Semigroups of N-Level Systems". In: *Journal of Mathematical Physics* **17**, 821-825 (1976).

[71] J.-F. Huang, J.-Q. Liao, and L.-M. Kuang. "Ultrastrong Jaynes-Cummings model". In: *Physical Review A* **101**, 043835 (2020).

[72] D. Meschede, H. Walther, and G. Müller. "One-Atom Maser". In: *Physical Review Letters* **54**, 551 (1985).

[73] J. J. Slosser and P. Meystre. "Tangent and cotangent state of electromagnetic field". In: *Physical Review A* **41**, 3867-3874 (1990).

[74] J. J. Slosser, P. Meystre, and S. L. Braunstein. "Harmonic oscillator driven by a quantum current". In: *Physical Review Letters* **63**, 934–937 (1989).

[75] M. Hofheinz et al. "Generation of Fock states in a superconducting quantum circuit". In: *Nature* **454**,310–314 (2008).